THE CRUSTAL STRUCTURE OF CARNEGIE RIDGE INFERRED FROM GRAVITY AND SEISMIC DATA

A Thesis

by

GIORGIO DE LA TORRE

Submitted to the Office of Graduate Studies of
Texas A&M University
in partial fulfillment of the requirements for the degree of

MASTER OF SCIENCE

May 2005

Major Subject: Oceanography

THE CRUSTAL STRUCTURE OF CARNEGIE RIDGE INFERRED FROM GRAVITY AND SEISMIC DATA

A Thesis

by

GIORGIO DE LA TORRE

Submitted to Texas A&M University
in partial fulfillment of the requirements
for the degree of

MASTER OF SCIENCE

Approved as to style and content by:

William W. Sager (Chair of Committee)	William R. Bryant (Member)
Thomas W. C. Hilde (Member)	Niall C. Slowey (Member)
	Wilford D. Gardner (Head of Department)

May 2005

Major Subject: Oceanography

ABSTRACT

The Crustal Structure of Carnegie Ridge Inferred from

Gravity and Seismic Data. (May 2005)

Giorgio De La Torre, B.S., Escuela Superior Naval "Cmdte. Rafael Morán Valverde"

Chair of Advisory Committee: Dr. William W. Sager

Carnegie Ridge is a prominent bathymetric feature of the Galápagos Volcanic Province originated from the interaction of the Galápagos Hot Spot and the Cocos - Nazca Spreading Center. Our present knowledge regarding its crustal structure is limited to ridge transects along which wide-angle refraction seismic experiments have been conducted. In this study, the long-wavelength crustal structure of Carnegie Ridge between ~81° W and 89° W was determined by employing 2-D forward gravity modeling as the primary analytical technique. Model structures were built by assuming Airy isostasy and crustal layers of constant density. The geometry and density structure of the thickened oceanic crust beneath the ridge was constrained based on available seismic velocity models. Except for regions near the Ecuador Trench, the gravity modeling solution along the different transects examined in this study accounted adequately for the observed gravity anomaly field over the ridge. Crustal overthickening mainly accommodated in oceanic layer 3 and the asymmetry of the crustal root geometry characterize the estimated long-wavelength crustal structure. The asymmetry on eastern Carnegie Ridge is thought to be related to a ridge-related rifting whereas the origin and nature of that estimated on western Carnegie Ridge remain uncertain. Crustal volume

fluxes were calculated at Carnegie Ridge and the Galápagos Archipelago, and at Cocos Ridge in order to explain the along-axis variations of the estimated crustal thickness. Along-axis crustal thickness variations on eastern Carnegie Ridge, and the formation of its bathymetric saddle were found to be related to the decline in the total volume output of the Galápagos Hot Spot. According to my results, this decay started soon after the spreading center shifted to the south of the hotspot (i.e., ~15 Ma) and continued for ~4.5 m.y. Since ~10 Ma the volume output of the GHS started to increase again, giving rise to the formation of western Carnegie Ridge and the Galápagos Archipelago. This increase continued until ~2 Ma, when the hotspot intensity started a new decrease that continues until the present time.

DEDICATION

I dedicate this thesis to my family.

To my wife Erika for being such an extraordinary spouse and friend. Without your love and inspiration during all these years, I had not accomplished this goal.

To my parents Jorge and Susana for their unconditional love and permanent support. You have not only been extraordinary parents but also my best and most sincere friends.

To my brother Alex and my sister Estefanía for complementing my life.

I would also like to dedicate this thesis to the memory of my grandfather Miguel, who will be always in my heart.

This work is for all of you

ACKNOWLEDGMENTS

In first place, I would like to thank the Ecuadorian Navy for supporting my studies at Texas A&M University. My special recognition to Captain Fernando Zurita and Captain Patricio Goyes who trusted in my professional capacity.

For their time, patience, and permanent support, I would like to thank my committee chair Dr. William W. Sager, and committee members: Dr. Thomas Hilde, Dr. William Bryan, and Dr. Niall Slowey.

I would also like to thank Dr. Valentí Sallarés for providing an important part of the data set employed in this study, and particularly for his attention and fast response to my questions.

I finally would like to thank Mrs. Sandy Drews for helping me with the formatting and editing of my manuscript.

TABLE OF CONTENTS

Page

CHAPTER Page

LIST OF FIGURES

FIGURE Page

FIGURE Page

LIST OF TABLES

CHAPTER I

INTRODUCTION

The morphology of the Galápagos Volcanic Province (GVP) is dominated by the presence of thickened blocks of oceanic crust, with Carnegie, Cocos, Malpelo, and Coiba submarine ridges the major geological features of this large oceanic igneous province (Figure 1). According to tectonic evolution models proposed for the region [*Hey*, 1977; *Lonsdale and Klitgord*, 1978; *Barckhausen et al.*, 2001], these ridges represent the surface expression of the interaction between the Galápagos Hot Spot (GHS) and the Cocos-Nazca Spreading Center (CNSC) during the last ~23 m.y. The characteristic crustal structure observed across the volcanic ridges of the GVP, particularly their crustal thickening, represents one of the most widely known evidences of the complex hotspot – ridge interaction. Crustal thickening, which is considered to be mainly accommodated in oceanic layer 3 [e.g., *Mutter and Mutter*, 1993; *Walther, 2003*; *Sallarés et al.*, 2003], is thought to be the result of increasing melt production typically associated with the presence of a hot spot near a spreading center [*Morgan et al*, 1978].

The analysis of crustal thickness inferred across various ridge segments of the GVP and along the present-day CNSC has been used to determine important aspects of the tectonic evolution of this region such as: crustal volume flux through time, relative location of the GHS with respect to the CNSC at different periods of time, and temporal variations on the hot-spot – ridge distance [*Sallarés and Charvis*, 2003].

This thesis follows the style and format of *Journal of Geophysical Research.*

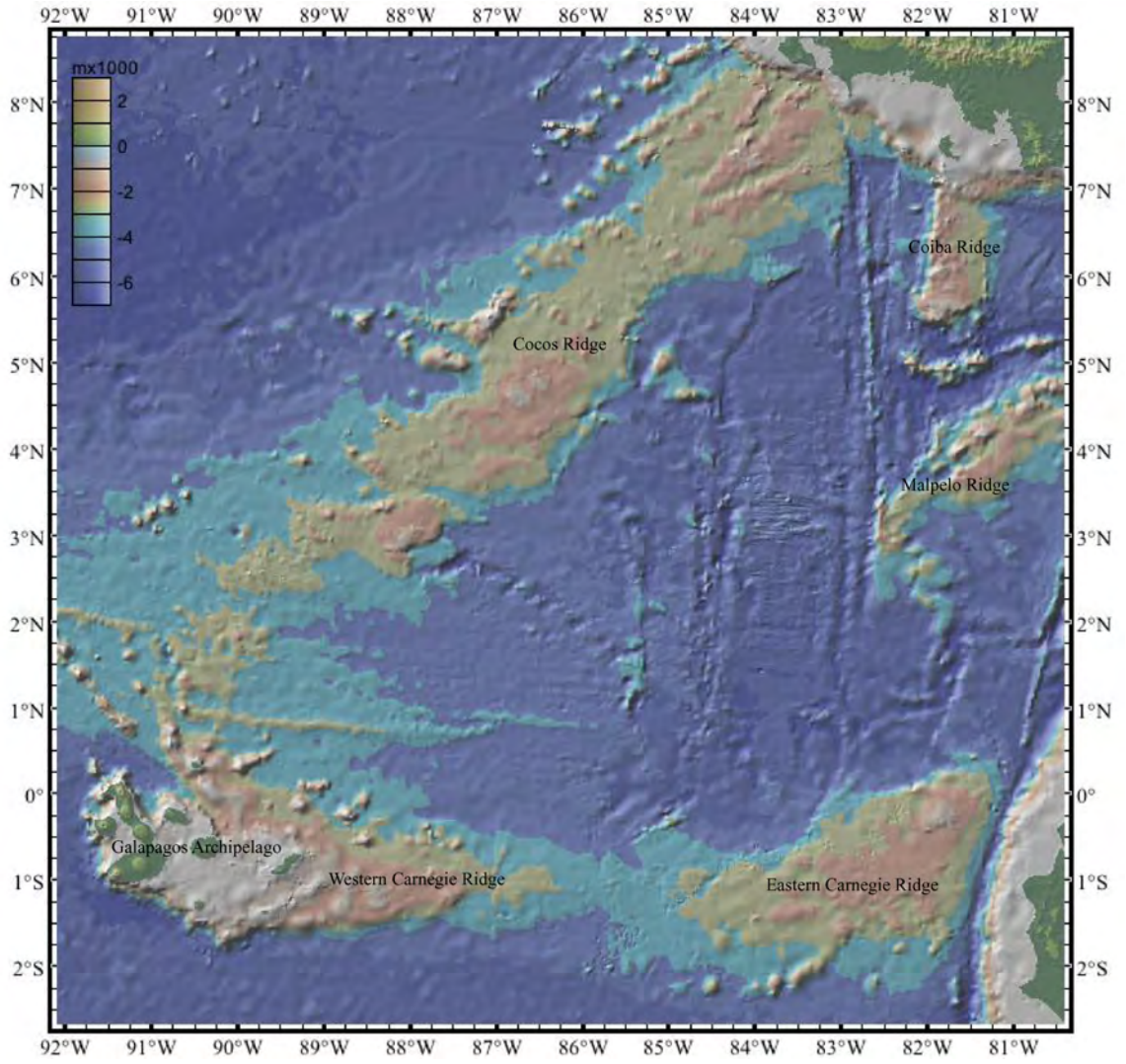

Figure 1. Bathymetry map of the Galápagos Volcanic Province. The map shows the location of Carnegie, Cocos, Malpelo, and Coiba ridges.

In a similar way, a joint analysis of crustal thickness and velocity models determined across various segments of Carnegie [*Sallarés et al.*, submitted, 2004], Cocos, and Malpelo [*Sallarés et al.*, 2003] ridges has been employed to estimate the characteristics

of the GHS - CNSC interaction, particularly mantle melting parameters that can account for the observed velocity structures. These parameters have been constrained based on mantle melting models [e.g., *Korenaga et al*., 2002], as well as other geophysical [*Schilling*, 1991; *Ito and Lin*, 1995; *Canales et al*., 1997, 2002] and geochemical [*Schilling et al*., 1982; *Detrick et al*., 2002] data collected in the region.

Our present knowledge regarding the crustal thickness and particularly the crustal-seismic structure across different ridge segments of the GVP has been inferred from wide-angle refraction seismic data, employing forward modeling [*Walther*, 2002, 2003] and seismic tomography inversion [*Sallarés et al*., 2003; *Graindorge et al*., 2004; *Sallarés et al*., submitted, 2004] techniques. 2-D forward gravity modeling has been employed as a complementary analytical tool in order to test the consistency of seismic structure models inferred from seismic data, and particularly to constrain Moho geometry in regions where it has not been clearly resolved by seismic data. The methodology previously described is constrained by the availability of seismic data and its results therefore limited to those transects where such data have been collected. Even though a series of wide-angle seismic experiments have been recently conducted along the present-day CNSC [*Canales et al*., 2002] and across selected ridge segments of the GVP [*Sallarés et al*., 2003; Walther, 2002, 2003], a major portion of this vast igneous province remains unexplored and many aspects of its crustal structure consequently unresolved. For this reason, it is desirable to consider alternative and more flexible analytical techniques that allow us to obtain consistent crustal structure estimations in regions where seismic refraction data are not available. In order to accomplish this

objective, during the present study I employed two-dimensional forward gravity modeling as the primary analytical technique to determine the long-wavelength crustal structure along selected ridge segments of the GVP. This study has been oriented to estimate the crustal structure of Carnegie Ridge between ~81° W and 89°W. I have limited gravity modeling to this area in order to avoid the complications of modeling gravity data in regions near the Ecuador trench system where I would have to integrate the upper plate structure and some large variation in slow velocity sediments (low densities) that may have strong short-wavelength effects (D. Graindorge, personal communication, 2004). In a similar way, I have excluded areas to the west in order to stay away from the GHS, particularly from the tectonic complications that it may cause (i.e., dynamic uplift).

As a first step in this study, a systematic approach to determine 2-D crustal models along any ridge segment is established by assuming that the ridge is isostatically compensated according to the Airy model. The geometry and density of the bodies that define the estimated model structures are constrained based on available seismic structure models. By applying this approach, crustal models are then built along various ridge transects with available shipboard free-air gravity anomaly data and a nearly perpendicular orientation relative to the along-axis direction of the ridge. The consistency and errors of the estimated model structures are evaluated based on the gravity modeling solution along these transects. Third, the results of this study are summarized by defining a crustal thickness grid and then an excess crustal thickness grid (the thickness of normal oceanic crust excluded) for Carnegie Ridge. Fourth, similar

gridded data sets are produced for Galápagos Archipelago and Cocos Ridge by assuming Airy isostasy and employing the same crustal densities used to define the model structures across Carnegie Ridge. Finally, I employ the estimated excess crustal thickness grid for Carnegie (including the Galápagos Archipelago) and Cocos ridges in order to determine the crustal volume flux at these ridges, compare their variations through time, and the implications of the observed variations on the tectonic evolution of the GVP.

1.1. Geological Setting

Carnegie Ridge is a prominent aseismic ridge, ~1350 km long and up to ~300 km wide, rising ~2000 m above the surrounding seafloor (Figure 2). The separation of this ridge into two elongated triangular-shaped parts is thought to represent the result of the complex tectonic evolution of the GVP, particularly the temporal variations on the relative location and interaction between the GHS and the CNSC. The hotspot - ridge interaction began soon after the onset of spreading between the Cocos and Nazca plates, which are thought to have originated as a result of the breaking of the ancient Farallon plate at ~25 Ma [*Hey*, 1977; *Lonsdale and Klitgord*, 1978].

The presence of a differential stress regime within this plate [e.g., *Wortel and Cloetingh*, 1981] has been proposed as a plausible mechanism to explain its fragmentation, along a pre-existing zone of weakness [*Hey*, 1977], that subsequently began rifting between the Cocos and Nazca plates. This rifting was reorganized into an approximately North-South spreading configuration (CNSC) at ~23 Ma [*Hey*, 1977].

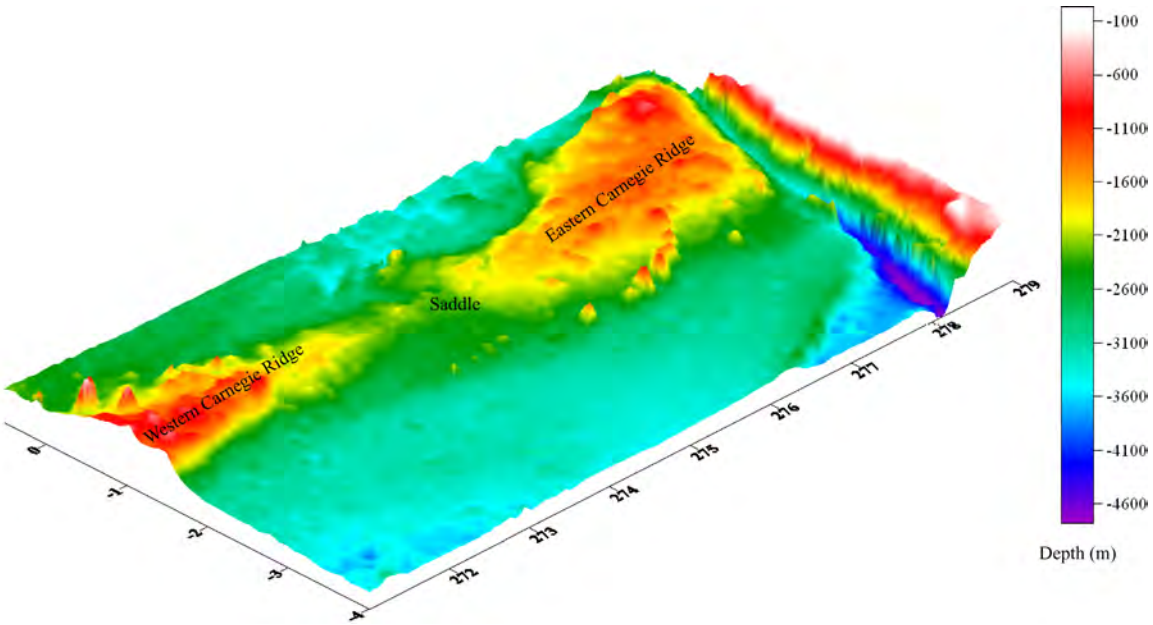

Figure 2. Surface map of Carnegie Ridge. The map shows the triangular-shaped eastern and western segments of the ridge as well as the central-saddle segment separating them.

Recent tectonic evolution models propose a three stage development of the CNSC based on the analysis of magnetic anomalies, dredge samples of the GVP [*Meschede and Barckhausen*, 2001; *Barckhausen et al.*, 2001], and the relative location between the GHS and the CNSC [*Sallarés and Charvis*, 2003]. According to these models (see Figure 3 for reference), after the breaking of the Farallon plate and the onset of spreading between the Cocos and Nazca plates, the CNSC was originally oriented ENE between ~23 and 19.5 Ma when the ridge jumped south changing its strike to a nearly

E-W orientation. During this time, the GHS was approximately ridge centered, based on a comparison of isochronous ridge segments on both sides of the present-day CNSC (Carnegie and Malpelo ridges), which show similar crustal thickness [*Sallarés and Charvis*, 2003]. Between ~19.5 and 14.5 Ma the tectonic evolution of the GVP was characterized by the northward migration of the CNSC relative to the GHS [*Meschede and Barckhausen*, 2001; *Sallarés and Charvis*, 2003], along with a series of small southward ridge jumps that kept the distance between the GHS and the CNSC ~50 km.

The motion of the Cocos (SW-NE) and Nazca (E-W) plates, as outlined by the trend of the Cocos and Nazca ridges, is thought to be the result of the migration of the CNSC combined with the N-S spreading along the CNSC and the E-W spreading along the East Pacific Rise [*Sallarés and Charvis*, 2003]. At ~14.5 Ma a major ridge jump placed the GHS beneath the Cocos plate [*Barckhausen et al*., 2001], reducing the amount of volcanic material emplaced on the Nazca plate and subsequently giving rise to the observed saddle that divides the two elongated triangular-shaped parts of Carnegie Ridge [*Meschede and Barckhausen*, 2001]. The volcanic material missing in this region is thought to be presently represented in its conjugate isochronous segment of Cocos Ridge [*Meschede and Barckhausen*, 2001]. At ~7.5 Ma the continuous northward migration of the CNSC placed the GHS beneath the Nazca plate (its present-day configuration) increasing the amount of material deposited in this plate and subsequently giving rise to the formation of the western segment of Carnegie Ridge and the Galápagos Archipelago.

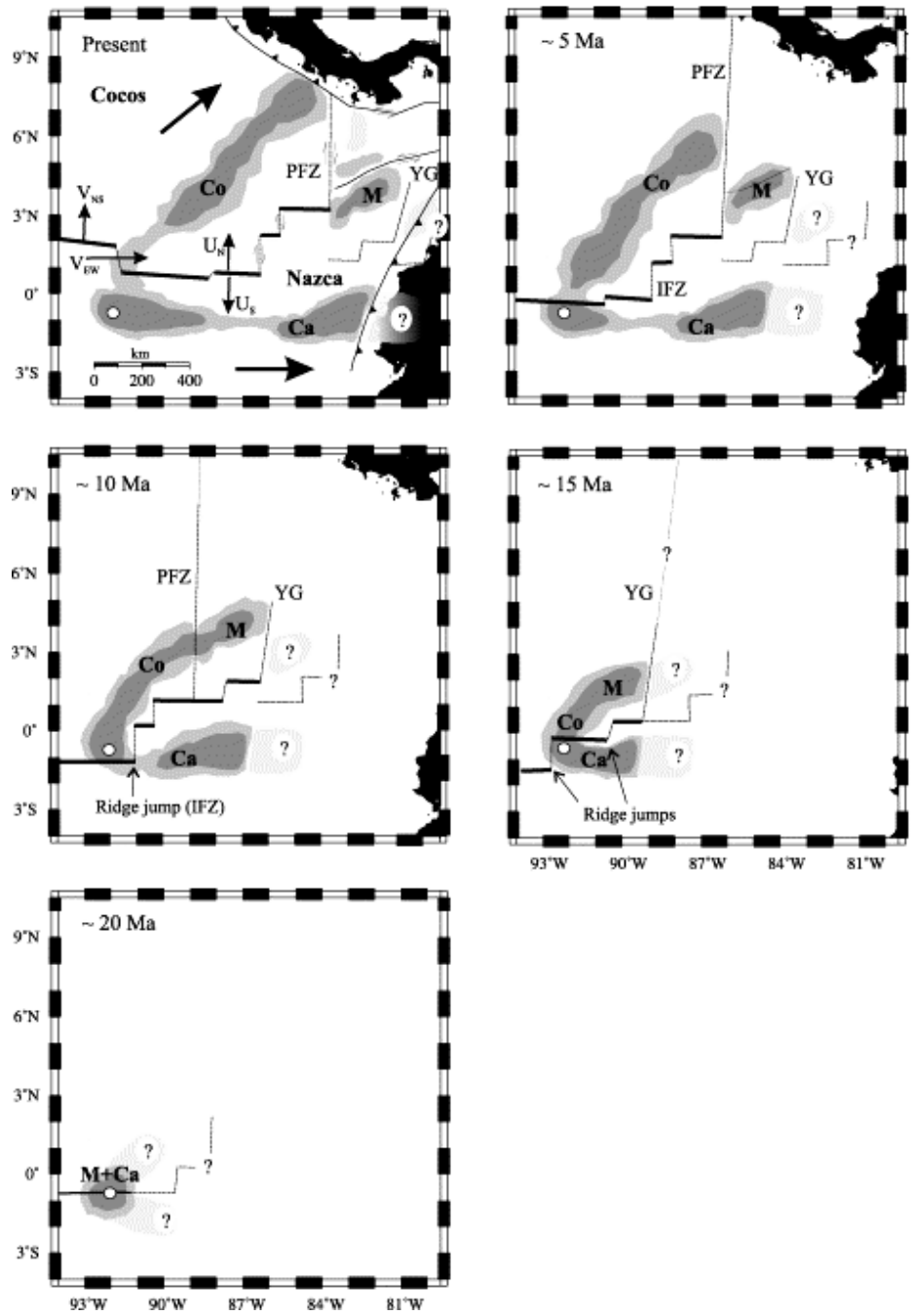

Figure 3. Tectonic evolution of the Galápagos Volcanic Province during the last 20 m.y. Reprinted from Earth and Planetary Science Letters, 214, Sallarés and Charvis, Crustal thickness constraints on the geodynamic evolution of the Galápagos Volcanic Province, 545-559, Copyright (2003), with permission from Elsevier.

1.2. Previous Work

The seismic structure of Carnegie ridge has been inferred from wide-angle refraction seismic data collected across two transects located in the eastern and central-saddle segments of the ridge [*Sallarés et al*., submitted, 2004] and another perpendicular to the trench axis, located south of the bathymetric ridge bulge [*Graindorge et al*., 2004] (Transects 1, 2, and 3, respectively, in Figure 4). The velocity structure across these transects (Figure 5 for transects 1 and 2) is characterized by values for oceanic layer 2 ranging from 3.0 km/s to 6.5 km/s along transects 1 and 2, and mean velocities of 4.8 km/s and 5.5 km/s at the top and base of this layer, respectively, along transect 3. Layer 3 is characterized by velocity values ranging from 6.8 km/s and 7.2 km/s along transects 1 and 2, and from 6.4 km/s and 7.3 km/s along transect 3. The 6.5 km/s isovelocity contour defined in the velocity models along transects 1 and 2 has been proposed as the interface that marks the transition from a prominent vertical velocity gradient in oceanic layer 2 to a gentler one in oceanic layer 3, and, in turn, the boundary between these two layers [*Sallarés et al*., submitted, 2004]. Because few seismic reflection phases from the layer 2/layer 3 boundary have been identified in the seismic records, the change in velocity gradient is thought to reflect a transition from an upper altered layer (layer 2) to a lower unaltered layer (layer 3) instead of the boundary between layers with different lithological characteristics [*Sallarés et al*., submitted, 2004].

Velocity structures similar to those determined along transects 1 and 2 have been observed along their conjugate-isochronous ridge segments located across Malpelo and

Cocos ridges, respectively. This similarity of the velocity structures is considered to be in support of the common nature and origin attributed to the ridges of the GVP.

Crustal thickening beneath the ridge is considered to be mainly accommodated in oceanic layer 3 based on the nearly uniform thickness of layer 2 (3.5 +/- 1.0 km) regardless of crustal thickness variations observed along transects 1 and 2. The maximum crustal thickness estimated across Carnegie Ridge is 13 km, 19 km, and 14 km along transects 1, 2, (Figure 5) and 3, respectively. The variable crustal thickness observed along the ridge as well as across its conjugate ridge segments located in Malpelo and Cocos ridges is thought to represent the temporal variation in the hotspot - ridge interaction characterized by the relative motion of the CNSC with respect to the GHS during the last ~20 m.y [*Sallarés and Charvis*, 2003].

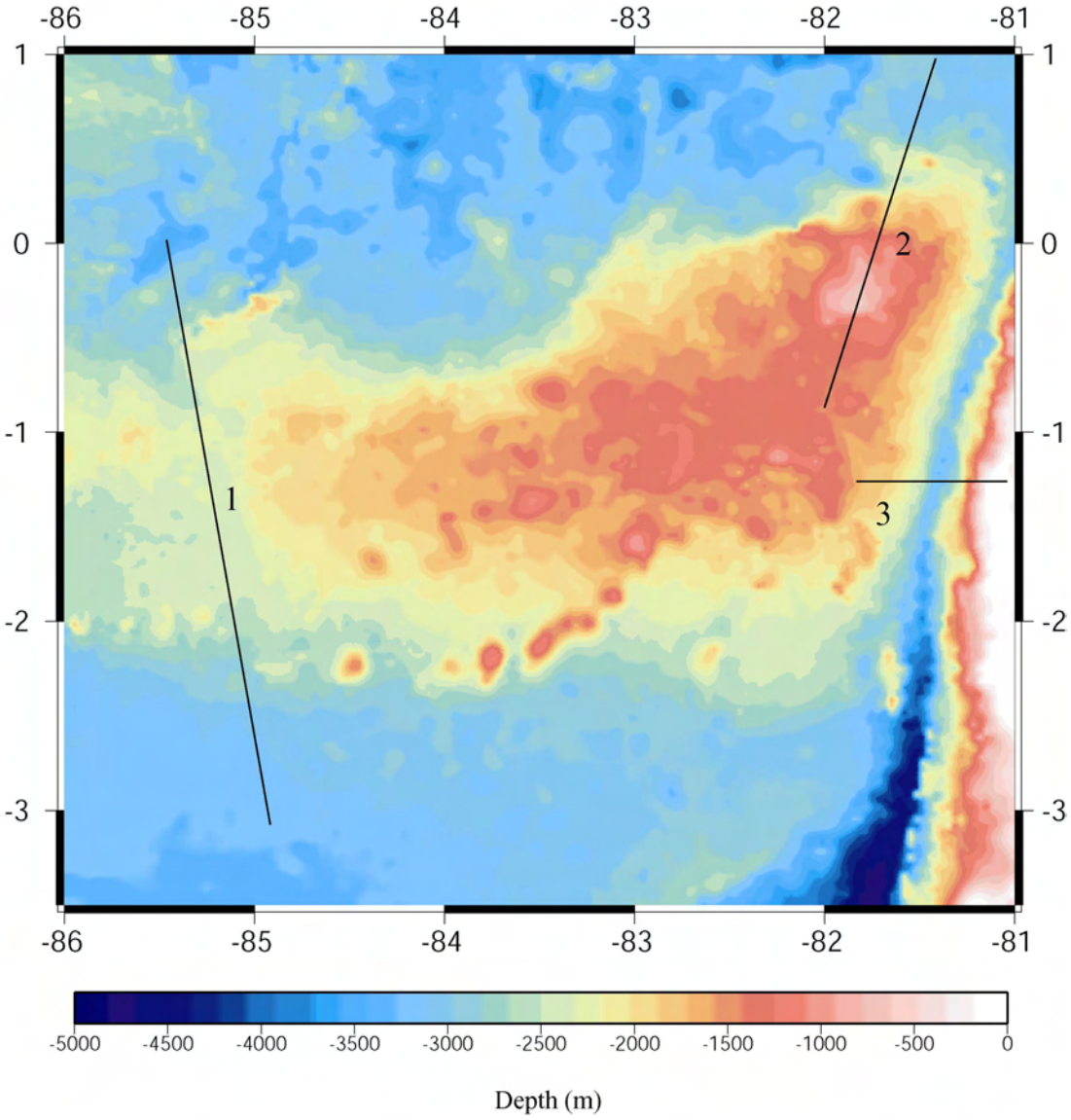

Figure 4. Transects along which the crustal structure of Carnegie Ridge has been determined from seismic refraction data.

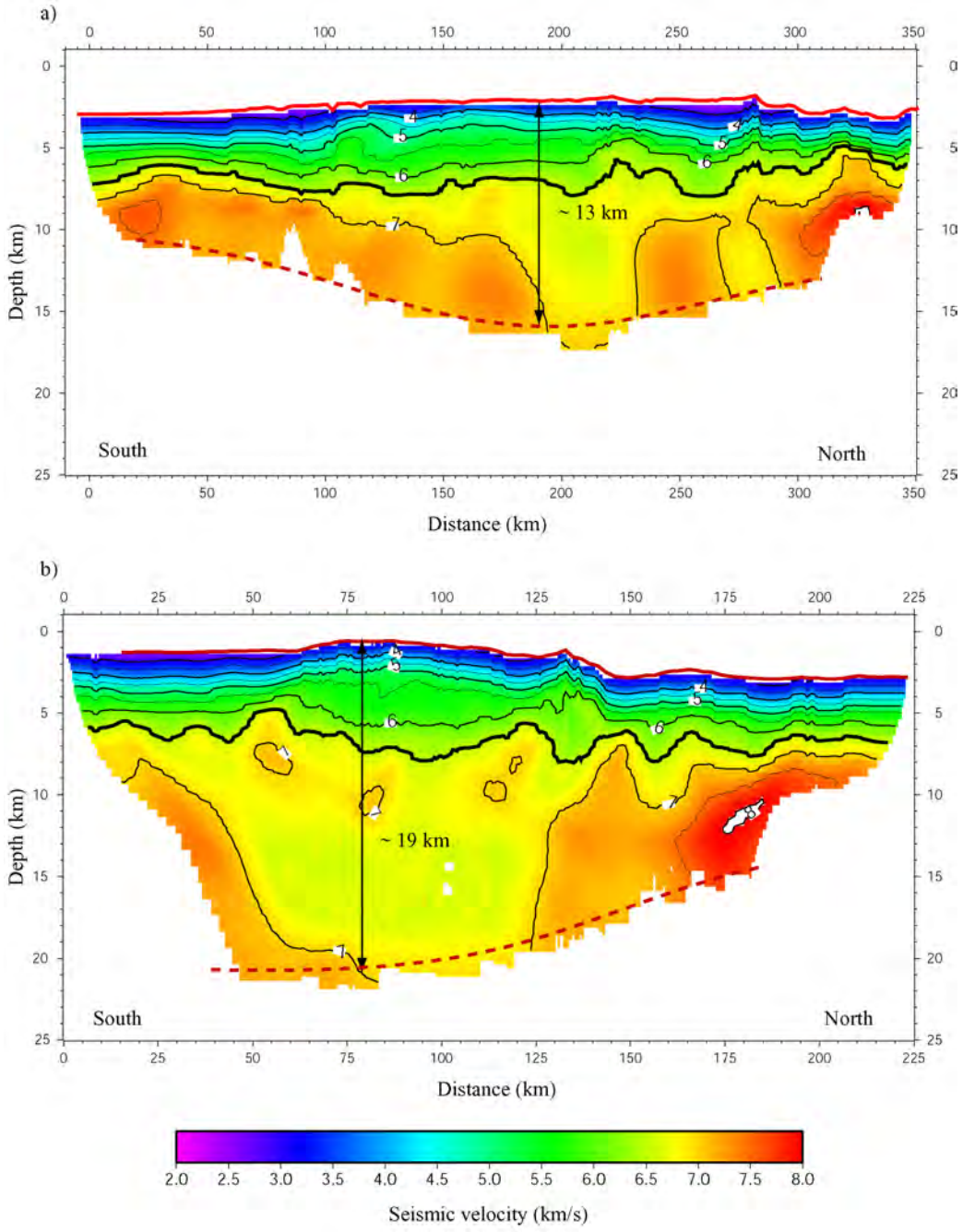

Figure 5. Averaged velocity models for Carnegie Ridge. a) central-saddle region (transect 1 in Figure 4); and b) western Carnegie ridge (transect 2 in Figure 4). The maximum crustal thickness (double arrow lines), as well as the estimated Moho geometry (dashed red line) are shown in each profile. Modified from *Sallarés et al*. [submitted , 2004].

CHAPTER II

METHODS

2.1. Data Sets

In this study, I employed the following geophysical data sets: ship-board corrected bathymetry and free-air gravity anomaly data, along with estimated sediment thickness data, all obtained from the National Geophysical Data Center (NGDC); and high-resolution predicted bathymetry and marine gravity data derived from satellite altimetry [*Sandwell and Smith*, 1997]. Data corresponding to the averaged velocity models for transects 1 and 2 (Figure 5) were provided by Dr. Valentí Sallarés from IRD-Géosciences Azur, France.

2.2. Crustal Structure Estimation

2.2.1. Modeling Method

2-D forward gravity modeling represents the primary analytical technique applied in this study with the purpose of predicting the crustal structure of Carnegie Ridge. The modeling of gravity data was carried out by employing a computer program that utilizes a line-integral method to calculate the free-air anomaly over 2-D crustal models composed of bodies of constant density [*Talwani et al*., 1959].

2.2.2. Crustal Model Definition

As the first step in this study, I established a systematic approach in order to define consistent 2-D crustal models along any arbitrary segment of Carnegie Ridge. As part of

this approach, my crustal models were built by assuming that the ridge is isostatically compensated as a result of variations in crustal root thickness (i.e., Airy model), according to the mass balance diagram described in Figure 6. The presence of an Airy type compensation on the study area is thought to be mainly supported by the formation of Carnegie Ridge near the spreading center [*Hey*, 1977; *Meschede and Barckhausen*, 2001; *Barckhausen et al*., 2001; *Sallarés and Charvis*, 2003], which resulted in volcanic material being emplaced on young and thin oceanic lithosphere [e.g., *Watts, 1978; Watts and Zhong*, 2000]. The presence of a weak lithosphere at the time of loading has been found to favor local isostatic compensation according to the Airy model on various young seamount chains in the Southeastern Pacific [*Calmant*, 1987] including the central and eastern segments of the Galápagos Archipelago (i.e., western Carnegie Ridge) [*Feighner and Richards*, 1994].

The bodies that compose my model structures are: a sedimentary layer; normal oceanic crust beneath the ridge; the bathymetric edifice relative to normal seafloor depth; and the isostatic crustal root. Regarding the sedimentary layer, its upper geometry along any ridge transects was defined by sampling data from a 2-min resolution predicted bathymetry grid derived from satellite altimetry [*Sandwell and Smith*, 1997]. This grid is available at ftp://topex.ucsd.edu/pub/global_topo_2min/. In a similar way, the thickness of this layer at any ridge area (h_l) and outside the ridge (h_s) was obtained from an estimated sediment thickness grid with a resolution of 5 min [*Divins*, 2001]. This grid is available at http://www.ngdc.noaa.gov/mgg/sedthick/sedthick.html. The information obtained from these two gridded data sets was employed, in turn, to define

basement geometry by adding the estimated sediment thickness values to those obtained from the predicted bathymetry grid. Because of the different resolution between the two gridded data sets, basement depth was determined only for those bathymetry points where sediment thickness is available.

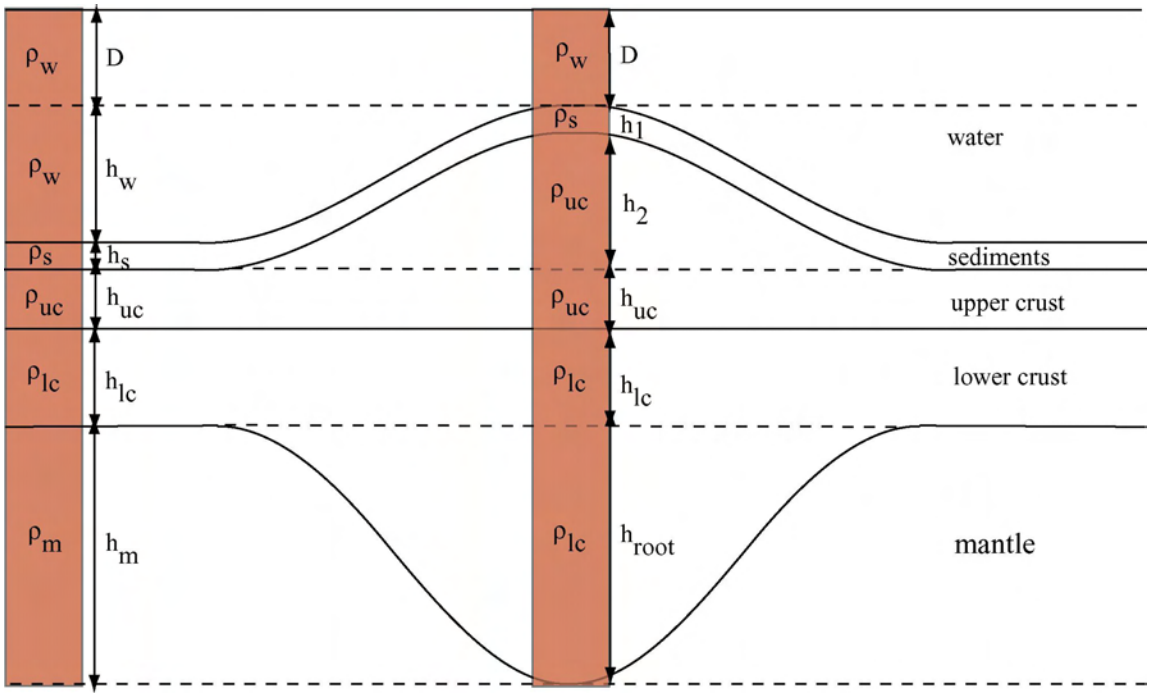

Figure 6. Mass balance diagram representing the isostatic compensation of an oceanic swell. Modified from J.P. Canales (personal communication, 2004).

The bathymetric anomalies (h_2) relative to normal seafloor depth, were calculated based on the same predicted bathymetry data set [*Sandwell and Smith*, 1997], after determining an appropriate base depth for the study area. The latter was established by calculating the peak of a histogram of depths within a polygon containing Carnegie Ridge and its adjacent oceanic basins. The density of the bathymetric edifice was assumed to be the same as the mean density of oceanic layer 2 (ρ_{uc}).

The variations in Moho depth (h_{root}) related to the estimated bathymetric anomalies (h_2) were calculated according to the following equation:

$$h_{root} = \frac{[(h_1\rho_s + h_2\rho_{uc}) - (h_w\rho_w + h_s\rho_s)]}{(\rho_m - \rho_{lc})} \qquad (1)$$

where ρ_m = mantle density, ρ_{lc} = lower crust density, ρ_{uc} = upper crust density, and ρ_s = sediment density. Heights denoted by h_1, h_2, h_s, and h_w, are shown in Figure 5. The geometry of the initially estimated isostatic crustal root was filtered in order to smooth the effects of short-wavelength local variations, particularly sharp changes in Moho depth related to small bathymetric anomalies. This filtering was carried out in a systematic way by employing a median filter with 40 km moving-window, which was found to preserve the long-wavelength features that characterize the crustal root geometry estimated in my crustal models. The density of the isostatic crustal root was assumed to be the same as the mean density of oceanic layer 3 (ρ_{lc}).

Regarding the configuration of normal oceanic crust beneath the ridge, it was assumed to be composed of oceanic layers 2 and 3 with a constant thickness in the outer ridge area as well as beneath the bathymetric edifice, and a flat interface at constant depth separating the two layers (Figure 6). I have assumed a flat interface because of the unpredictable character of the short wavelength variations that define the layer 2/layer 3 boundary determined from seismic refraction (the 6.5 km/s isovelocity contour in Figure 5). Because these variations appear unrelated to bathymetry and otherwise unpredictable without seismic data, the assumption of a flat layer 2/layer 3 interface was used as the best possible approximation.

2.2.3. Crustal Model Constraints

In order to constrain the potentially infinite number of possible crustal configurations that could account for the observed gravity field over the ridge, my crustal models were initially estimated along two ridge transects where crustal structure has been determined from seismic data [*Sallarés et al*., submitted, 2004] (transects 1 and 2 in Figure 4). Henceforth, I will refer to transects 1 and 2 as "reference transects".

The main elements that were constrained correspond to the geometry and density structure of the thickened crust beneath the ridge. The geometry was constrained by examining the maximum crustal thickness determined from seismic data along the reference transects, whereas the density structure defined by converting their seismic velocity models (Figure 5) into crustal density using an empirical velocity-density relation derived by *Carlson and Herrick* [1990] :

$$\rho = 3.81 - 6.0/V_p$$

The thickness of the sedimentary layer as well as the basement geometry defined in our models could not be accurately constrained because of the lack of seismic reflection data along the reference transects. In a similar way, the density of this layer could not be constrained given that the lack of seismic velocity values lower than 3.0 km/s (i.e., sediments) in the velocity models for reference transects 1 and 2 prevented the use of similar velocity-density relations for sediments [e.g., *Nafe and Drake*, 1957; *Hamilton*, 1978]. Because of this limitation, a density of ~1.70 g/cm^3 was assigned to this layer by integrating the results of Deep Sea Drilling Project sites 156 and 157 [*Heath and van Andel*, 1973], and Ocean Drilling Program sites 1238 and 1239 [*Shipboard Scientific Party*, 2003].

Table 1. Parameters employed to calculate crustal structure models along reference transects 1 and 2.

Parameter	Value
Water density (ρ_w)	1.03 g/cm^3
Sediment density (ρ_s)	1.71 g/cm^3
Upper crust density (ρ_{uc})	2.65 g/cm^3
Lower crust density (ρ_{lc})	2.95 g/cm^3
Mantle density (ρ_m)	3.3 g/cm^3
Reference crust (layer 2) thickness (h_{uc})	3 km
Reference crust (layer 3) thickness (h_{lc})	4 km

Based on these considerations, my crustal models were calculated along reference transects 1 and 2 following the approach described in section 2.2.2. and using the parameters in Table 1. Along transect 1 (Figure 7a), the estimated isostatic crustal root geometry fits well with the Moho geometry determined from seismic data, with a root mean squared (RMS) depth error of ~392 m. This misfit is considered acceptable since we are mainly interested in defining long-wavelength crustal features in our models. Moreover, the major source of this error comes from the northern part of transect 1 (between ~290 km and ~320 km) where Moho geometry has not been clearly resolved from seismic data. Along transect 2 (Figure 7b), a major difference between the estimated and the seismically determined Moho geometry is observed on the northern part of this transect (between ~120 and ~185 km). In this region, the isostatic crustal root geometry shows a steeper transition from the bulge of the ridge to the nearby oceanic basin than does the Moho geometry determined from seismic data. I consider that this misfit could be explained by Moho depth uncertainties in the seismic structure model. These uncertainties have been related to the nearly complete absence of seismic reflection phases from the crust/mantle boundary in the northern part of transect 2, between ~150 and 225 km, which have significantly reduced the resolution and accurate definition of this interface (V. Sallarés, personal communication, 2004). Furthermore, it has been suggested (V. Sallarés, personal communication, 2004) that the observed transition in crustal root geometry from beneath the ridge to the adjacent oceanic basin could be steeper than the geometry originally determined from seismic data, which would resemble the estimated crustal root configuration.

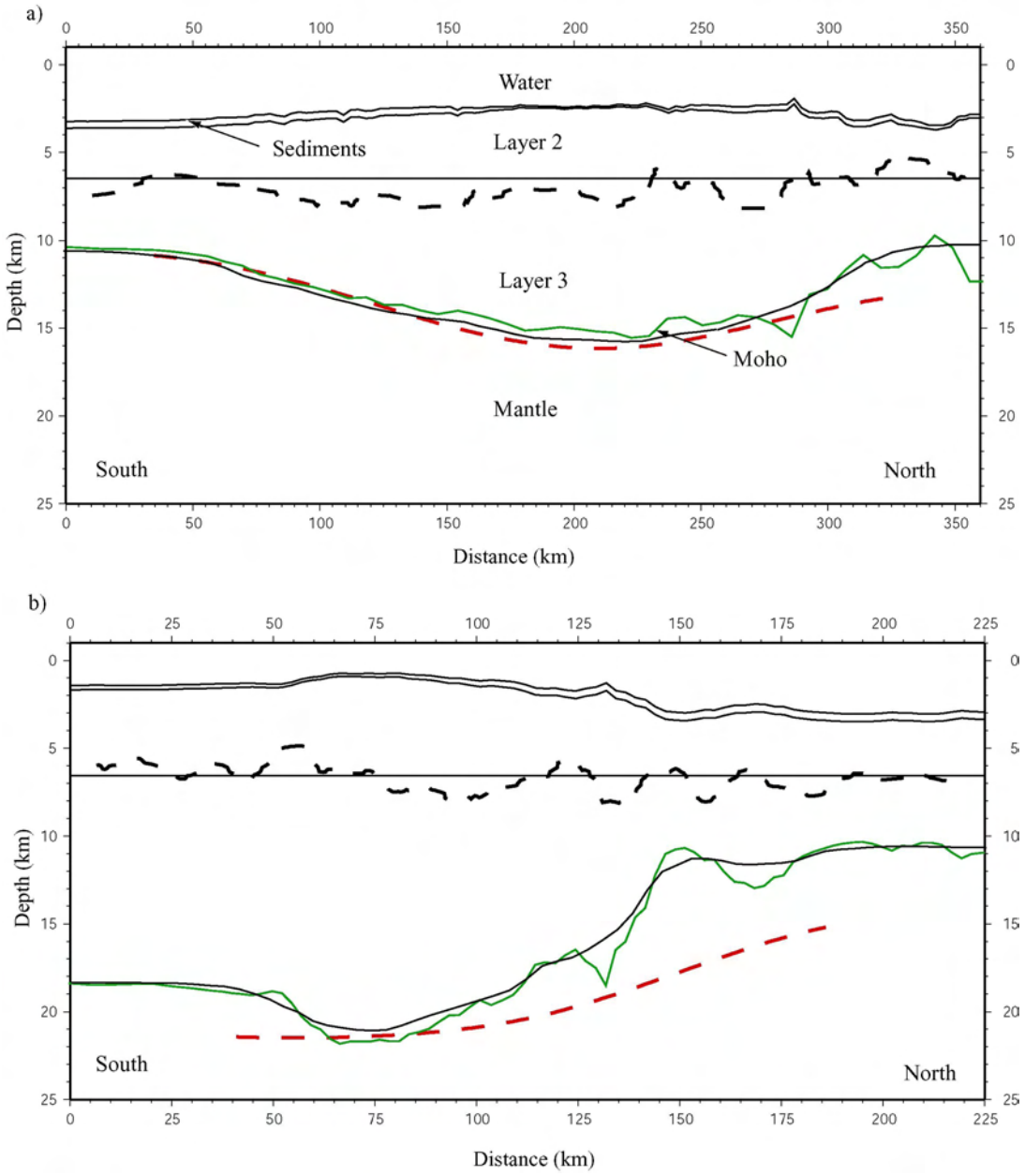

Figure 7. Crustal models along the reference transects. The upper panel (a) corresponds to reference transect 1 whereas the lower panel (b) corresponds to reference transect 2. Green solid lines represent the initially estimated isostatic crustal root geometry (before filtering). Dashed red lines represent the Moho geometry inferred from seismic data. Dashed black lines correspond to the 6.5 km/s isovelocity contour (Figure 5), which defines the layer 2/layer 3 interface in the seismic structure models.

The major difference between the estimated model structures and the seismic structure models along reference transects 1 and 2 corresponds to the interface between oceanic layers 2 and 3. In my crustal models, this interface was assumed to be flat and at a constant depth of 6.5 km in order to avoid the complications of modeling the irregular geometry that characterize the layer 2/layer 3 boundary determined along the reference transects (6.5 km/s isovelocity contour in Figure 5). Moreover, the unpredictable character of the short-wavelength variations that define the layer 2/layer 3 interface determined from seismic data prevents any attempt to model this irregular geometry directly from bathymetry data. The depth of this interface in my crustal models was determined by adding the thickness of oceanic layer 2 (3 km) to the estimated base depth (~3150 m) and to the mean sediment cover (~350 m) on the outer ridge area.

I consider that the irregular layer 2/layer 3 boundary determined from seismic data could be simplified into an approximate linear interface (similar to that defined in my crustal models) if the effects of short-wavelength local variations were smoothed in the velocity models along the reference transects. A similar approach was previously applied by *Sallarés et al*. [2003] along the conjugate segments of transects 1 and 2 located in southern Cocos and Malpelo ridges, respectively; showing that the irregular boundary between layers 2 and 3 is reshaped into a gentler interface at nearly constant depth (~6 +/- 1.0 km) (Figure 8). Furthermore, it has been suggested (V. Sallarés, personal communication, 2004) that the assumed flat interface at the depth defined in the model structure along the reference seismic sections constitutes a suitable representation of the boundary between these two layers.

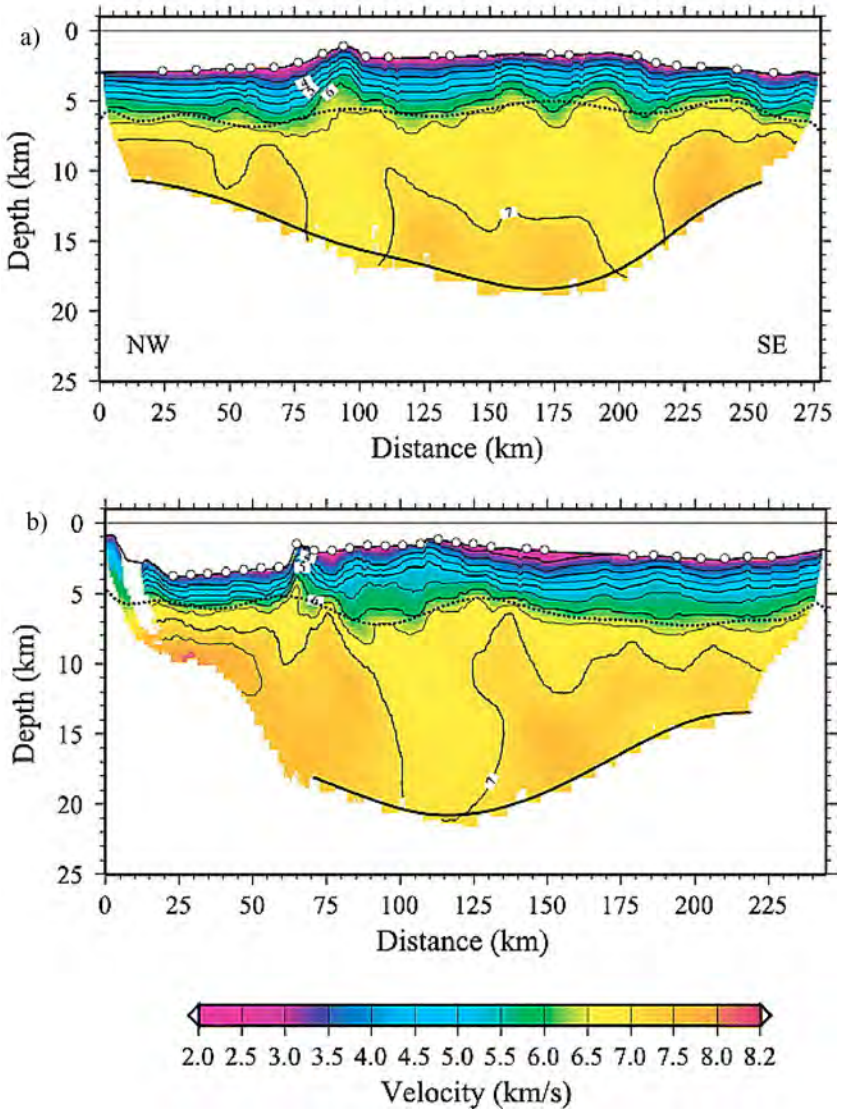

Figure 8. Averaged velocity models for southern Cocos Ridge (a) and Malpelo Ridge (b). The dashed line shows the layer 2/layer 3 interface corrected for the effects of short-wavelength local variations. Notice the gentler geometry of the corrected interface relative to irregular geometry originally defined from seismic data (6.5 isovelocity contour). Reprinted by permission of the American Geophysical Union from Sallarés V., Charvis P., Flueh L., and Bialas J., Seismic structure of the Cocos and Malpelo volcanic ridges and implications for hotspot-ridge interaction, Journal of Geophysical Research, 108, 2564, doi:10.1029/2003JB002431, 2003. Copyright [2003].

2.2.4. Model Structure Testing

Based on the results of my crustal models along reference transects 1 and 2, a similar approach was followed in order to define 2-D crustal models along several ridge transects located within a region where the geometry and density structure of the thickened oceanic crust has been constrained (i.e., between the reference transects) (Figure 9). I selected these transects (transects A-A' through D-D') considering the availability of shipboard free-air gravity data along them as well as their nearly perpendicular orientation relative to the along-axis direction of Carnegie Ridge.

The consistency and errors of the model structures determined along reference transects 1 and 2 (Figure 7), and along transects A-A' through D-D' (Figures 10 and 11) were evaluated by comparing the observed gravity anomaly field along them with the gravity anomaly calculated over the estimated crustal models. Because of the lack of shipboard free-air gravity data along the reference transects, the observed gravity anomaly data were obtained from a 2-min resolution gravity anomaly grid derived from satellite altimetry [*Sandwell and Smith*, 1997]. This grid is available at ftp://topex.ucsd.edu/pub/global_grav_2min/.

2.3. Crustal Volume Flux

The analysis of the gravity modeling solutions along the different ridge transects examined in this study (Chapter III) demonstrated that simple model structures built by assuming Airy isostasy account adequately for the observed gravity anomaly field over the ridge and subsequently for its long-wavelength crustal structure**.** Based on this

consideration, the results of this study were generalized by defining an isostatic crustal thickness grid for Carnegie Ridge, employing the same crustal densities used to define my model structures (Table 1).

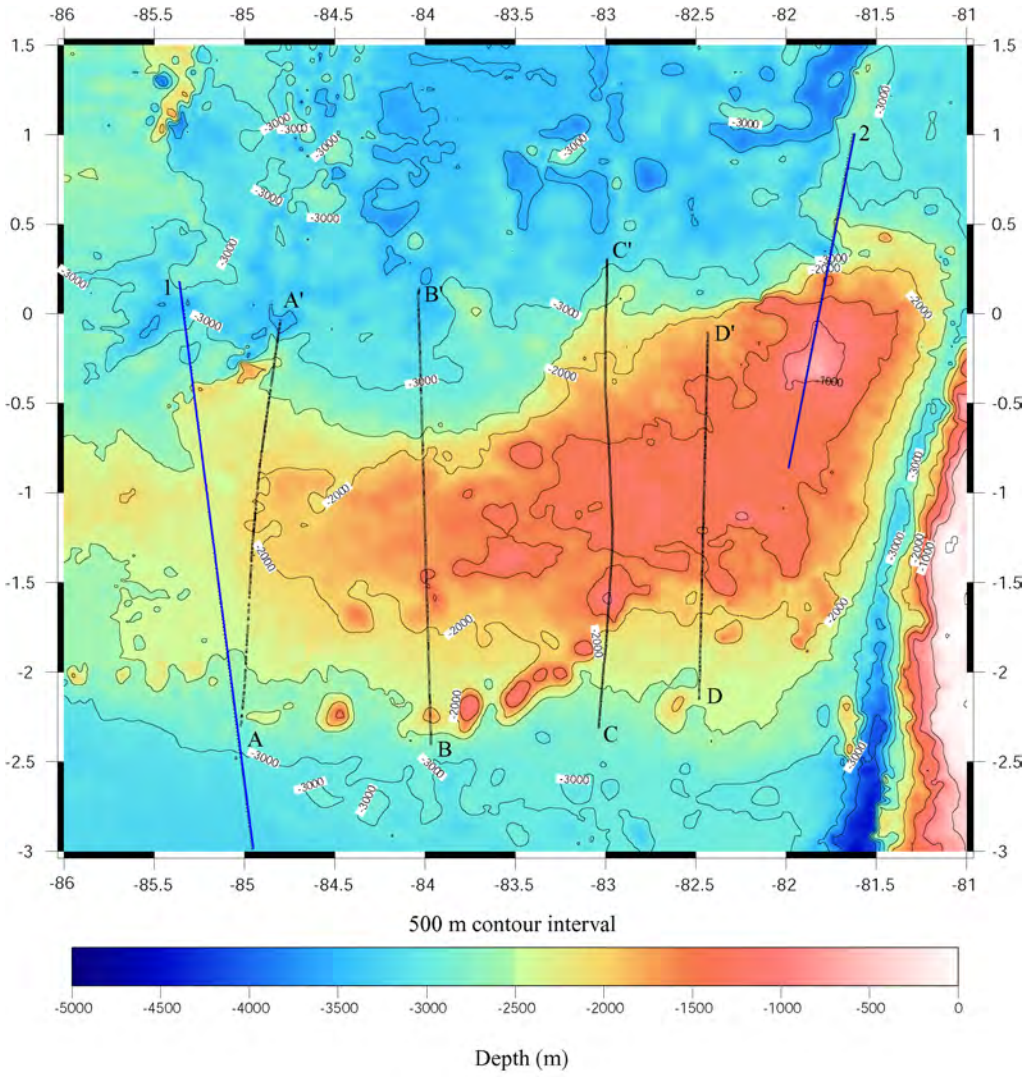

Figure 9. Bathymetric map of Carnegie Ridge showing the tracklines along which crustal structure models have been determined. Dashed lines show the locations of transects A-A' through D-D' Solid blue lines show the location of the reference transects 1 and 2.

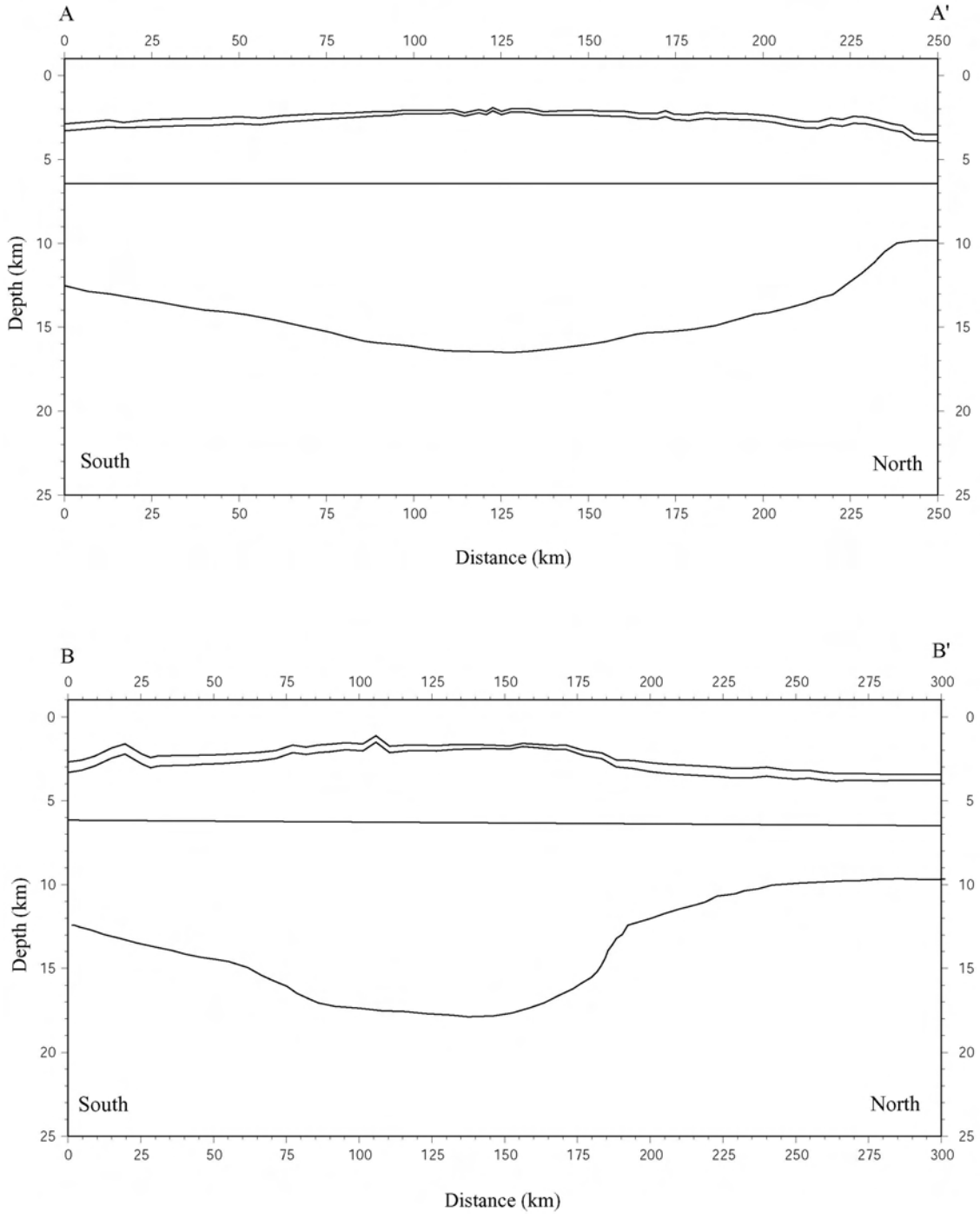

Figure 10. Crustal models along transect A-A' (upper crustal model) and B-B' (lower crustal model). The location of these transects is shown in Figure 9.

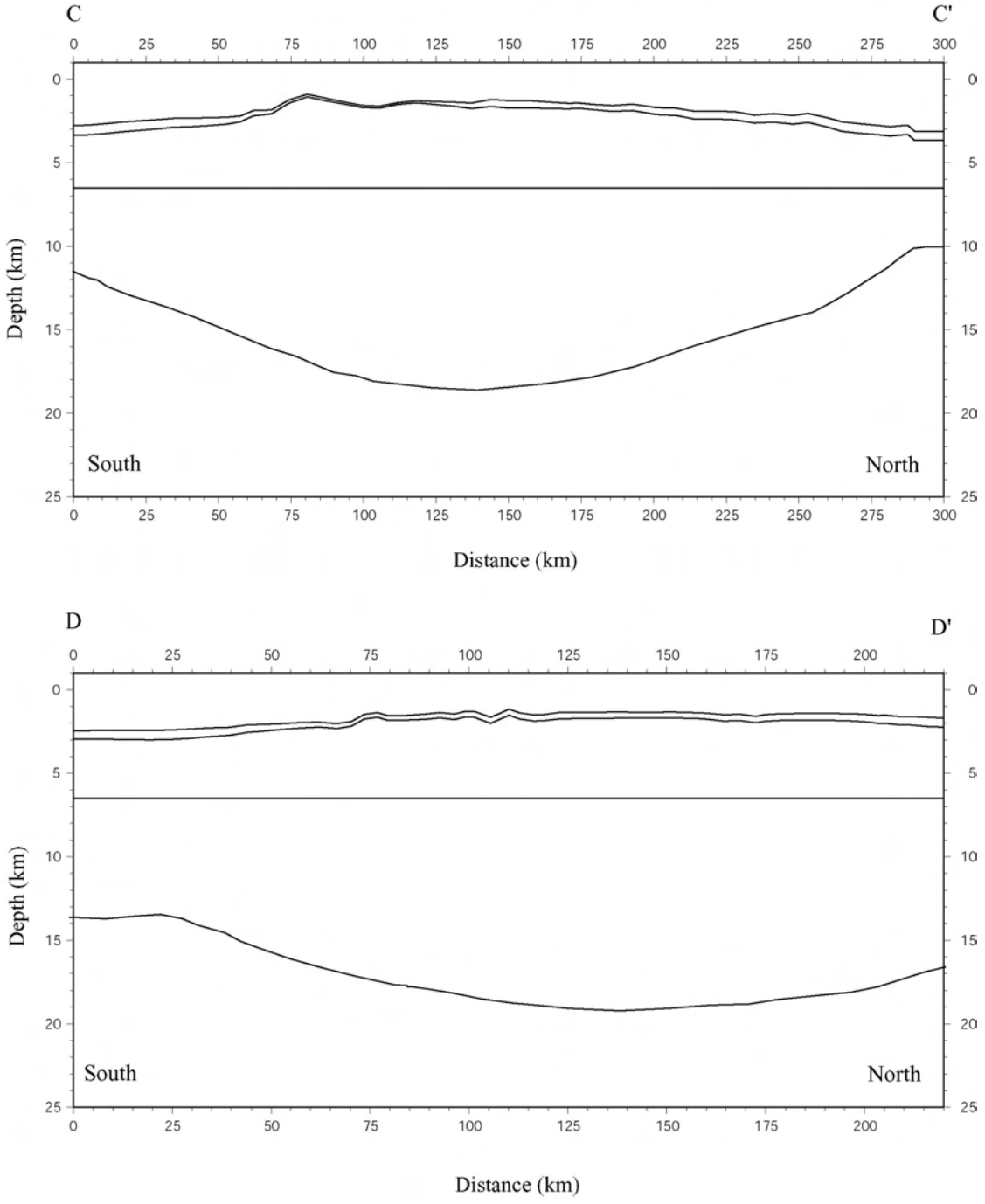

Figure 11. Crustal models along transect C-C' (upper crustal model) and D-D' (lower crustal model). The location of these transects is shown in Figure 9.

This grid includes not only the eastern segment of Carnegie Ridge where model structures were built and evaluated (between ~81.5° W and 86° W), but also its western segment between 86° W and 89° W where the presence of an Airy type compensation has been found to account satisfactorily for the observed gravity anomaly field [*Feighner and Richards*, 1994]. The isostatic crustal thickness grid was in turn employed to define an excess crustal thickness grid (the thickness of normal oceanic crust excluded) for the study area. The significance in determining this gridded data set is that it provided a practical way to derive excess crustal volume at any ridge segment. The definition of excess crustal volume on regions of known age was in turn employed to calculate the crustal volume flux through time at Carnegie Ridge.

2.3.1. Isostatic Crustal Thickness and Excess Crustal Thickness Grids Calculation

The isostatic crustal thickness grid and excess crustal thickness grid for Carnegie Ridge were calculated by initially defining an isostatic Moho depth grid for this region. The latter was determined by first converting the predicted bathymetry and estimated sediment thickness grids into tables containing X (latitude) Y (longitude) Z (depth – sediment thickness) data. Because of the different resolution between the predicted bathymetry grid (2 min) and the estimated sediment thickness grid (5 min), bathymetry data were obtained only for those points where sediment thickness is available. Although the way in which bathymetry data were determined reduced its resolution (from 2 min to 5 min), I consider that it did not affect significantly the estimated long-wavelength Moho geometry. Predicted bathymetry and estimated sediment thickness data were employed to calculate the height of the bathymetric edifice for each one of the points where such

data were obtained. The isostatic Moho depth (h_{root}) at each one of these points was then determined by utilizing equation (1). The Moho depth data were gridded with a grid spacing (i.e., resolution) of 5 min both in the X (longitude) and Y (latitude) directions, which correspond to that of the other gridded data sets.

Once the isostatic Moho depth grid was determined, I defined the isostatic crustal thickness grid for the study area by first adding the predicted bathymetry and the estimated sediment thickness grids in order to produce a basement grid and then, by subtracting this grid from the estimated Moho depth grid. The excess crustal thickness grid for Carnegie Ridge was determined by subtracting from the isostatic crustal thickness grid the thickness of normal oceanic crust (i.e., 7 km).

2.3.2. Crustal Volume Flux Calculation

In order to calculate crustal volume flux through time at Carnegie Ridge, I initially determined an age grid for this region. The data used to define this grid were obtained by digitizing ridge isochrons (Figure 12) from a map of age predictions for the hot spot traces of the GVP [*Meschede and Barckhausen*, 2001]. This data set was gridded with a 5 min grid spacing (i.e., resolution) both in the X (longitude) and Y (latitude) directions.

Once the age grid was determined, I obtained the values for each node within a polygon defining long-wavelength morphology of eastern and western Carnegie Ridge. In order to reduce the uncertainty and errors that a visually chosen polygon may have in the later calculation of excess crustal volume and crustal volume flux through time (i.e., to include in these calculations thickened segment of oceanic crust outside the ridge), I employed a bathymetric contour to define this polygon and subsequently the region

where such calculations were performed. The 2400 m contour was found to account adequately for the long-wavelength ridge morphology. The region within this polygon was then divided into a series of square regions whose center is defined by the location of the estimated age grid nodes, and whose side length is equal the node interval (i.e., grid spacing) (Figure 13). The age within each region was assumed to be constant and the same as the value of their central nodes. The excess crustal thickness at the center of these regions was determined by sampling the estimated excess crustal thickness grid at each age grid node. Excess crustal volume for each region was then derived by multiplying its area times the excess crustal thickness value at its central point. The calculated excess crustal volumes were sorted by age and divided into age intervals of 0.5 m.y. The crustal volume flux through time at Carnegie Ridge was finally determined by dividing the sum of the calculated excess crustal volumes at each interval by the time span represented by such intervals.

2.3.3. Crustal Volume Flux Variations and Tectonic Implications

Based on the analysis of bathymetric and magnetic data, it has been proposed [*Hey*, 1977; *Barckhausen et al*., 2001] that the recent tectonic evolution of the GVP was characterized by a major southward jump of the CNSC at ~14.5 Ma that placed the GHS beneath the Cocos Plate. The CNSC eventually passed over the GHS as a result of its northward migration between ~9 Ma and ~7 Ma, placing GHS beneath the Nazca Plate [*Wilson and Hey*, 1995]. Since then, the CNSC has been moving away from the GHS to reach the location observed today. Although changes in the relative location of the CNSC with respect to the GHS are considered to explain the observed differences in

amount of volcanic material emplaced on each side of the spreading center [*Hey*, 1977; *Sallarés and Charvis*, 2003], the amount of such emplacement on the Cocos and Nazca plates remain uncertain [e.g., *Barckhausen et al.*, 2001].

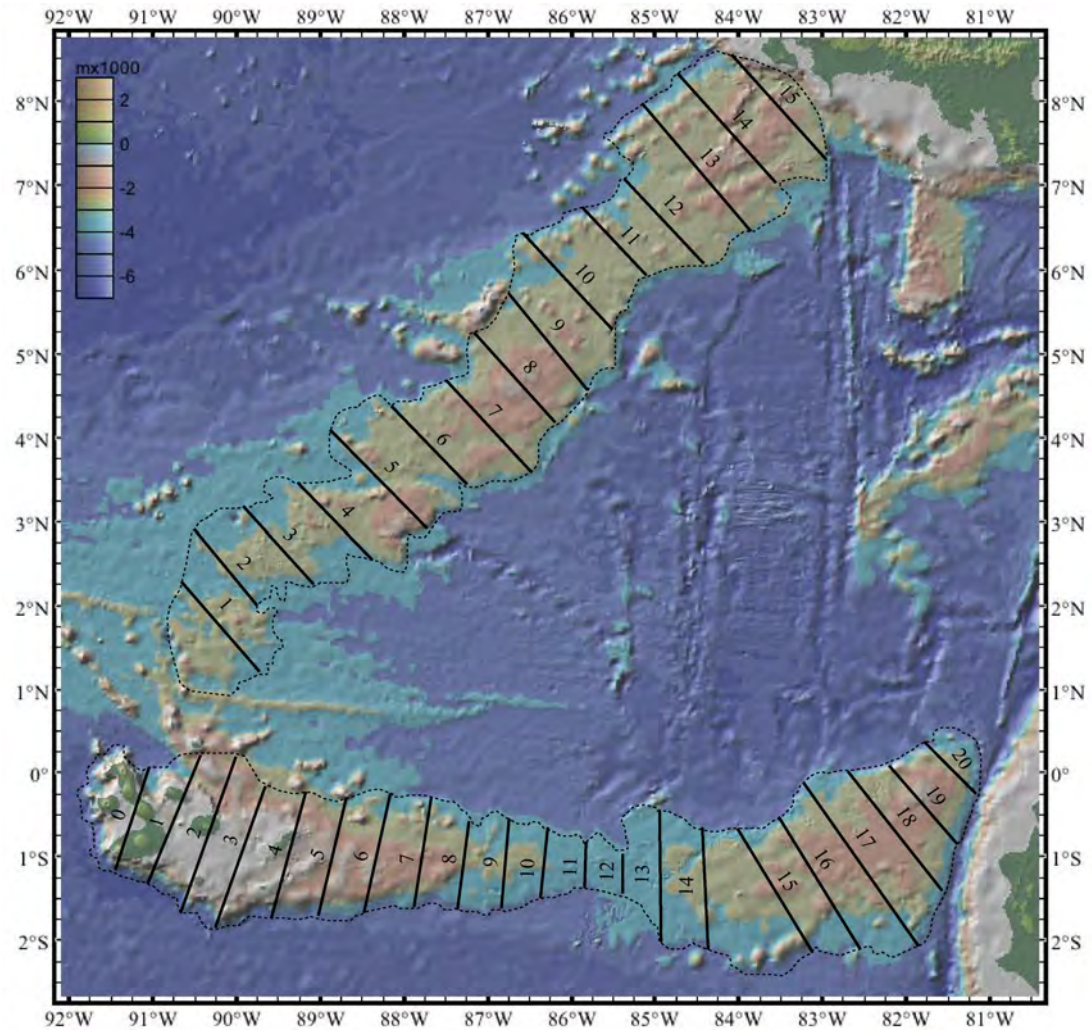

Figure 12. Predicted age isochrons on the Galápagos Archipelago, Carnegie Ridge, and Cocos Ridge. The dotted lines represent the polygons where crustal volume flux was calculated. Modified from *Meschede and Barckhausen* [2001].

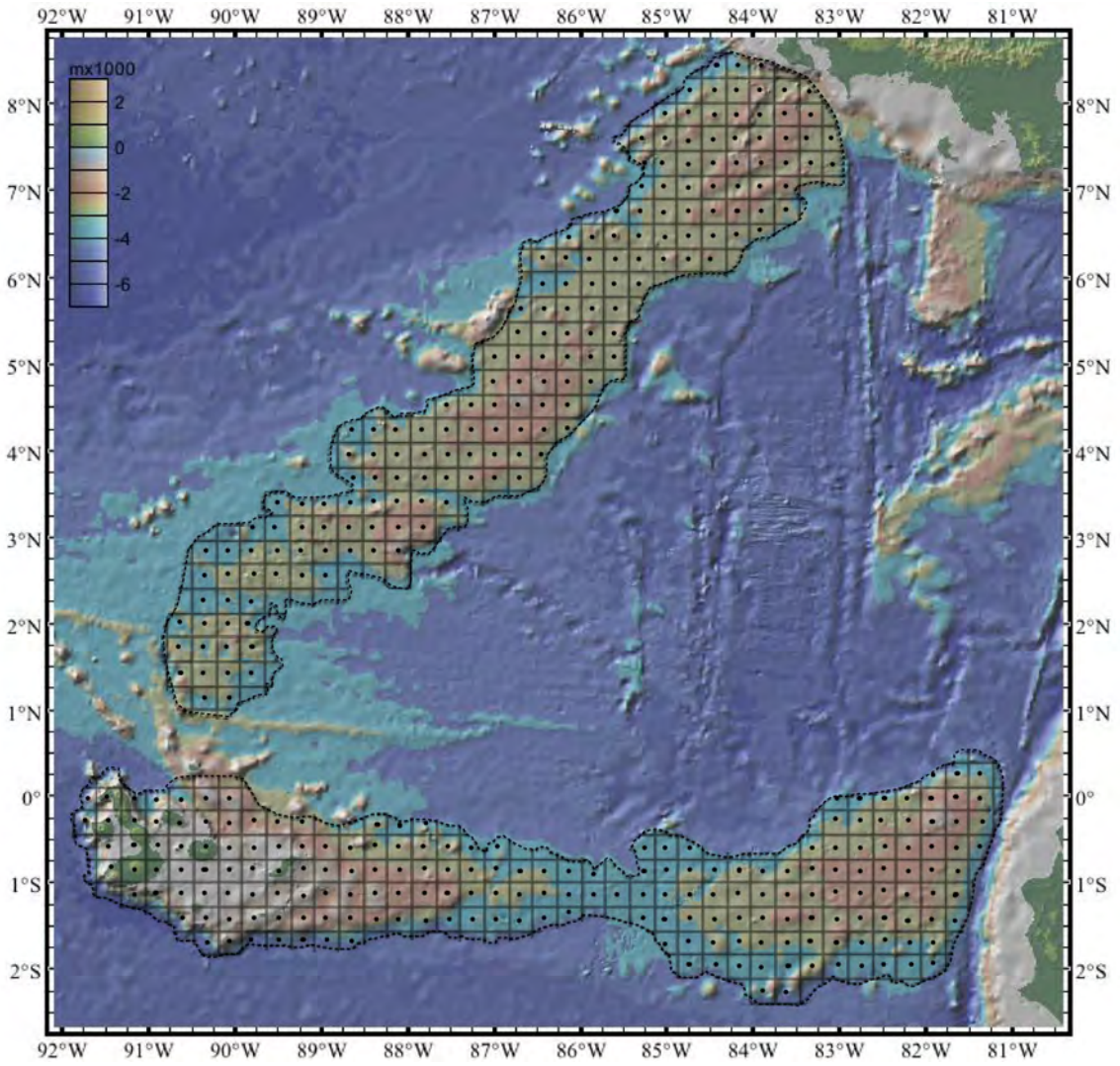

Figure 13. Crustal volume flux calculation. This cartoon shows the way in which the ridge was divided into square regions with a central point defined by the location of the estimated age grid nodes (black dots, not all shown in this figure) and a side length equal to the node interval (not at scale in this figure).

Based on this consideration, and as a final step in this study, I calculated the crustal volume flux at the hot spot traces emplaced on the Nazca and Cocos plates in order to

establish the relative differences in the amount of volcanic material emplaced on each plate. This objective was accomplished by including in my calculation of crustal volume flux of both the Galápagos Archipelago (between ~89° W and ~92° W) and Cocos Ridge. The Galápagos Archipelago along with the western and eastern segments of Carnegie Ridge are a record of volcanic material emplaced on Nazca plate during the last ~20 m.y, whereas the Cocos Ridge is the same for the volcanic material emplaced on the Cocos plate during the last ~15 m.y. Hot spot traces older than 15 m.y on the Cocos Plate (i.e., Coiba, Regina, and Malpelo ridges) were excluded from my calculation of crustal volume flux through time because of uncertainties regarding their origin, tectonic evolution, and age. Therefore, any further analysis regarding such calculations and particularly their comparison relative to the results obtained at the Galápagos Archipelago and Carnegie Ridge will be limited to the last 15 m.y.

By assuming that all the volcanic material produced by the GHS is partitioned between the volcanic ridges of the GVP and that this material corresponds to the excess crustal thickness on these ridges, the calculated crustal volume flux at the Galápagos Archipelago and Carnegie Ridge, and at Cocos Ridge can be taken as a measure of the excess melt flux provided by the GHS [e.g., *Sallarés and Charvis*, 2003]. Based on this consideration, the calculated crustal volume flux values at the Galápagos Archipelago and Carnegie Ridge were added to their corresponding values in age at Cocos Ridge in order to define the total crustal volume flux provided by the GHS during the last 15 m.y. *Sallarés and Charvis* [2003] suggested that crustal volume flux can be taken as a measure of the along-axis intensity of the hot spot. Based on this consideration, the

calculated total crustal volume flux is assumed to represent the total intensity of the GHS during the last 15 m.y. The calculated total volume output of the GHS was employed to evaluate whether the variations in the calculated crustal volume flux at the Galápagos Archipelago and Carnegie Ridge, and at Cocos Ridge can exclusively be explained as the result of changes in the relative distance between the CNSC and the GHS [e.g., *Hey*, 1977; *Meschede and Barckhausen*, 2001; *Barckhausen et al*, 2001; *Sallarés and Charvis*, 2003].

Similar to the case of Carnegie Ridge, the crustal volume flux at the Galápagos Archipelago and Cocos Ridge was calculated by initially defining the following gridded data sets for these regions: crustal thickness, excess crustal thickness, and age. Regarding the crustal thickness and excess crustal thickness gridded data sets, they were defined by assuming Airy isostasy and employing the same crustal densities used to define these grids on Carnegie Ridge. The procedure used to define crustal thickness and excess crustal thickness grids on the Galápagos Archipelago and Cocos Ridge corresponds to that employed on Carnegie Ridge (section 2.3.1.). The presence of an Airy type compensation on Cocos Ridge is thought to be consistent with the its formation near the CNSC (i.e., volcanic material forming the ridge is emplaced on oceanic lithosphere with low elastic plate thickness). On the other hand, the results of gravity and geoid modeling on the Galápagos Archipelago suggest that only its eastern and central parts (between ~89° W and ~91° W) are locally compensated (i.e., Airy compensation), whereas its western part is regionally supported by elastic flexure of the lithosphere [*Feighner and Richards*, 1994]. The implications of assuming local Airy

isostasy in my estimations of crustal thickness and excess crustal thickness, and the later calculation of crustal volume flux on the western part of the Galápagos Archipelago is discussed on Chapter IV.

The age grids for the Galápagos Archipelago and Cocos Ridge were defined according to the procedure described in section 2.3.2. The orientation of the predicted isochrons on Cocos Ridge [*Meschede and Barckhausen*, 2001] was modified in order to obtain isochrons with an orientation nearly perpendicular to the along-axis direction of the ridge (i.e., similar to the predicted isochrons on the Galápagos Archipelago and Carnegie Ridge).

Once the isostatic crustal thickness, excess crustal thickness and age grids were determined, the crustal volume flux at the Galápagos Archipelago and Cocos Ridge was estimated following the procedure described in section 2.3.2. (Figure 13). These calculations were performed within polygons similar to that employed on Carnegie Ridge. In the case of the Galápagos Archipelago, this boundary polygon corresponds to the 2400 m bathymetric contour (i.e., the same as that for Carnegie Ridge), whereas for Cocos Ridge it is defined by the 2200 m bathymetric contour (Figure 13).

CHAPTER III

RESULTS

3.1. Model Testing

The gravity anomaly over the crustal models determined along reference transects 1 and 2 and along transects A-A' through D-D' was calculated and compared with observed data in order to assess the consistency of the estimated model structures. Because of the lack of shipboard free-air gravity data along the reference transects, the observed data was obtained from the 2 min resolution gravity anomaly grid derived from satellite altimetry [*Sandwell and Smith*, 1997].

3.1.1. Identification of Potential Sources of Error

Along reference transect 1 (Figure 14), the calculated gravity anomaly fits well the observed data, with an overall misfit of ~10 mGal to ~15 mGal. Because of its small amplitude and short-wavelength, I consider that the observed misfit is related to the inaccurate definition of bedrock relief in my crustal model. In order to test this assumption, I initially evaluated the extent to which the approach used to define basement geometry in my crustal models (section 2.2.2.) might have incorrectly estimated its real configuration along transect 1. This objective was accomplished by first employing a similar approach to define bedrock relief along a ridge transect (transect 3) whose upper crustal geometry has been resolved from seismic data (Figure 15), and then by comparing the estimated and seismic basement structures. The absence

of seismic reflection data along transect 1 prevented any attempt to perform this evaluation directly.

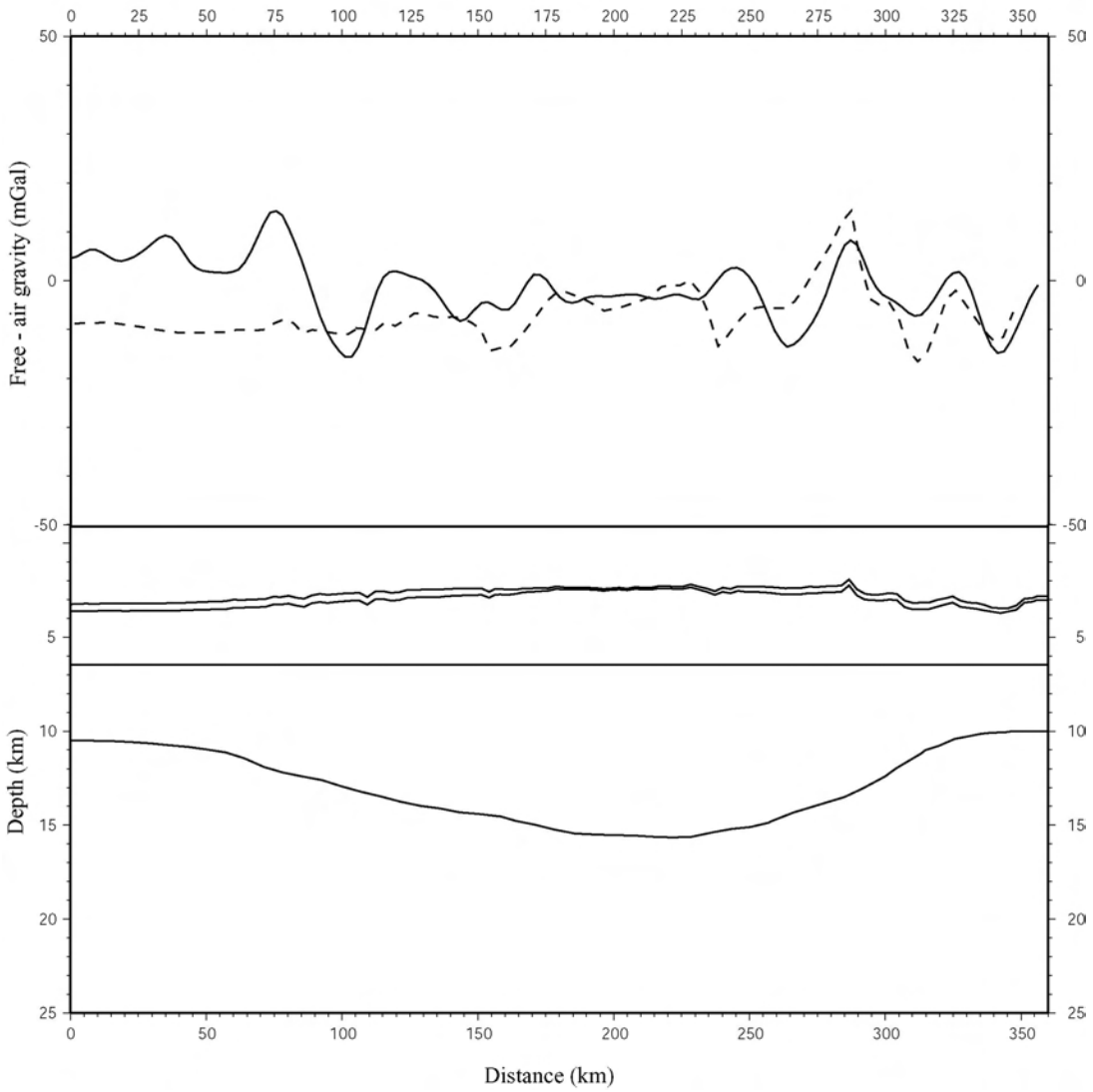

Figure 14. Gravity modeling solution along reference transect 1. The solid line represents the observed gravity anomaly field, whereas the dashed line corresponds to the calculated gravity anomaly field. The crustal model is shown in the bottom panel.

In contrast to the gentle basement geometry and uniform sediment distribution estimated along transect 3, seismic reflection profiling shows a rough bedrock relief characterized by the presence of sediment-free basement highs and volcanic peaks, and large basement offsets, with a preferential accumulation of sediments in depressions of the rough volcanic surface.

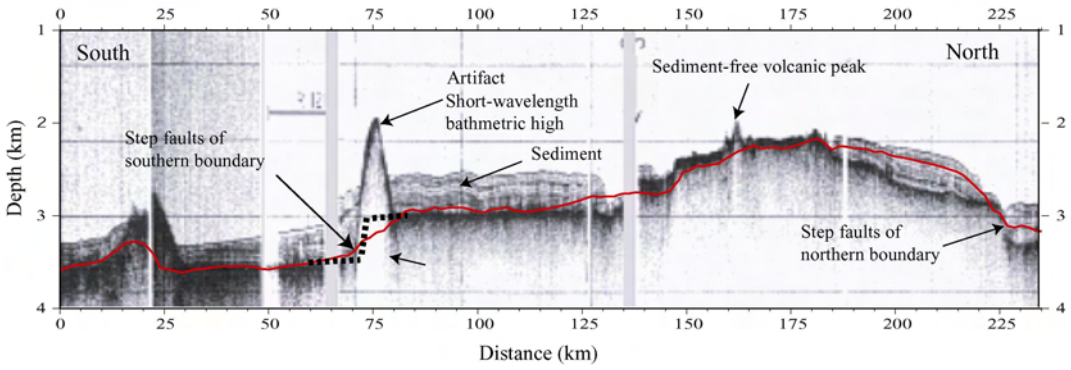

Figure 15. Seismic reflection profile along transect 3 showing the main features of its rough bedrock relief. For location of this profile see Figure 17. The solid red line shows the basement geometry estimated in my crustal model by adding estimated sediment thickness values to the predicted bathymetry data. The doted line on the southern part of this profile (between 65 km and 70 km) defines the probable geometry of a large step fault similar to that observed the northern flank of the ridge. Reflections from this large basement offset are thought to have been masked by the acoustic diffraction produced by a short-wavelength conspicuous bathymetric high located in this region. Modified from Geological Society of America Bulletin, 82, van Andel et al., Tectonics of the Panama Basin, Eastern Equatorial Pacific, 1489-1508, Copyright (1971), with permission from the Geological Society of America.

Lonsdale [1978] pointed out that as result of this uneven sediment distribution, the irregular bedrock relief of eastern Carnegie Ridge has been smothered and its geometry subsequently underestimated on the observed topography. Based on this observation, I consider that the absence of well defined surface expression related to irregular basement structures might have affected their accurate definition in my crustal models given that bedrock relief was determined by adding estimated sediment thickness values to predicted bathymetry data.

In order to evaluate the extent to which the underestimated bedrock relief has affected the gravity anomaly field calculated along transect 3, I initially calculated the gravity anomaly field over a crustal model whose upper crustal geometry was defined according to the approach defined in section 2.2.2. Under these conditions, the calculated gravity anomaly fits well the observed data along most of this transect (overall mean misfit of < ~10 mGal), with exception of those regions where the geometry of irregular basement structures (i.e., step faults, sediment-free volcanic peaks) has been poorly defined (Figure 16). Notice that the misfit along this transect resembles in amplitude and wavelength the misfit observed along transect 1. Because of the lack of shipboard free-air gravity data along transect 3, the observed data was obtained from a 2 min resolution gravity anomaly grid derived from satellite altimetry [*Sandwell and Smith*, 1997]. As a second step, I modified my crustal model by replacing the estimated bedrock relief with that resolved from seismic data, and recalculated the gravity anomaly field over the new model structure (Figure 16). With this new model structure, the fit between calculated and observed gravity data improved significantly in regions where

the geometry of irregular basement structures was corrected (overall mean misfit of < ~5 mGal). The error caused by a basement approximation was found to be ~5 mGal over short-wavelength bathymetric highs, and ~10 mGal over normal faults with large vertical offsets.

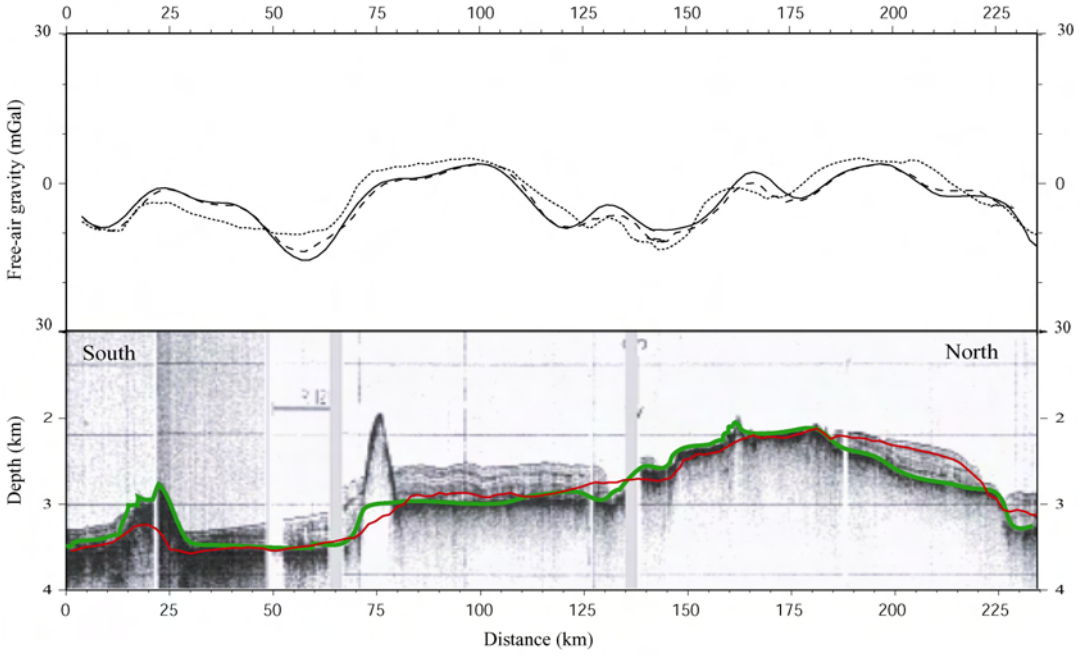

Figure 16. Gravity modeling solution along transect 3. The solid line represents the observed gravity anomaly field. In model A (dotted line) the gravity anomaly was calculated over a crustal model with estimated basement geometry (solid red line in the seismic section). In model B (dashed line) the gravity anomaly was calculated over a crustal model whose basement geometry corresponds to the bedrock relief resolved from seismic data (green line). The presence of a gravity anomaly low at ~65 km is thought to be related to the presence of a large step fault on the southern part of this transect. A similar response occurs on the northern flank of the ridge where a comparable basement structure is observed.

Based on these observations it is clear that without seismic data to define basement geometry, many of the small, short-wavelength anomalies that characterized the observed gravity anomaly field cannot be adequately reproduced by gravity modeling. Similar to the case of transect 3, an inaccurate bedrock relief definition is thought to be associated to the short-wavelength features that could not be adequately reproduced by gravity modeling along transect 1. These features correspond to a trend of positive gravity anomalies of ~5 mGal to ~15 mGal along the oceanic basin (between 0 km and ~70 km), followed by a negative gravity anomaly of ~ -15 mGal at the southern edge of the ridge (~90 km). The former appears to be caused by local short-wavelength bathymetric highs whose geometry is not properly represented in my crustal model as result of the differential accumulation of sediments on its flanks. On the other hand, the continuous and nearly linear trend that characterizes the observed negative gravity anomaly at the edge of the ridge (Figure 17) suggests that this low is produced by a continuous, linear subsurface depression, probably a basement offset whose real geometry has been masked by a thick sediment cover. This structure is thought to be related to a series of normal faults with large vertical offsets of ~200 to ~500 m, which bound Carnegie Ridge on its southern and northern flanks [*van Andel et al*., 1971] (e.g., Figure 15).

The influence of well defined bathymetric highs and large basement offsets on the calculated gravity anomaly field along transect 1 is thought to resemble the conditions observed along transect 3 (Figure 16), where the accurate definition of these structures resulted in a good fit between calculated and observed gravity anomaly data. Based on

this consideration, my crustal model along transect 1 was modified on its southern flank by nearly eliminating sediment cover over local short-wavelength bathymetric highs, and by increasing the basement offset located at the edge of the ridge by ~350 m (Fig. 18). The new crustal model resulted in a good fit between calculated and observed gravity anomaly data, with an overall mean misfit of < ~10 mGal.

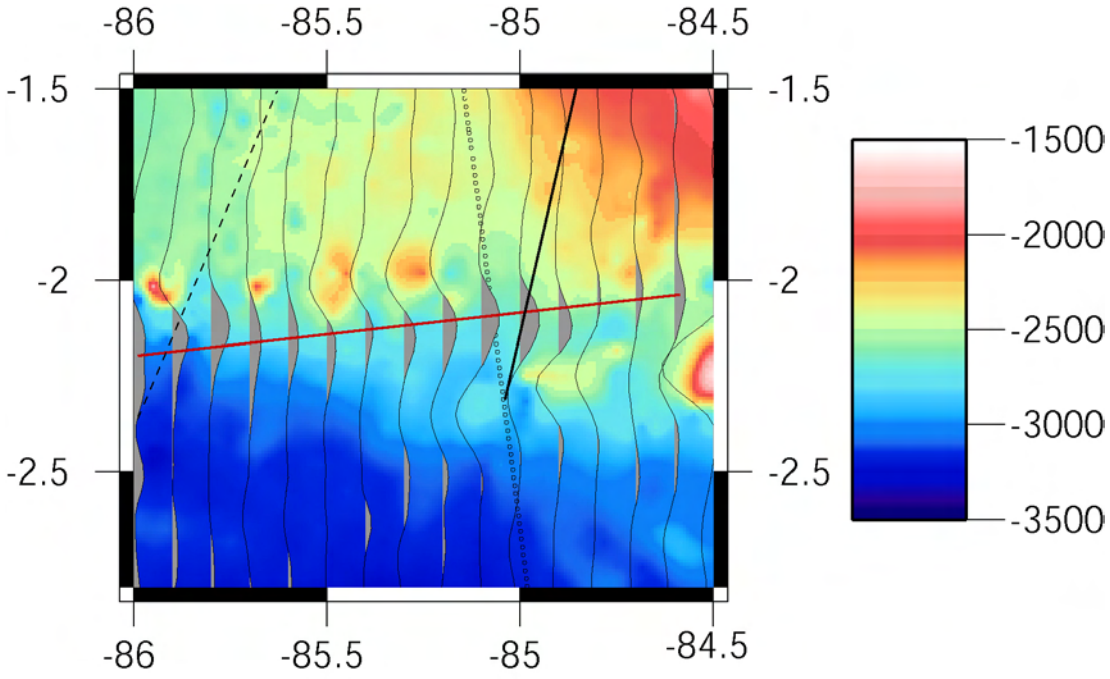

Figure 17. Observed gravity anomaly field around reference transect 1. The wiggles represent the observed gravity anomalies. The dotted black line shows the location of reference transect 1. The dashed black line shows the location of the seismic reflection profile shown in Figures 15 and 16. The solid black line shows the location of transect A-A'. Negative gravity anomalies have been shaded (grey) in order to show the linear trend (solid red line) of a prominent gravity anomaly low along the southern edge of the ridge.

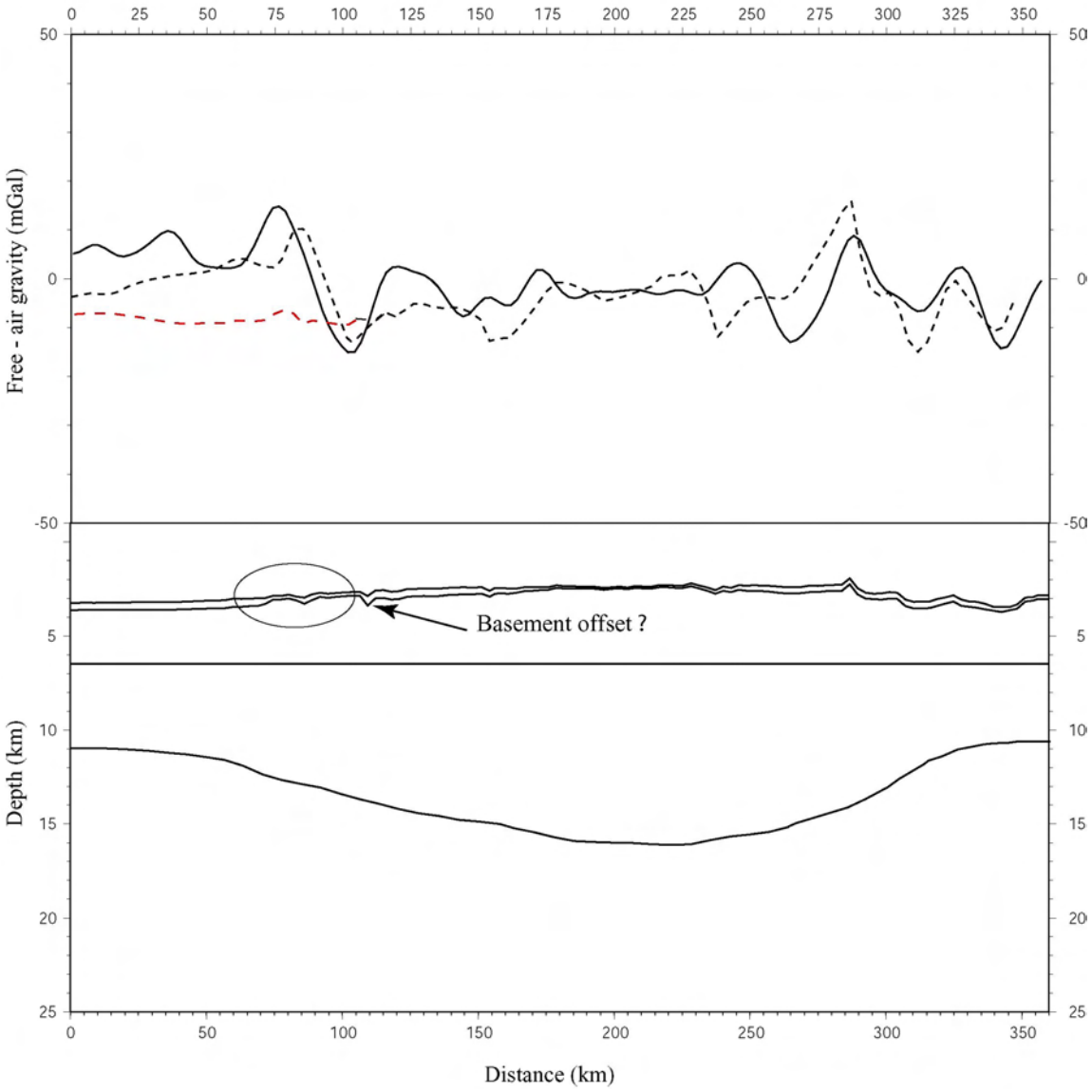

Figure 18. Gravity modeling solution along reference transect 1 (corrected bedrock relief). The solid black line represents the observed gravity anomaly field, whereas the dashed black line corresponds to the calculated gravity anomaly field. The dashed red line corresponds to the gravity anomaly field originally calculated on the southern part of this transect (Figure 14) by employing an estimated bedrock relief in my model structure. In the new crustal model (bottom panel), sediment cover over short-wavelength bathymetric highs was nearly eliminated (region within the ellipsoid), and the depth of a basement offset observed at the edge of the ridge was deepened by ~350 m.

Along transects A-A' the calculated gravity anomaly fits well the observed data, with a overall mean misfit of ~10 mGal to ~15 mGal (Figure 19). Similar to the case of transect 1, I consider that some of the observed misfit is related to the inaccurate definition of bedrock relief in my crustal model. The major source of error along this transect comes from its southern flank, at ~15 km, where a negative anomaly of ~15 mGal was not reproduced by the initial gravity model. Because of its characteristic amplitude and wavelength, as well as its distinctive linear trend (Figure 17), this low is thought to be related to a series of normal faults similar to those defined at the edge of the ridge along transects 1 and 3. Based on these observations, the model structure along transect A-A' was modified on its southern flank by increasing the vertical offset of this irregular basement structure. The new crustal model resulted in a good fit between calculated and observed gravity anomaly data, with an overall mean misfit of < ~10 mGal (Figure 20).

Along transects B-B', C-C' and D-D', the presence of 3-D seamount-like structures and a series of short-wavelength bathymetric highs increased the uncertainty of the bedrock relief defined in my crustal models. This problem was determined by comparing the interpretation of a seismic reflection profile collected along transect B-B' (Figure 21a) with the upper crustal geometry defined in my model structure (Figure 21b). The bedrock relief resolved from seismic data shows a rough volcanic surface characterized by the presence of pronounced sediment-free basement peaks and bathymetric highs, with a preferential accumulation of sediments on their flanks. On the other hand, the geometry of these structures has been underestimated in my crustal model as result of

the thick sediment cover defined both at the crest of these elevations as well as in depression of the rough volcanic surface.

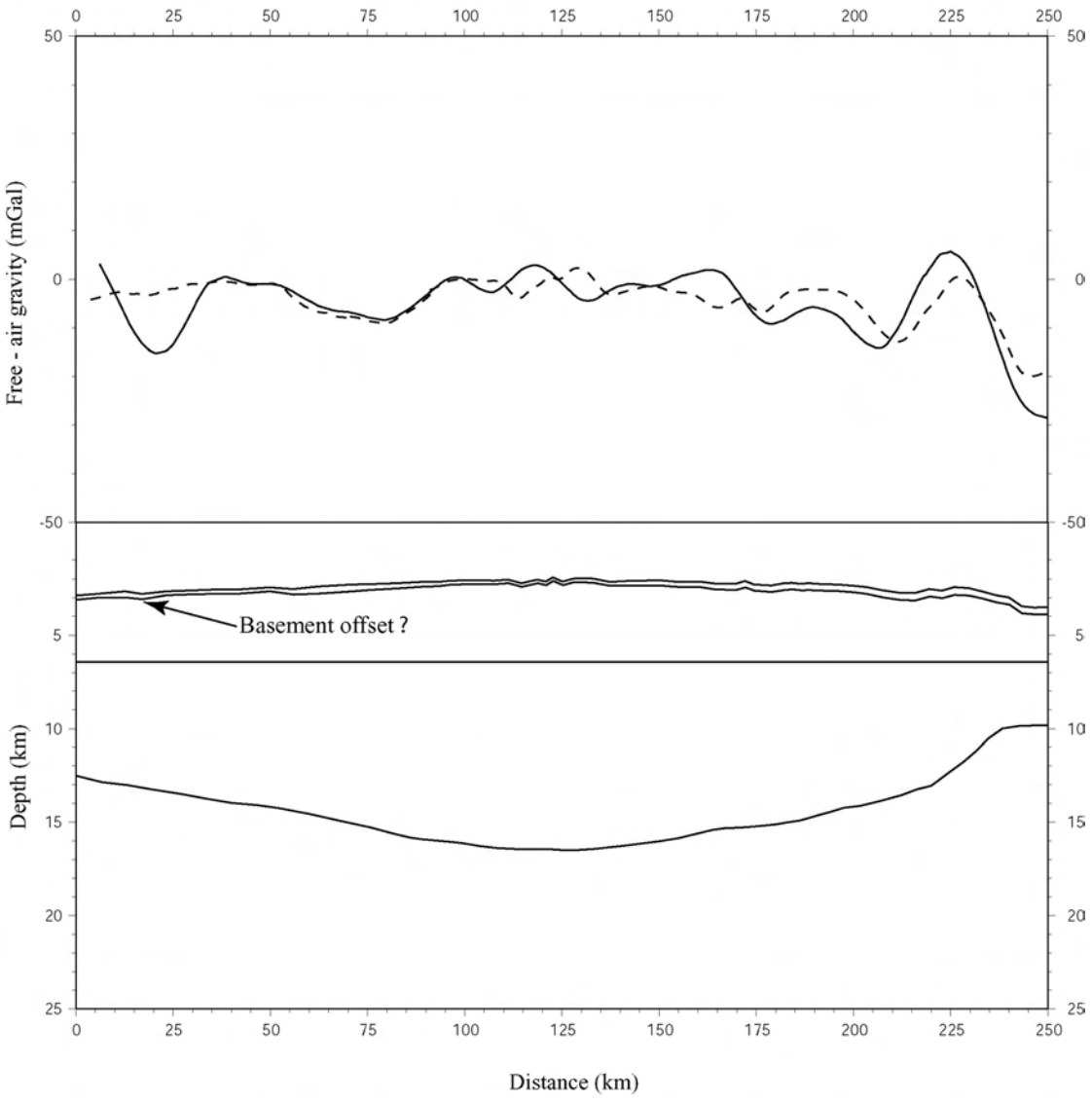

Figure 19. Gravity modeling solution along transect A-A'. The solid line represents the observed gravity anomaly field, whereas the dotted line corresponds to the calculated gravity anomaly field. The arrow in the crustal model (bottom panel) shows the probable location of a pronounced basement offset.

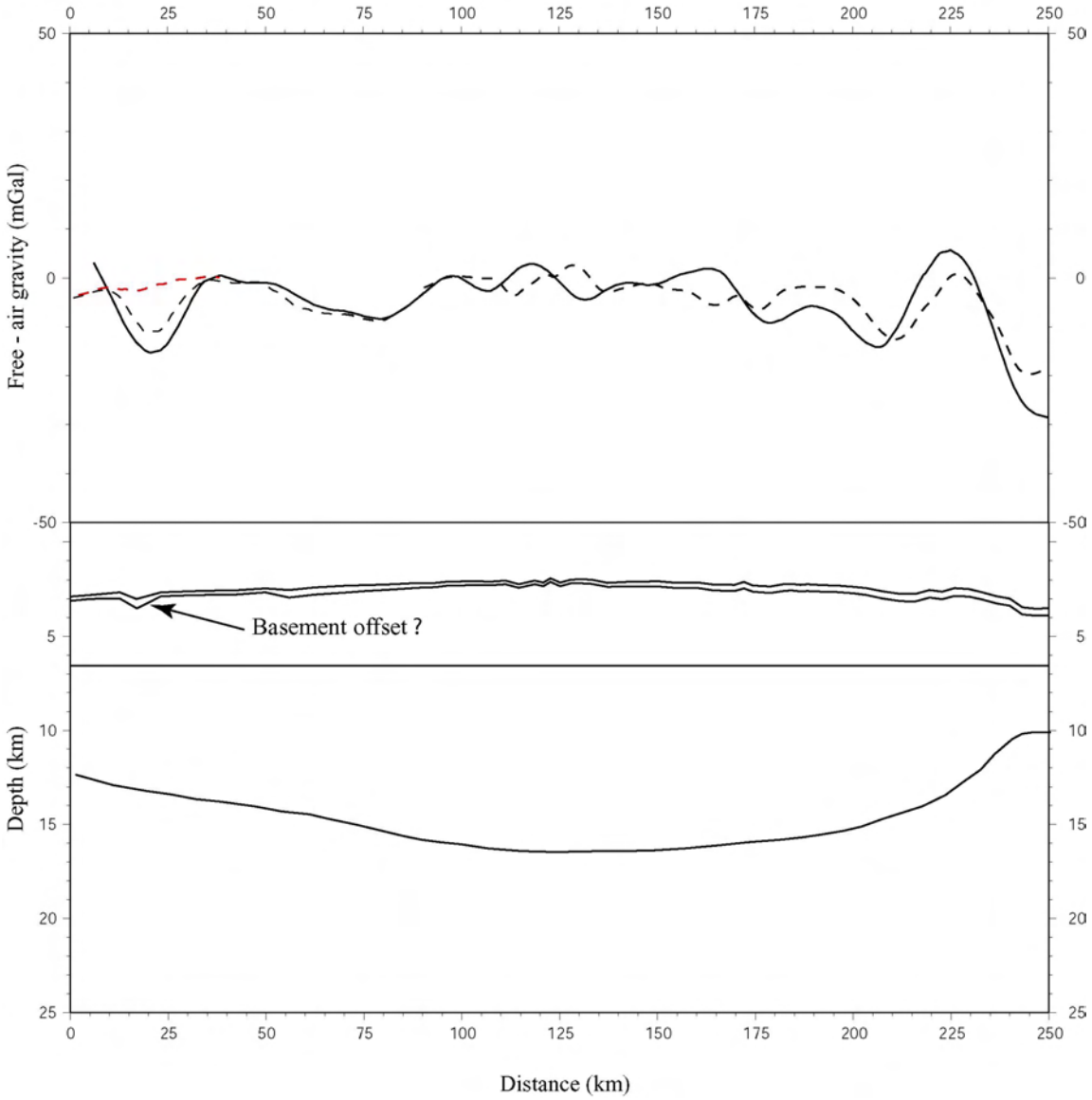

Figure 20. Gravity modeling solution along transect A-A' (corrected bedrock relief). The solid black line represents the observed gravity anomaly field, whereas the dashed black line corresponds to the calculated gravity anomaly field. The dashed red line corresponds to the gravity anomaly field originally calculated on the southern part of this transect by employing an estimated bedrock relief in my model structure (Figure 19). In the new crustal model (bottom panel), the depth of a basement offset observed at the edge of the ridge was deepened by ~350 m.

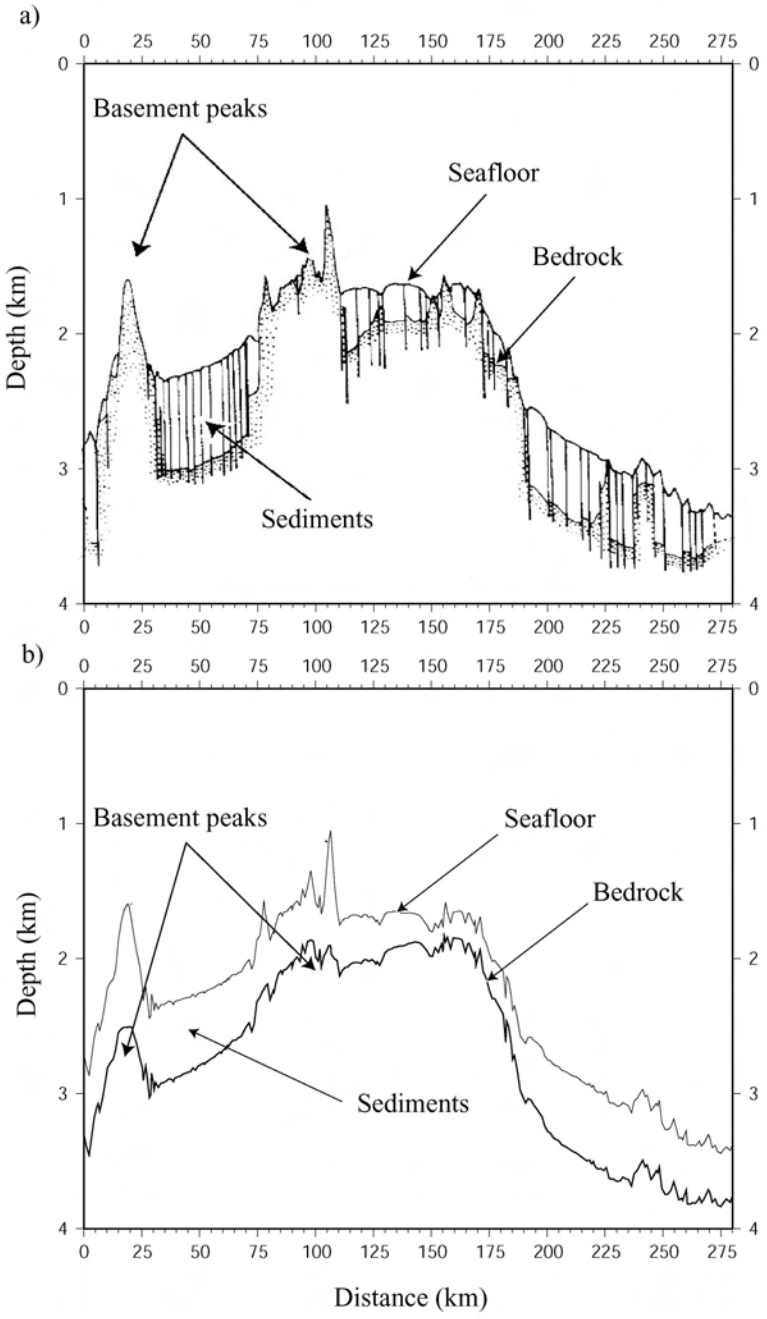

Figure 21. Comparison of seismically determined (a) and estimated (b) bedrock relief along transect B-B'. The upper figure was modified from Geological Society of America Bulletin, 82, van Andel et al., Tectonics of the Panama Basin, Eastern Equatorial Pacific, 1489-1508, Copyright (1971), with permission from the Geological Society of America.

Despite the lack of seismic reflection data along transects C-C' and D-D', I consider that the uneven sediment distribution and particularly the extent to which it has affected the geometry of 3-D seamount-like structures and short wavelength bathymetric highs in my crustal models would resemble the conditions observed on transect B-B'. Based on these considerations, the upper crustal geometry along transects C-C', and D-D' was modified by correcting the areas of preferential sediment accumulation as well as those with no sediment cover. Regarding transect B-B', the observed misfit between calculated and observed gravity anomaly data (Figure 22) was reduced by eliminating sediment cover at the top of two prominent seamount like structures located at ~15 km, and between ~65 km and 100 km. In the corrected crustal model, the calculated gravity anomaly fits well the observed data, with an overall mean misfit of ~5 mGal to 10 mGal (Figure 23). Similar to the case of transect B-B', the observed misfit along transects C-C' (Figure 24) and D-D' (Figure 25) was reduced by adjusting sediment cover both at the top as well on the flanks of short wavelength bathymetric highs, which in turn redefined the upper crustal geometry along these transects.

Because of the lack of seismic reflection data, these changes were made to an arbitrary degree until a good fit between calculated and observed gravity anomaly data was obtained. The gravity anomaly calculated over the new crustal models along transect C-C' (Figure 26) and D-D' (Figure 27) fits well the observed gravity anomaly field, with and overall mean misfit of ~10 mGal.

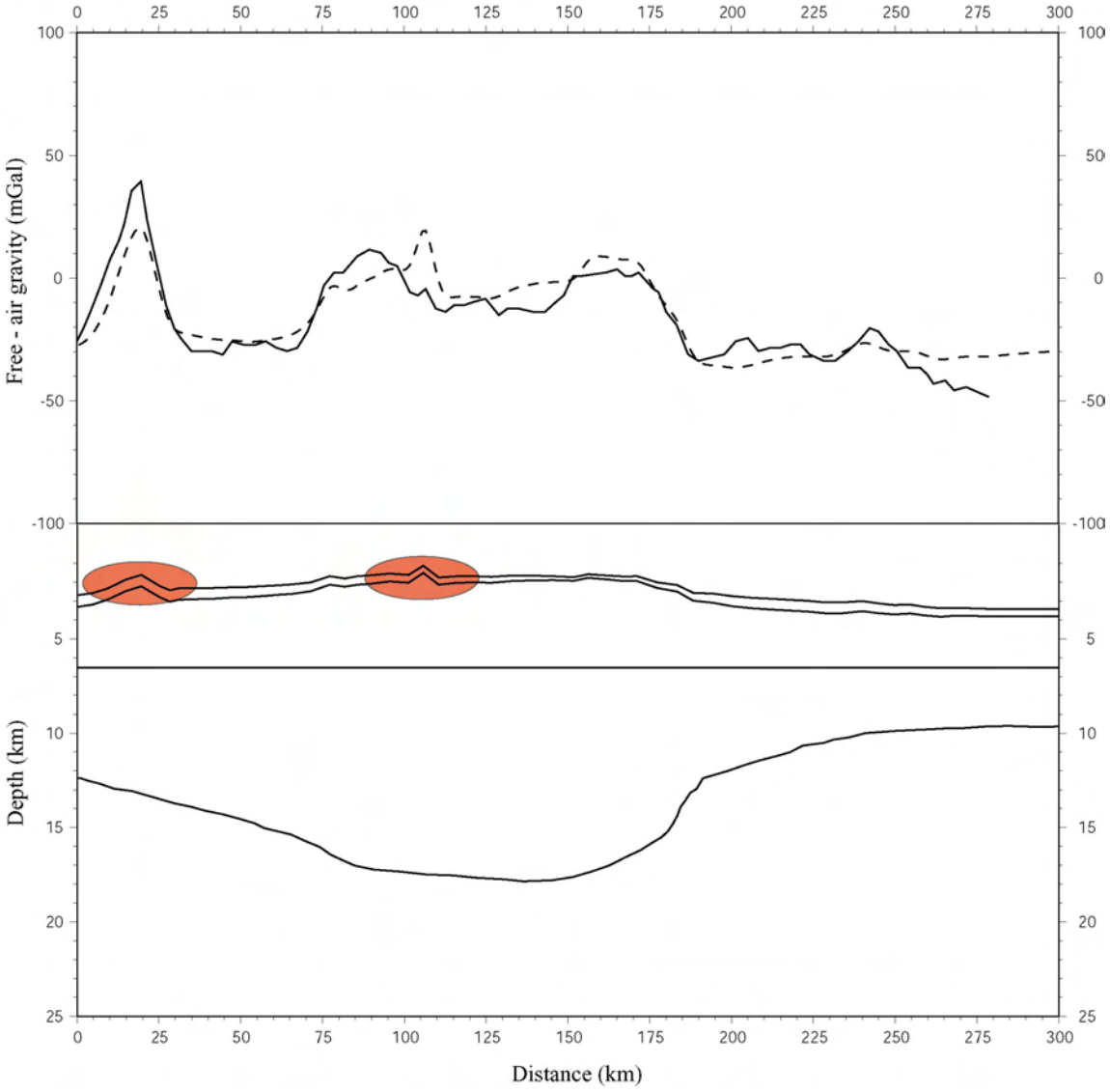

Figure 22. Gravity modeling solution along transect B-B'. The solid line represents the observed gravity anomaly field, whereas the dashed line corresponds to the calculated gravity anomaly field. The red ellipsoids in the crustal model (bottom panel) enclose 3-D basement peaks whose real geometry has been underestimated as result of an overestimated sediment cover at their top as well as on their flanks (Figure 21b).

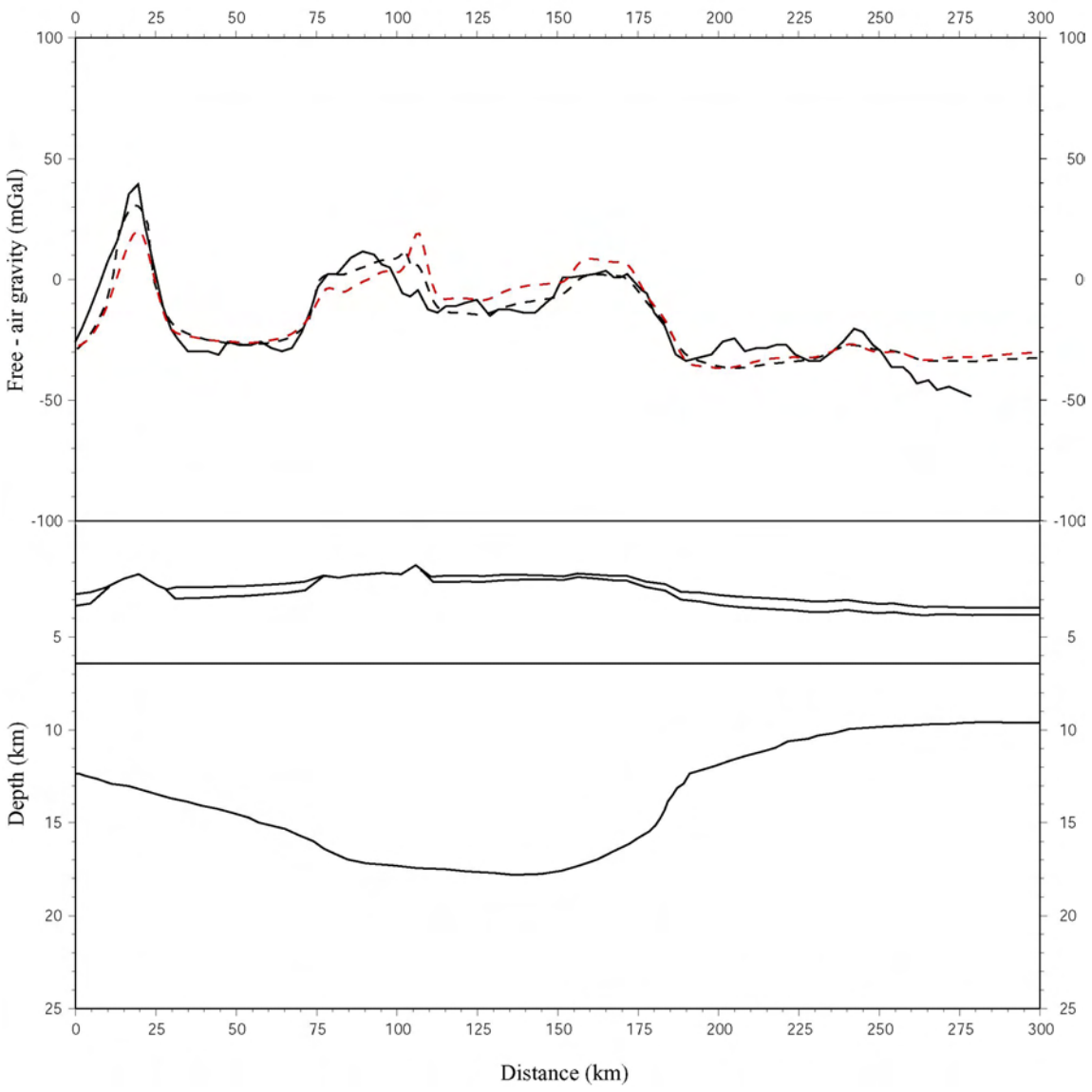

Figure 23. Gravity modeling solution along transect B-B' (corrected bedrock relief). The solid black line represents the observed gravity anomaly field, whereas the dashed black line corresponds to the calculated gravity anomaly field. The dashed red line corresponds to the gravity anomaly field originally calculated by employing an estimated bedrock relief in my model structure (Figure 21b).In the new crustal model (bottom panel), the upper crustal geometry along this transect was modified according to the bedrock relief resolved form seismic data (Figure 21a).

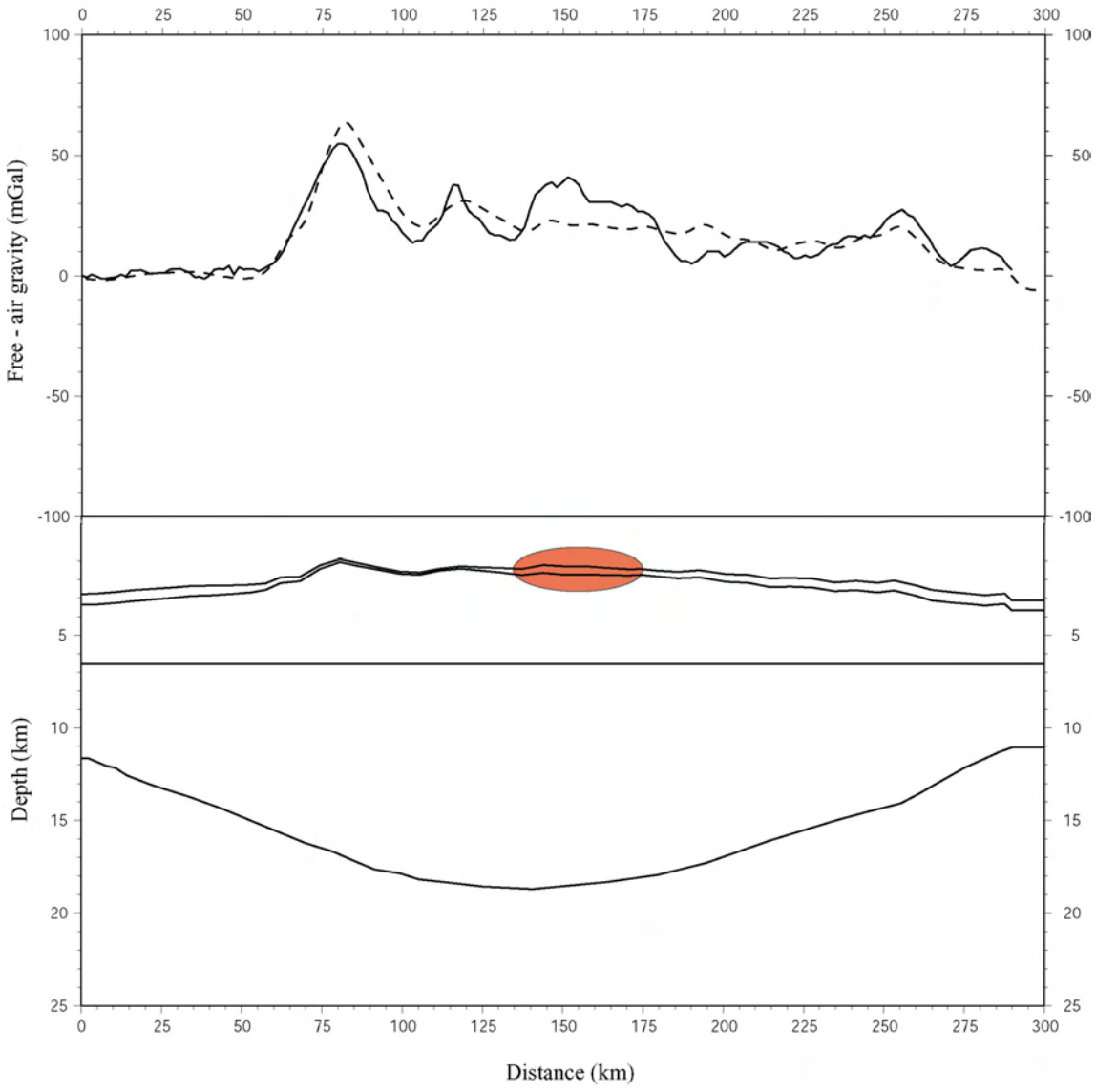

Figure 24. Gravity modeling solution along transect C-C'. The red ellipsoid in the crustal model (bottom panel) encloses a local short wavelength bathymetric high whose real geometry is thought to has been underestimated as result of the inaccurate estimation of sediment distribution.

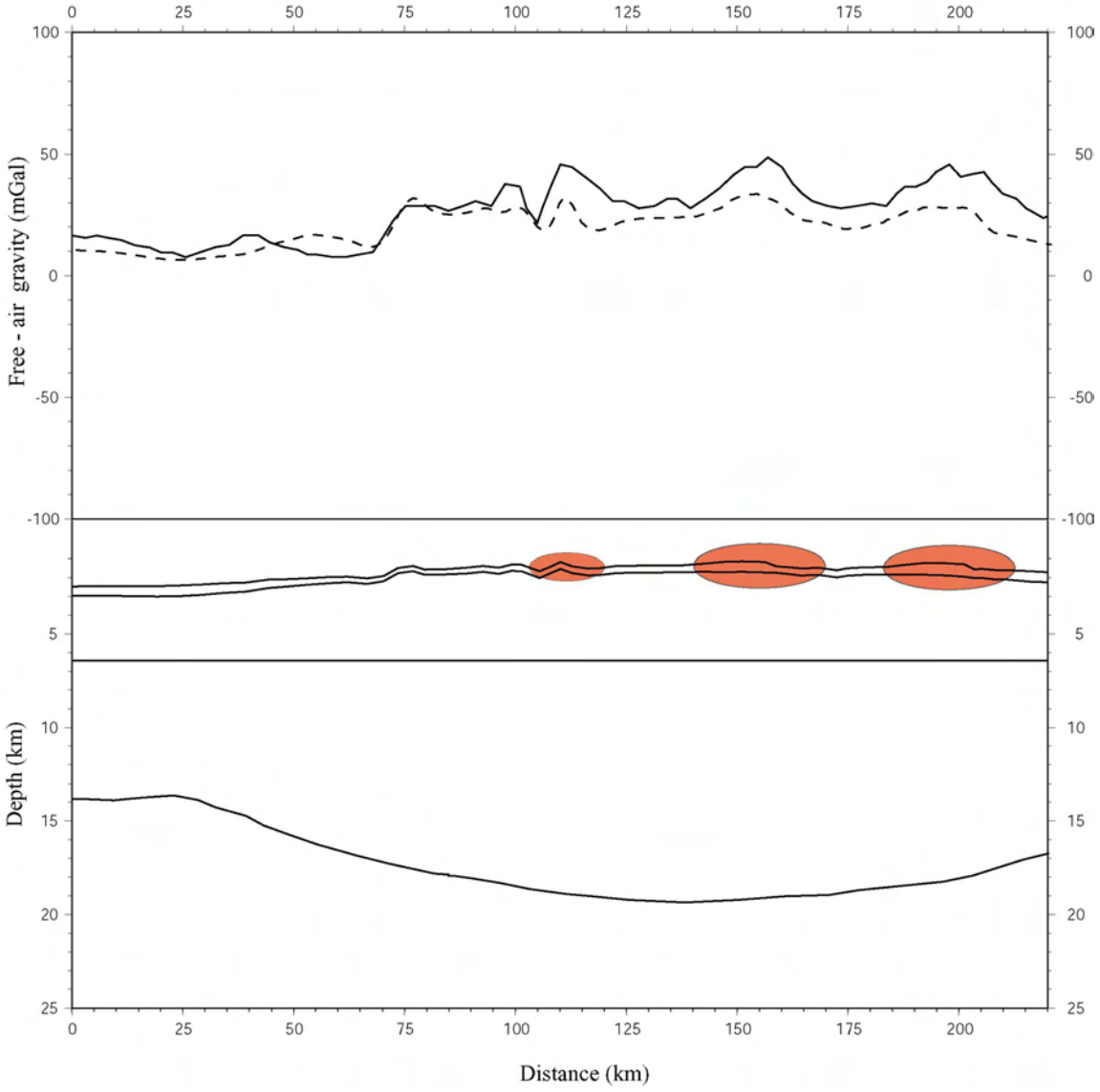

Figure 25. Gravity modeling solution along transect D-D'. The red ellipsoids in the crustal model (bottom panel) enclose possible basement highs whose real geometry is thought to has been underestimated as result of the inaccurate estimation of sediment distribution.

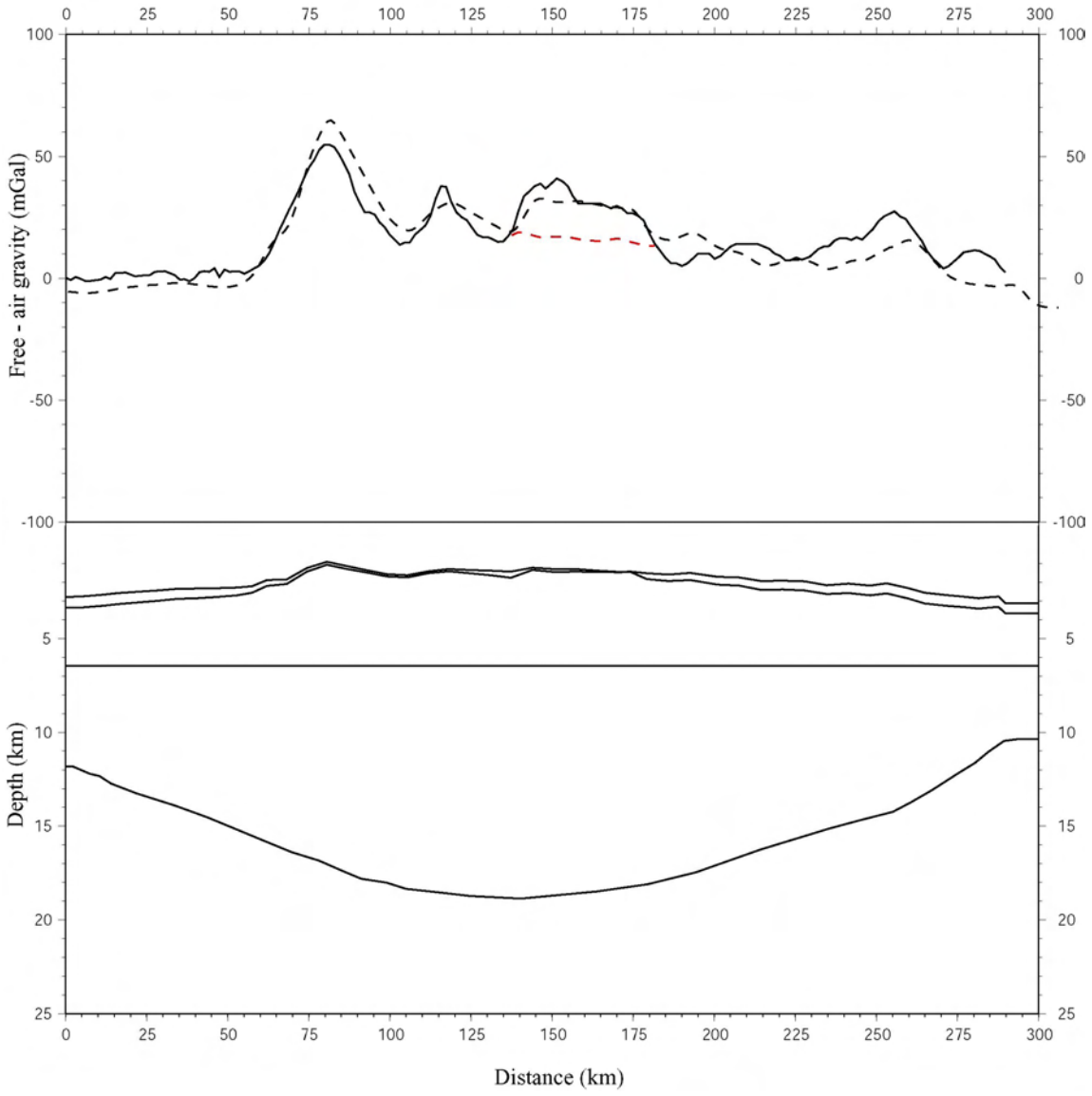

Figure 26. Gravity modeling solution along transect C-C' (corrected bedrock relief). The solid black line represents the observed gravity anomaly field, whereas the dashed black line corresponds to the calculated gravity anomaly field. The dashed red line corresponds to the gravity anomaly field originally calculated by employing an estimated bedrock relief in my model structure (Figure 24). In the new crustal model (bottom panel) the upper crustal geometry was modified by correcting the sediment cover over a short wavelength bathymetric high shown in Figure 24 (area enclosed by the red ellipsoid).

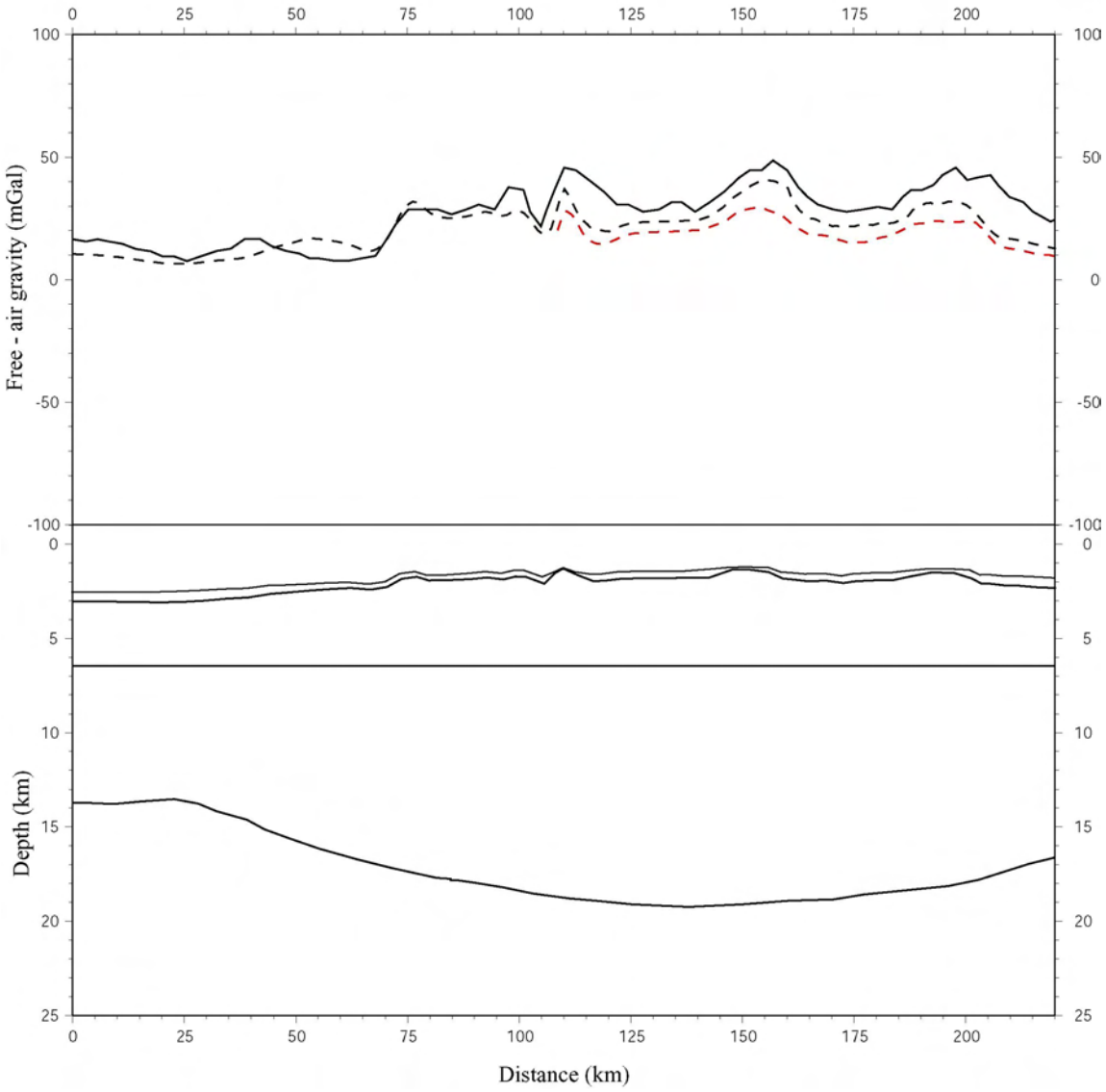

Figure 27. Gravity modeling solution along transect D-D' (corrected bedrock relief). The solid black line represents the observed gravity anomaly field, whereas the dashed black line corresponds to the calculated gravity anomaly field. The dashed red line corresponds to the gravity anomaly field originally calculated by employing an estimated bedrock relief in my model structure (Figure 25). In the new crustal model (bottom panel) the upper crustal geometry was modified by correcting the sediment cover over a seamount-like structure and a local short wavelength bathymetric highs shown in Figure 25 (areas enclosed by the red ellipsoids).

Along transect 2 (Figure 28), the fit between calculated and observed gravity anomaly data is good on the northern flank of this transect (mean misfit of < ~5 mGal.), whereas large differences (up to ~40 mGal) are observed at the crest of the ridge, between ~50 km and ~100 km, and along its southern flank.

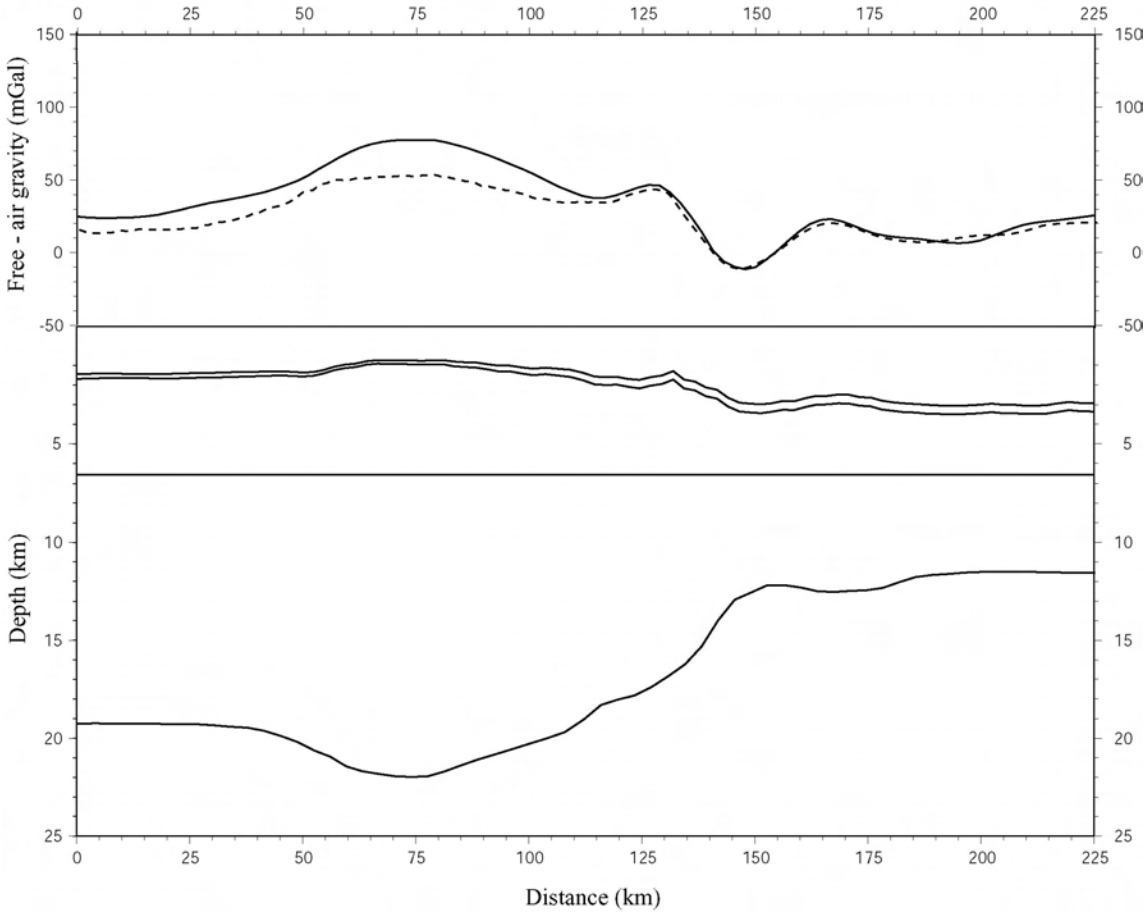

Figure 28. Gravity modeling solution along reference transect 2. The solid line represents the observed gravity anomaly field, whereas the dashed line corresponds to the calculated gravity anomaly field. The crustal model is shown in the bottom panel.

Because of its high amplitude and long-wavelength, I consider that the observed misfit could not be simply explained by the inaccurate definition of bedrock relief in my crustal model. In order to evaluate this assertion I initially determined the extent to which a poorly defined upper crustal geometry on this region could affect the calculated gravity anomaly field. This objective was accomplished by first examining available seismic reflection profiles across the crest of the ridge [*Lonsdale*, 1978] with the purpose of determining the major differences between the basement geometry defined in my crustal model and that resolved from seismic data. In contrast to a sediment-free volcanic edifice resolved from seismic data, the estimated bedrock relief shows the presence of a sedimentary layer with a mean thickness of ~300 m. Based on this observation, I then proceeded to modify my crustal model by eliminating sediment cover at the crest of the ridge. As expected, this correction made little improvement of the fit between calculated and observed gravity anomaly data (between ~5 mGal and 10 mGal) (Figure 29).

An alternative explanation for the large residual misfit at the crest of the ridge (~30 mGal) is errors in the crustal root geometry defined in my crustal model, particularly overestimated Moho depth variations associated with the prominent bathymetric edifice that characterizes this region. *Lonsdale* [1978] suggested that the origin of this bathymetric edifice is related to the formation of an outer rise resulting from the collision of Carnegie Ridge with the Ecuador Trench and the subsequent flexural bending of the oceanic lithosphere. Though difficult to distinguish from volcanic relief,

an outer rise 300 m to 400 m high has been resolved from seismic data at a distance of ~100 km from the trench axis [*Lonsdale*, 1978].

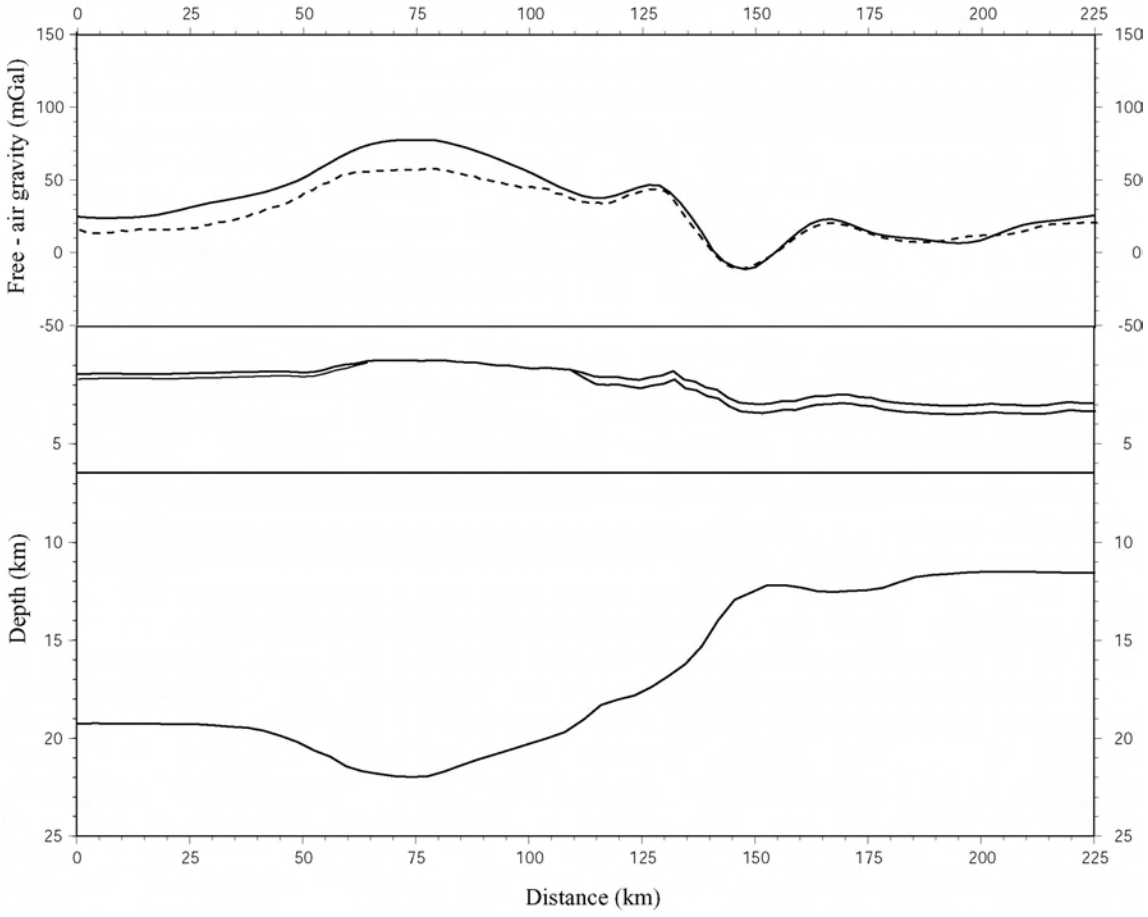

Figure 29. Gravity modeling solution along reference transect 2 (corrected bedrock relief). The solid line represents the observed gravity anomaly field, whereas the dashed line corresponds to the calculated gravity anomaly field. In the crustal model (bottom panel), sediment thickness was eliminated at the crest of the ridge while retaining the isostatically estimated crustal root geometry.

Because of the recent origin and tectonic nature of this dynamic uplift, I consider that a significant portion of the observed bathymetric edifice is not compensated as a product of variation in crustal root thickness as assumed in my crustal model. The last will result, in turn, in a crustal root beneath the crest of the ridge not only shallower than originally estimated from bathymetry data, but also with a different geometry. Since the southern part of transect 2 crosses the expected location of this rise, I consider that the misfit observed in this region could also be related to overestimated Moho depth variations along with an inaccurate geometry of the compensating crustal root.

Based on these considerations, my crustal model was modified by adjusting the depth of the estimated crustal root below the crest of the ridge and along its southern flank until a good fit between calculated and observed gravity anomaly data was achieved (overall mean misfit of ~10 mGal) (Figure 30) .

3.1.2. Other Sources of Error

An alternative explanation for the observed misfit along the different transects examined is variation of the linear layer 2/layer 3 interface, assumed horizontal in my crustal models. In order to evaluate this alternative source of error, I first modified the model structures already corrected along reference transects 1 (corrected bedrock relief) (Figure 18) and 2 (corrected bedrock relief and Moho depth) (Figure 30) by replacing the flat boundary between layer 2 and layer 3 with the interface resolved from seismic data (i.e., 6.5 km/s isovelocity contour in their velocity models). The gravity anomaly over the new model structures was then calculated in order to determine the extent to which the irregular geometry of the seismically determined layer 2/layer 3 interface

affects the calculated gravity anomaly field, and subsequently the fit with respect to the observed gravity anomaly data.

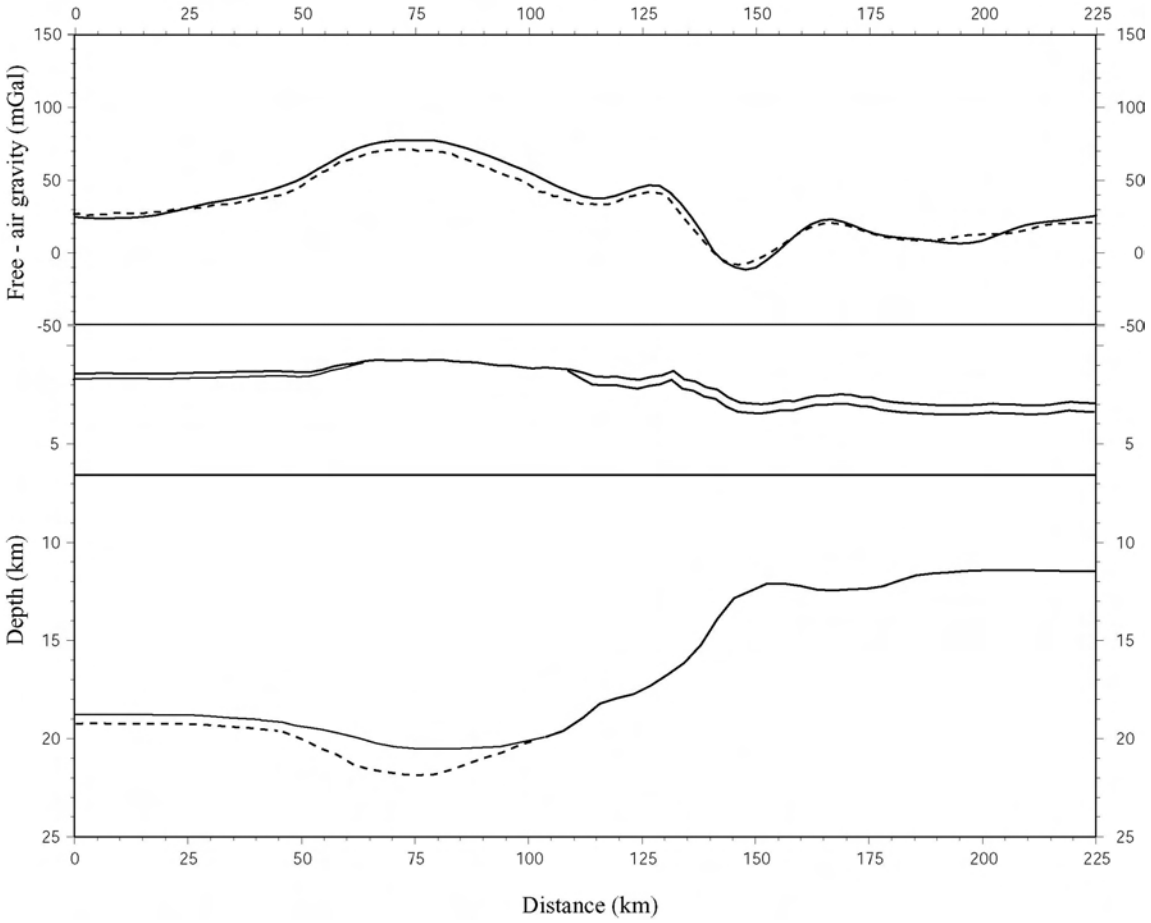

Figure 30. Gravity modeling solution along reference transect 2 (corrected Moho geometry). The solid line represents the observed gravity anomaly field, whereas the dashed line corresponds to the calculated gravity anomaly field. The dashed line in the crustal model (bottom panel) shows the extent to which the crustal root beneath the crest of the ridge was modified.

Along reference transect 1 (Figure 31), the gravity anomaly calculated over the model structure with the seismically determined layer 2/layer 3 interface reproduced adequately the wavelength and amplitude as well as the magnitude of the observed gravity anomaly field on the central and northern parts of this transect (between ~175 km and 350 km). On the southern part of this transects (between 0 km and ~175 km), the calculated gravity anomaly accounted adequately for the wavelength and amplitude of the observed gravity anomaly field but failed in reproducing its magnitude. Compared with the fit between calculated and observed gravity anomaly data obtained by employing a flat layer 2/ layer 3 interface (Figure 18), the use of the seismic boundary improved this fit in some areas by ~10 mGal (i.e., central and southern part of reference transect 1) while retaining and even increasing the error by a similar amount in others (i.e., southern part of reference transect 1).

Along reference transect 2 (Figure 32), the calculated gravity anomaly reproduced adequately the wavelength and amplitude as well as the magnitude of the observed gravity anomaly filed along this transect. Similar to the case of reference transect 1, the use of the seismically determined layer 2/layer 3 interface in the model structure improved the fit between calculated and observed gravity anomaly data by ~10 mGal relative to that previously obtained by employing a model structure with a flat interface (Figure 30).

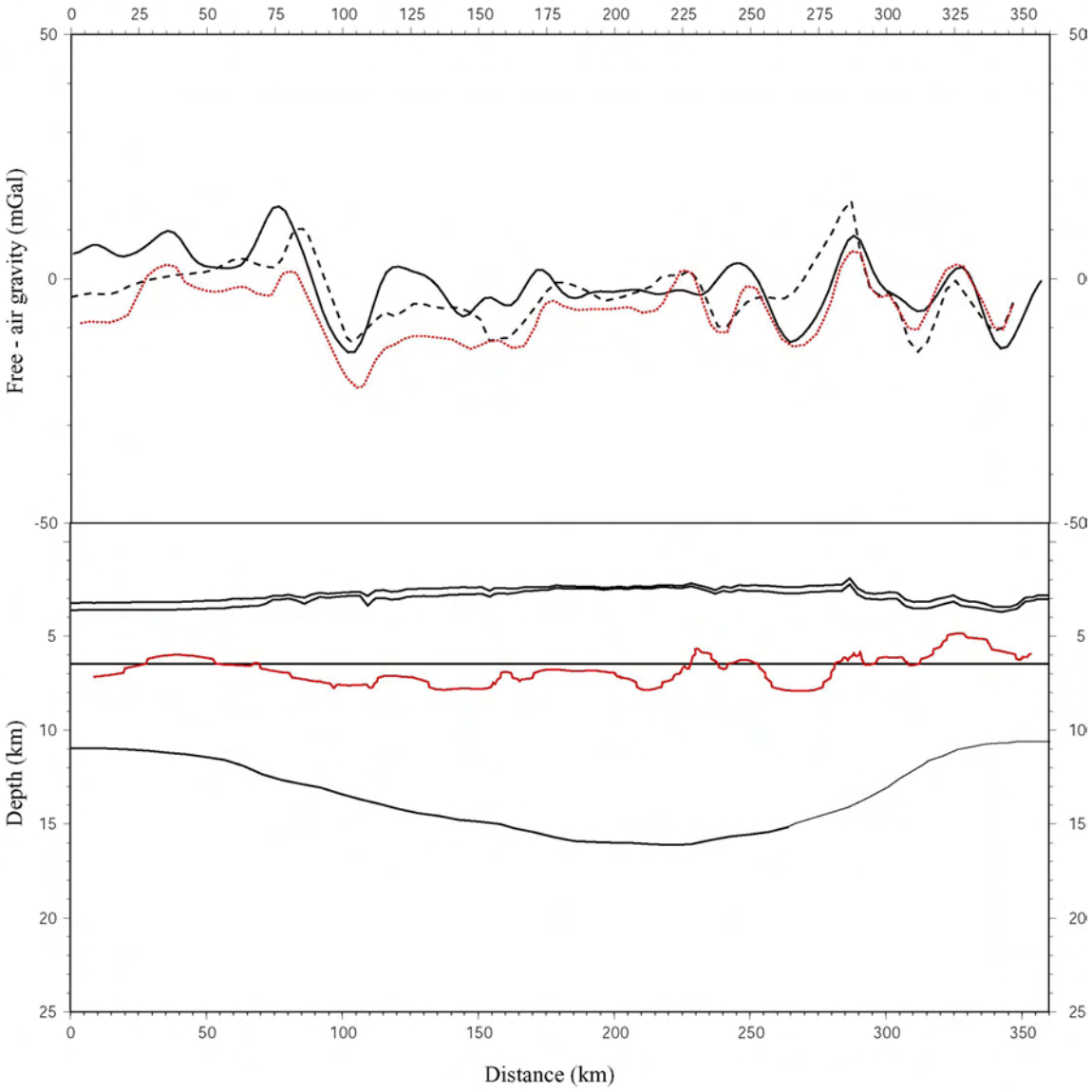

Figure 31. Gravity modeling solution along reference transect 1 employing the seismically determined layer 2/layer 3 interface. The solid black line corresponds to the observed gravity anomaly field along this transect. The dotted red line represents the gravity anomaly calculated over the model structure with a layer 2/layer 3 interface determined from seismic data (solid red line in the model structure). The dashed black line represents the gravity anomaly calculated over the model structure with a flat layer2/layer3 interface. The solid red line in the model structure (bottom panel) correspond to the layer 2/layer 3 interface determined from seismic data.

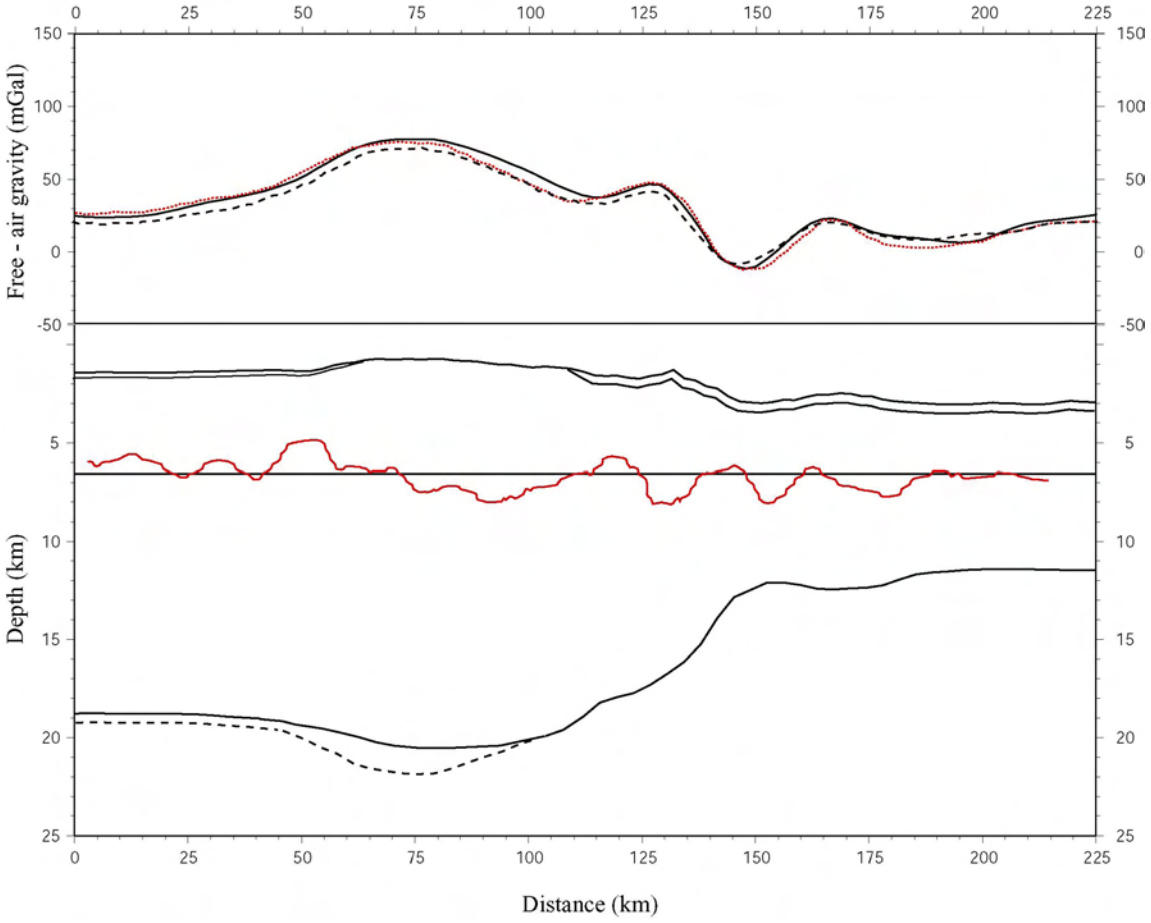

Figure 32. Gravity modeling solution along reference transect 2 employing the seismically determined layer 2/layer 3 interface. The solid black line corresponds to the observed gravity anomaly field along this transect. The dotted red line represents the gravity anomaly calculated over the model structure with a layer 2/layer 3 interface determined from seismic data (solid red line in the model structure). The dashed black line represents the gravity anomaly calculated over the model structure with a flat layer 2/layer 3 interface. The solid red line in the model structure (bottom panel) correspond to the layer 2/layer 3 interface determined from seismic data.

3.2. Predicted Crustal Structure

Based on the analysis of the potential sources of error for the different transects examined in this study, I consider that the approach described in section 2.2.2. can be applied in order to adequately define the long-wavelength model structures along any ridge transect of Carnegie Ridge. As shown before, except for regions near the Ecuador Trench (i.e., reference transect 2) the overall misfit between calculated and observed gravity anomaly data is small (between ~10 mGal and ~15 mGal) and can be corrected by minor changes on shallow crustal structures (i.e., bedrock relief and layer 2/layer 3 interface)**.** Based on this premise, the results of this study were generalized by defining an isostatic Moho depth grid for Carnegie Ridge (Figure 33) based on the assumption that its long-wavelength crustal structure is mainly defined by the estimated isostatic crustal root geometry. This grid was defined according to the procedure described in section 2.3.1. The isostatic Moho depth grid was in turn employed to define an isostatic crustal thickness grid (Figure 34) and an excess crustal thickness grid (the thickness of normal oceanic crust excluded, i.e., 7 km) (Figure 35) for the study area, following to the procedure described in section 2.3.1.

3.3. Crustal Volume Flux

The crustal volume flux through time at the Galápagos Archipelago and Carnegie Ridge, and at Cocos Ridge, along with the total crustal volume flux through time were calculated according to the procedure described in section 2.3.2. (Figure 36).

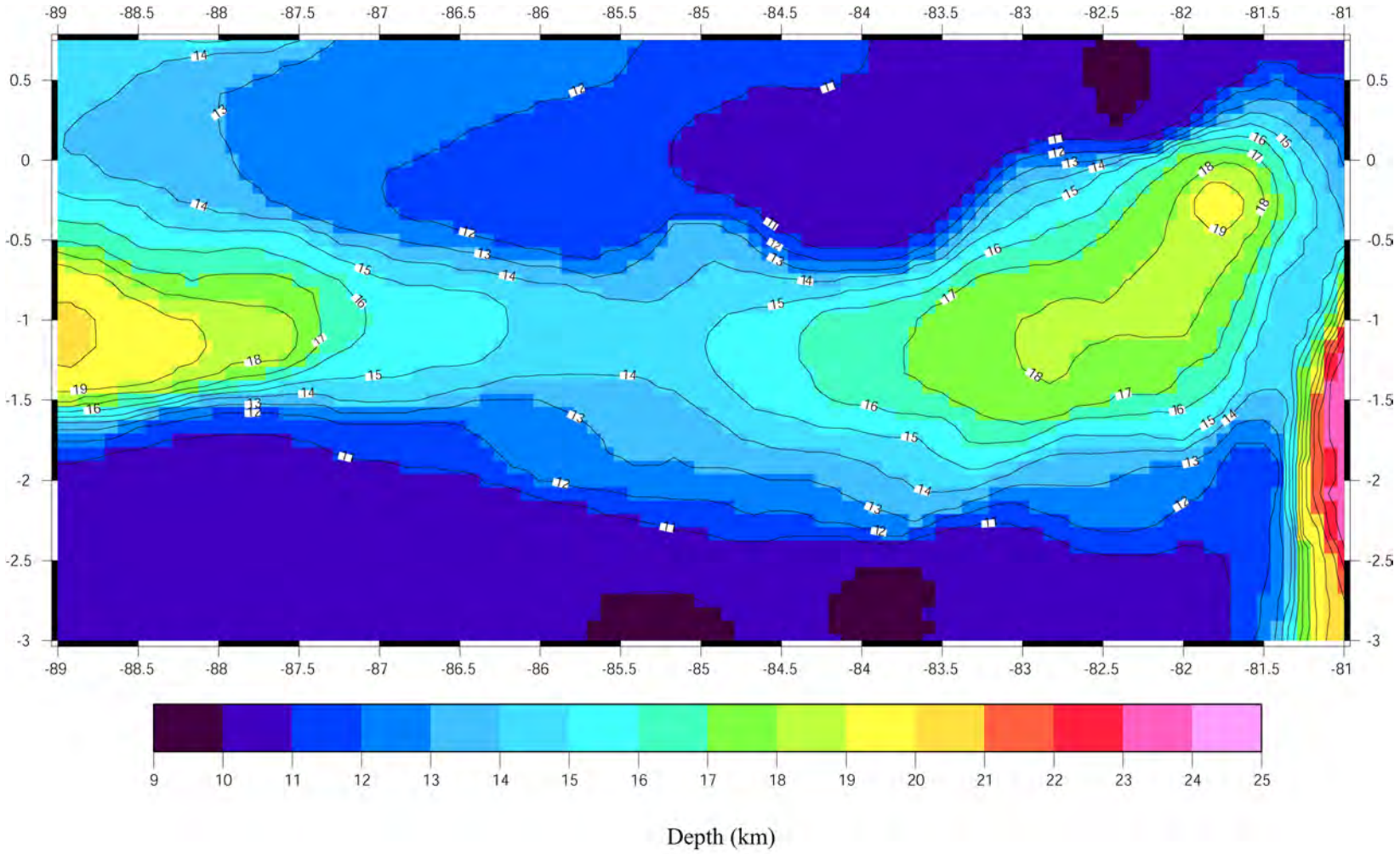

Figure 33. Estimated isostatic Moho depth on Carnegie Ridge.

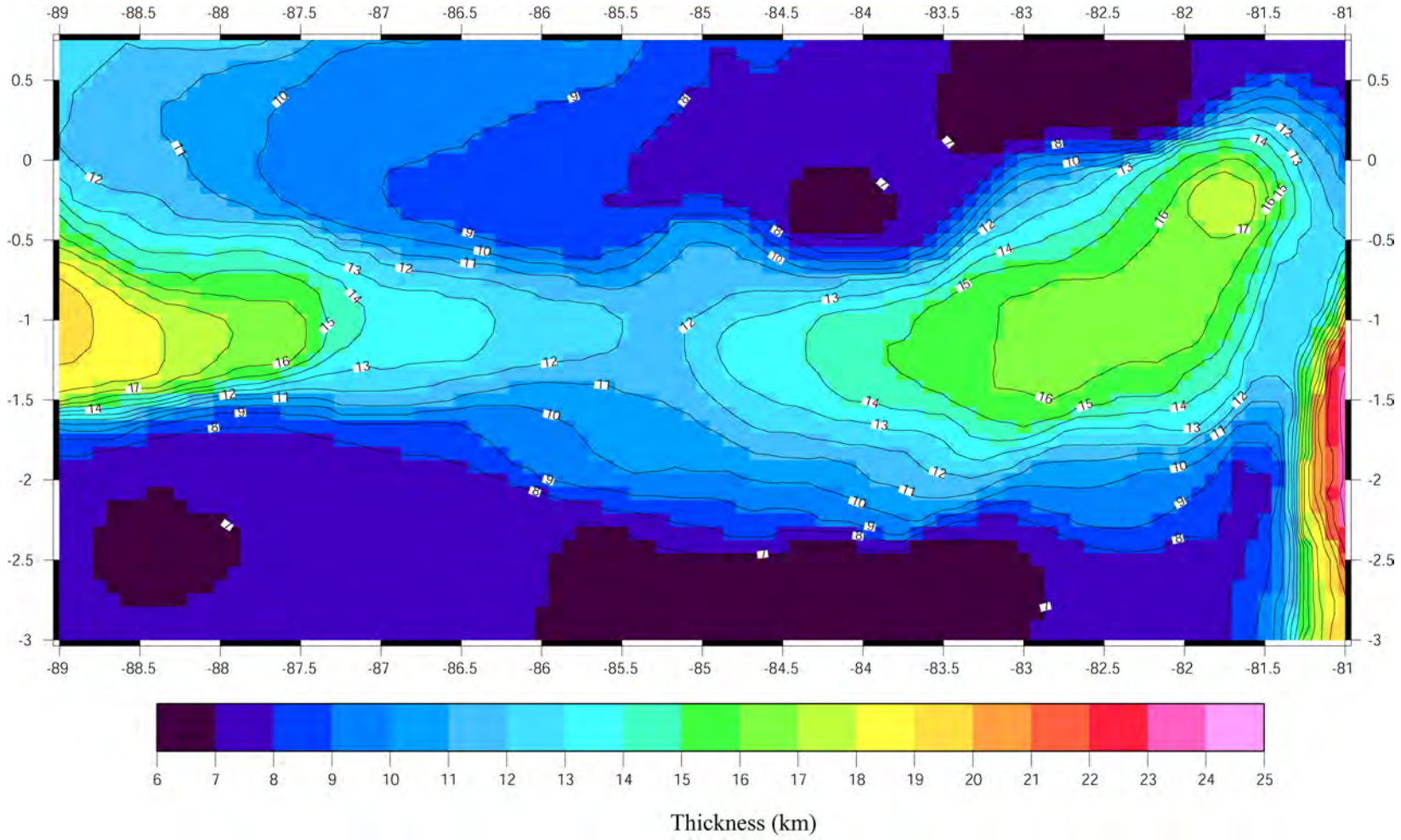

Figure 34. Estimated isostatic crustal thickness on Carnegie Ridge.

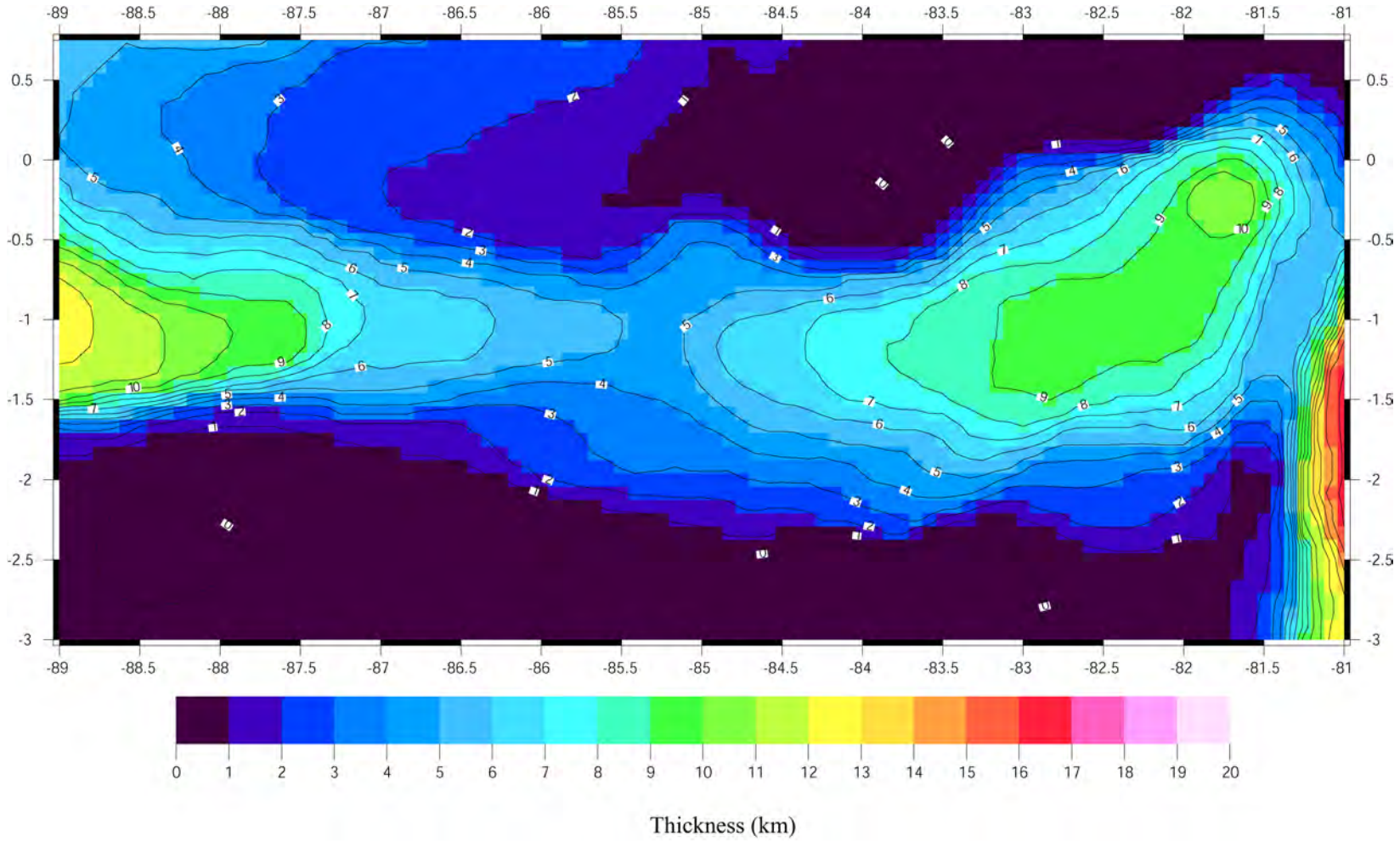

Figure 35. Estimated excess crustal thickness on Carnegie Ridge.

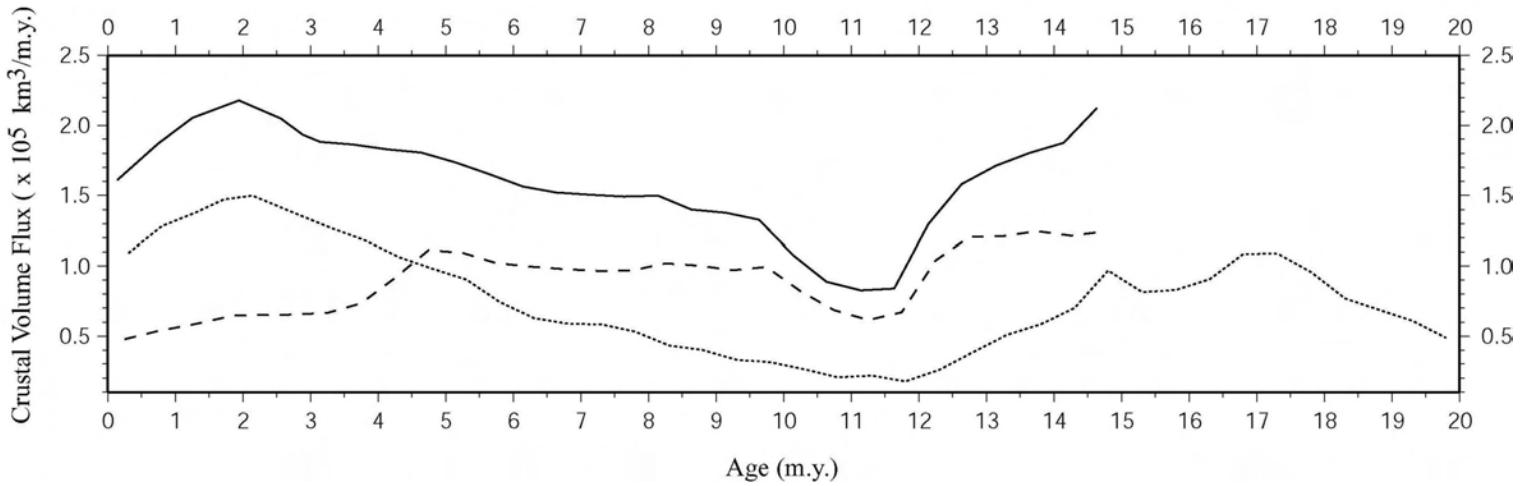

Figure 36. Calculated crustal volume flux through time. The dotted line represents the values calculated for the Galápagos Archipelago and Carnegie Ridge. The dashed line corresponds to the values calculated for Cocos Ridge. The solid line represents the total crustal volume flux through time during the last 15 m.y.

The values calculated at the Galápagos Archipelago and Carnegie Ridge show an increase from ~0.49 x 10^5 km^3/m.y at ~20 Ma to ~1.09 x 10^5 km^3/m.y at ~17.5 Ma, followed by a decrease to ~0.18 x 10^5 km^3/m.y at ~15.5 Ma. The decrease in crustal volume flux at ridge segments older than ~17.5 m.y (i.e., between ~20 Ma and ~17.5 Ma) is not consider to be real but probably the result of volcanic material missing due to the subduction of Carnegie Ridge during the last 2 m.y [e.g., Gutscher et al., 1999]. Between ~15.5 Ma and 14.5 Ma the calculated crustal volume flux values increase to ~1.10 x 10^5 km^3/m.y The observed peak at this time step is thought to be produced by the irregular spacing between the predicted 14 m.y and the 15 m.y isochrons (i.e., relative to the spacing of the other isochrons) (Figure12), which increased the amount of volcanic material employed for the crustal volume flux calculation. Since ~14.5 Ma, the calculated crustal volume flux curve shows a decrease to values of ~0.18 x 10^5 km^3/m.y at ~11.5 Ma. Since then, values increase again to ~1.54 x 10^5 km^3/m.y at ~2.5 Ma followed by a decrease to ~1.09 x 10^5 km^3/m.y at the present time.

At Cocos Ridge, the calculated crustal volume flux curve is characterized by nearly uniform values of ~1.23 x 10^5 km^3/m.y between ~15 Ma and ~12.5 Ma, followed by a decrease to a minimum value of ~0.61 x 10^5 km^3/m.y at ~11.5 Ma. From this time, crustal volume flux values increase to ~1.0 x 10^5 km^3/m.y at ~9.5 Ma, remaining approximately constant from then until ~5 Ma, when values increase to ~1.25 x 10^5 km^3/m.y Between ~5 Ma and the present time, the crustal volume flux curve shows a decrease to values of ~69 x 10^5 km^3/m.y at the present time.

The total crustal volume flux curve shows a decrease from values of ~2.34 x 10^5 km^3/m.y at ~15 Ma to ~0.83 x 10^5 km^3/m.y at ~11.5 Ma. Between this time and ~2 Ma values increase to ~2.37 x 10^5 km^3/m.y, with a prominent peak of ~2.12 x 10^5 km^3/m.y at ~5 Ma. Since then, the total crustal volume flux curve shows a decrease to values of ~1.62 x 10^5 km^3/m.y at the present time.

CHAPTER IV

DISCUSSION

In this study, I estimated the long-wavelength crustal structure of Carnegie Ridge. This objective was accomplished by initially defining in a systematic way 2-D crustal models based on the assumption that the ridge is isostatically compensated according to the Airy model. The consistency of the estimated model structures with observed gravity was then evaluated by employing 2-D forward gravity modeling. Perhaps the most significant implication of this analysis is that simple 2-D crustal models built by assuming Airy isostasy satisfactorily accounts for the observed gravity anomaly field over the ridge and subsequently for its long-wavelength crustal structure. Except for regions near the Ecuador Trench (i.e., along reference transect 2), the overall misfit of the gravity modeling solutions along the different transects examined in this study is small and can be corrected by minor changes on shallow crustal structures (i.e., bedrock relief and the geometry of the layer 2/layer 3 interface). Reference transect 2 and its southwestward prolongation (nearly parallel to the Ecuador Trench) crosses the expected location of an outer rise formed at a distance of ~100 km from the Ecuador Trench axis [*Lonsdale*, 1978]. As shown before, the dynamic uplift associated to the presence of this rise resulted in overestimated Moho depth variations. The presence of this dynamic uplift is a notorious characteristic of volcanic islands emplaced on oceanic crust that is approaching a deep-sea trench [*Dubois et al*., 1975; *Woodroffe*, 1988; *Woodrofe et al*., 1990]. *Watts and Talwani* [1974] pointed out that in regions where an outer rise occurs,

gravity modeling solutions show a poor correlation relative to the observed gravity anomaly field if the oceanic crust beneath the rise thickens as predicted by the Airy compensation model. Instead, they demonstrated that a good fit between calculated and the observed gravity anomaly data can be achieved by warping upward the oceanic crust beneath the rise. Under such conditions, the crust-mantle boundary will have a shallower depth and slightly different geometry than predicted by the Airy model. If a Moho geometry with characteristics similar to those proposed by *Watts and Talwani* [1974] occurs on eastern Carnegie Ridge, it would be observed on seismic structure models crossing the axis of the outer rise (i.e., perpendicular to the Ecuador Trench and to reference transect 2). Although a recent seismic refraction experiment determined the crustal structure along a ridge transect crossing the Ecuadorian margin (transect 3 in Figure 4) [*Graindorge et al*., 2004], it did not reach the expected location of the outer rise an subsequently did not resolve the crustal structure beneath it.

The presence of an Airy type compensation on Carnegie Ridge is considered to be consistent with its formation near the CNSC. Under such conditions, volcanic material forming ridges is emplaced on young and thin oceanic lithosphere with low elastic plate thickness [e.g., *Watts*, 1978; *Watts and Zhong*, 2000] and little or no long-term elastic bending strength [e.g., *Detrick and Watts*, 1979]. *Detrick and Watts* [1979] pointed out that since weak lithosphere is unable to distribute loading stress laterally by bending, isostatic adjustment might occur as a result of vertical movements of large fault-bounded crustal blocks. These authors further suggested that this mechanism of isostatic adjustment could explain the presence of large scarps and the fault morphology that

characterizes many aseismic ridge formed near a spreading center (e.g., Eastern Walvis Ridge and Ninetyeast Ridge). Because of the presence of a comparable morphology on Carnegie Ridge [e.g., *van Andel et al*, 1971], I consider that isostatic adjustment on the ridge might have been achieved through a similar mechanism.

4.1. Major Features of the Estimated Crustal Structure

The estimated long-wavelength crustal structure on Carnegie Ridge is characterized by crustal thickening being accommodated in oceanic layer 3, in agreement with observations in most overthickened oceanic crustal sections [e.g., *Mutter and Mutter*, 1993]. This feature is in turn consistent with the results of wide-angle refraction seismic studies [*Sallarés et al*., submitted, 2004] which show a crustal structure characterized by a constant thickness oceanic layer 2 beneath the ridge regardless of total crustal thickness variations (i.e., crustal thickness is accommodated in layer 3). Seismic structures with similar characteristics have been determined on Cocos [*Sallarés et al*., 2003; *Walther*, 2002, 2003] and Malpelo ridges [*Sallarés et al*., 2003], which suggests that emplacement of crustal overthickening in oceanic layer 3 is a common feature of the volcanic ridges of the GVP.

The estimated isostatic Moho geometry is asymmetric, showing a steeper transition from beneath the bulge of the ridge to the nearby oceanic basin on the ridge flank closest to the CNSC. A similar asymmetry is observed on the Moho geometry determined from seismic refraction data along reference transects 1 and 2 [*Sallarés et al*, submitted, 2004] and their conjugate ridge segments on southern Cocos and Malpelo ridges, respectively

[*Sallarés and Charvis*, 2003]. This observation seems to confirm that the asymmetry of the estimated crustal root geometry is not an artifact of the method used in this study to define Moho depth variations, but a regional feature of the aseismic ridges of the GVP.

Because of the occurrence of a steeper crustal root geometry transition on the ridge flank closest to the spreading center, I consider that this asymmetry might me explained by a ridge-related rifting. A plausible tectonic scenario would be the following. As the GHS and the CNSC started to interact at ~20 Ma [e.g., *Hey*, 1977; *Meschede and Barckhausen*, 2001; *Sallarés and Charvis*, 2003], the hotspot enhanced mantle melting beneath the spreading center giving rise to the formation of Carnegie and Malpelo ridges on the Nazca and Cocos plates, respectively [e.g., *Hey*, 1977; *Sallarés and Charvis*, 2003] (Figure 37). These two ridges were subsequently split apart by seafloor spreading along the CNSC. The presence of synchronous magnetic anomalies on both sides of the extinct Malpelo Rift shows evidence of the separation of the easternmost part of Carnegie Ridge and Malpelo Ridge since ~18 Ma [*Lonsdale*, 1978]. As rifting continued, the thermal expansion of mantle material related to the presence of the GHS beneath the CNSC was followed by contraction as seafloor spreading carried Carnegie Ridge laterally away from the hotspot. This thermal contraction resulted in the subsequent cooling and thickening of the lithosphere beneath the ridge as well as beneath its adjacent oceanic basins given that the lithosphere-asthenosphere interface is a rheological boundary dependent on temperature. The thickness of the oceanic lithosphere on the basin side closest to the spreading center (i.e., northern flank of Carnegie Ridge) must have remained thinner relative to that on the opposite flank of the

ridge (i.e., southern flank of Carnegie Ridge) because of the presence of the GHS near the CNSC and its subsequent thermal influence (Figure 37). This mechanism could explain the steeper crustal root geometry transition from the beneath bulge of the ridge to the nearby oceanic basin on the northern flank of eastern Carnegie Ridge relative to that on its southern flank. During the formation and tectonic evolution of this ridge segment (between ~20 Ma and ~15 Ma), the GHS remained nearly ridge centered in the vicinity of the GHS with the latter being located beneath the Nazca Plate [*Sallarés and Charvis*, 2003].

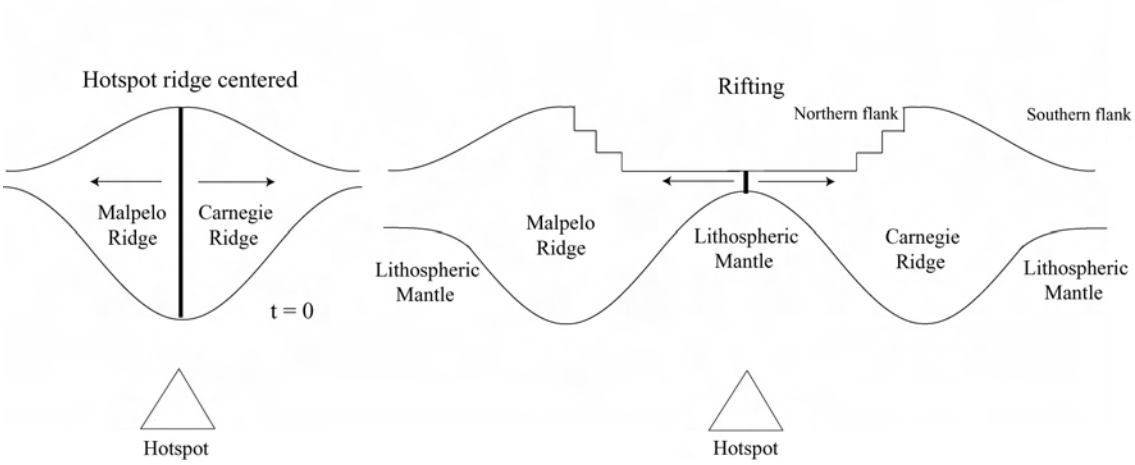

Figure 37. Cartoon showing the probable explanation for the asymmetry of the crustal root geometry on eastern Carnegie Ridge.

In a similar way, the differential contraction of the lithosphere beneath the ridge relative to that beneath its adjacent oceanic basins during cooling, along with the isostatic adjustment of the volcanic load [e.g., *Detrick and Watts*, 1979] might explain

the faulted morphology of eastern Carnegie Ridge [e.g., *van Andel et al.*, 1971]. The effects of this differential contraction are expected to be higher on the basin side of the ridge where the lithosphere is hotter and subsequently thinner, which might in turn explain the presence of a pronounced scarp on the northern flank of eastern Carnegie Ridge.

On the other hand, the asymmetry of the estimated crustal root geometry on Western Carnegie Ridge (between ~87.5° W and 89° W in Figure 33) shows an opposite behavior, with an steeper transition from beneath the bulge of the ridge to the nearby oceanic basin on the southern flank of the ridge than on its northern flank. In contrast to the asymmetry on eastern Carnegie Ridge, which could probably be explained by a ridge-related rifting, the origin and nature of the asymmetry on Western Carnegie Ridge is uncertain. The lack of seismic refraction data on this region restricts any possibility to evaluate whether the asymmetry of the estimated crustal root geometry is real or it is just an artifact related to the presence of a prominent bathymetric scarp on the southern flank of the ridge.

4.2 Crustal Volume Flux Variations

In general, the calculated crustal volume flux curves for the Galápagos Archipelago and Carnegie Ridge, and for Cocos Ridge (Figure 36) indicate that a higher amount of volcanic material was emplaced on the Cocos Plate than on the Nazca Plate between at least ~15 Ma and ~5 Ma. Since then, the amount emplaced on the Nazca Plate has been higher than that emplaced on the Cocos Plate. The upper limit of the period in which a

higher amount of volcanic material was emplaced on the Cocos Plate (i.e., 15 Ma) is uncertain given that crustal volume flux was not calculated for ages older than 15 m.y. It is evident, however, that since at least ~15 Ma this amount was higher on the Cocos Plate than on the Nazca Plate.

If we assume that differences in the amount of volcanic material emplaced on each plate occur as a result of variations in the relative location of the GHS with respect to the CNSC (i.e., beneath the Nazca or the Cocos plates) [e.g., *Hey*, 1977; *Meschede and Barckhausen*, 2001; *Barckhausen et al*, 2001; *Sallarés and Charvis*, 2003], my results indicate that the GHS was placed beneath the Cocos Plate between at least ~15 Ma and ~5 Ma and since then it has been placed beneath the Nazca Plate (Figure 38). This observation is in agreement with the results obtained by *Hey* [1977] from the analysis and interpretation of bathymetric and magnetic data. Although recent studies agree with the fact that the GHS was located north of the CNSC (i.e., beneath the Cocos Plate) at ~15 Ma [e.g., *Barckhausen et al*., 2001], there are different interpretations (compared to my results) regarding the time that the hot spot remained beneath the Cocos Plate. *Sallarés and Charvis* [2003] suggested that the CNSC shifted to the north of the GHS placing it beneath the Nazca Plate at ~7.5 Ma, which is in agreement with the 7-9 m.y estimated by *Wilson and Hey* [1995]. If these results are correct, it would imply that a higher amount of volcanic material was emplaced on the Nazca Plate than on the Cocos Plate between ~7-9 Ma. My results disagree with this hypothesis showing that during this time the calculated crustal volume flux on the Nazca Plate is ~2.5 times lower than that on the Cocos Plate (Figure 36).

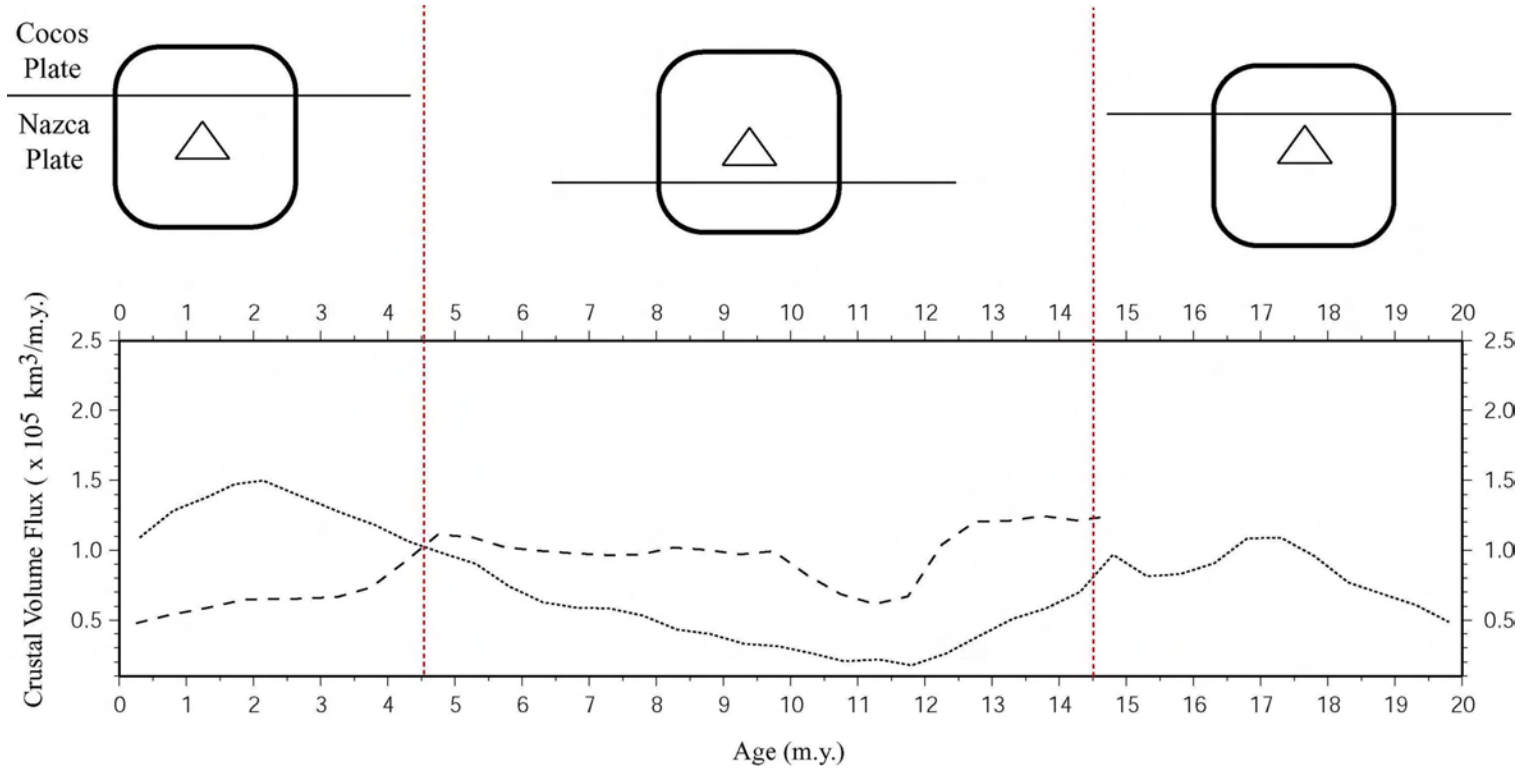

Figure 38. Differences in the amount of volcanic material emplaced on the Cocos and Nazca plates. The solid black line in the upper panel represents the relative location of the CNSC with respect to the GHS (triangle). The rounded square represents the amount of hotspot volcanic products emplaced on the Cocos and Nazca plates. In the lower panel, the dashed back line represents the crustal volume flux at Cocos Ridge whereas the dotted black line represents the crustal volume flux at Carnegie Ridge and the Galápagos Archipelago.

Regardless of the uncertainty and errors that the method used to estimate these values could have, a simple inspection of a bathymetric map of the GVP (Figure 12) shows that between ~7 and ~9 Ma Cocos Ridge is wider than its coeval ridge segment on Carnegie Ridge (relative to the 2400 isobath). This observation seems to contradict the presence of the GHS beneath the Nazca Plate during this time, if the width of each ridge at this time is taken as a relative measure of the amount of hot spot products deposited on each side of the CNSC [e.g., *Meschede and Barckhausen*, 2001].

In addition to relative differences in the amount of hotspot products deposited on the Nazca or Cocos plate sides of the CNSC, the calculated crustal volume curves show variations in the amount of volcanic material emplaced on each plate. Since my crustal volume flux calculations were determined from estimated excess crustal thickness values (i.e., the thickness of normal oceanic crust excluded), their variations represent as well changes in the crustal thickness of the hotspot traces emplaced on the Nazca and Cocos plates.

By assuming a constant intensity and fixed location of the GHS, variations in the amount of volcanic material emplaced on the Nazca and Cocos plates have been interpreted to be the result of changes in the relative distance between the CNSC and the GHS [e.g., *Hey*, 1977; *Meschede and Barckhausen*, 2001; *Barckhausen et al*, 2001; *Sallarés and Charvis*, 2003]. These changes are consider to be related to the northward migration of the CNSC along with prominent southward ridge jumps and temporal variations in the spreading rate [e.g., *Hey*, 1977; *Wilson and Hey*, 1995; *Barckhausen et al*., 2001]. Although the details of the relative spreading center – hotspot motion cannot

be determined from the calculated crustal volume flux values, these data can be employed to evaluate whether their variations are exclusively related to changes in the relative distance between the CNSC and the GHS.

According to my results, the nearly uniform crustal volume flux at Cocos Ridge between ~15 Ma and ~12.5 Ma and the observed decrease at Carnegie Ridge during this time implies a decline in the total volume output of the GHS. If the intensity of the GHS had remained constant, the observed decline in the amount of volcanic material emplaced on the Nazca Plate between ~15 Ma and ~13 Ma would have resulted in a reciprocal increase on the Cocos Plate [e.g., *Hey*, 1977; *Meschede and Barckhausen*, 2001] (Figure 39). This expectation disagrees with my results which show a nearly uniform crustal volume flux at Cocos Ridge during this time. Since my results do not provide information regarding the relative spreading center–hotspot motion (e.g., relative distance between the CNSC and the GHS through time), it would be highly speculative to explain how the calculated decline in the intensity of the GHS resulted in the crustal volume fluxes calculated at Cocos Ridge and Carnegie Ridge. My results seem to indicate, however, that a constant total volume output of the GHS would not explain the calculated crustal volume fluxes at these ridges between ~15 Ma and ~12.5 Ma.

Between 12.5 Ma and ~10.5 Ma, my results indicate that the calculated crustal volume flux decreased both at the Cocos and Carnegie ridges as result of a decline in the intensity of the GHS.

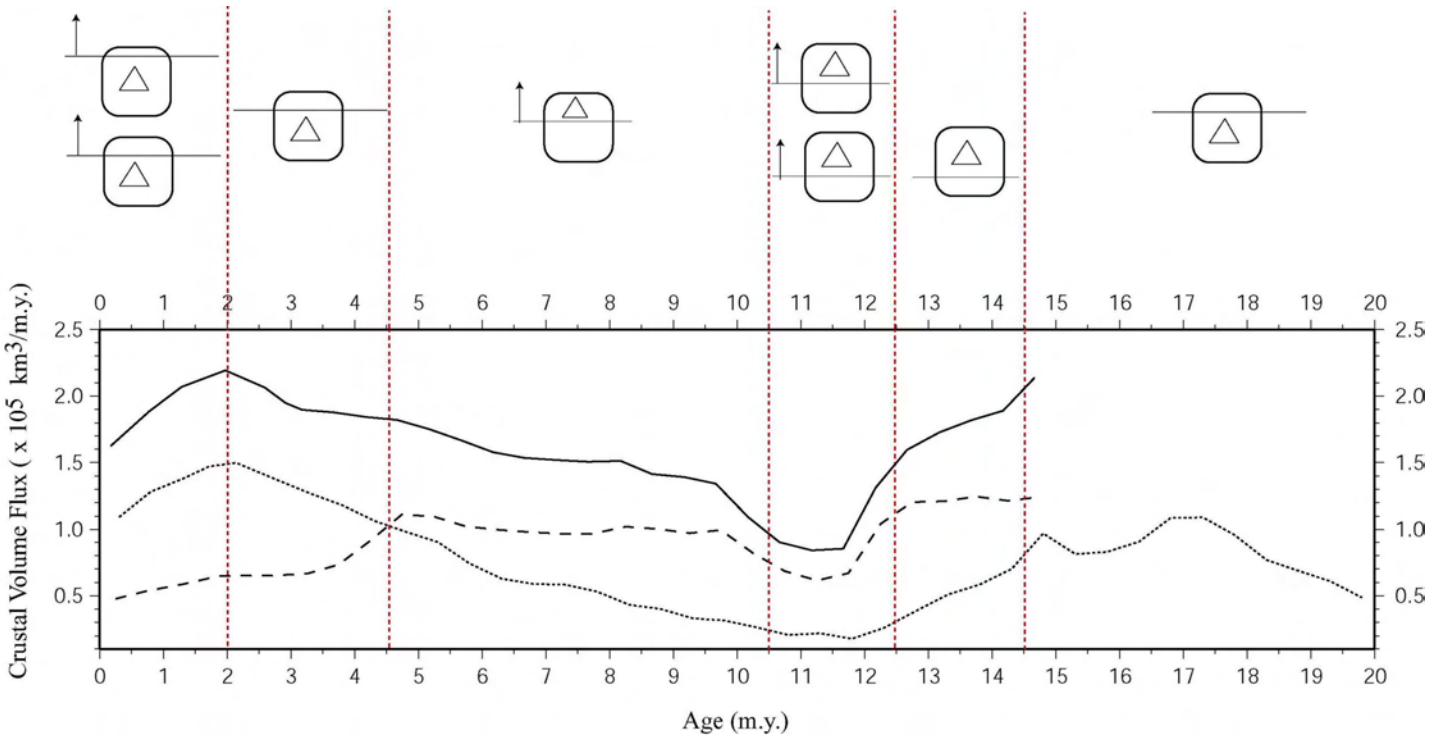

Figure 39. Variations in the calculated crustal volume flux at Carnegie Ridge and the Galápagos Archipelago, and at Cocos Ridge. The solid black line in the upper panel represents the relative location of the CNSC with respect to the GHS (triangle). The rounded square represents the amount of hotspot volcanic products emplaced on the Cocos and Nazca plates. In the lower panel, the dashed back line represents the crustal volume flux at Cocos Ridge whereas the dotted black line represents the crustal volume flux at Carnegie Ridge and the Galápagos Archipelago.

If during this time the intensity of the GHS remained constant and the CNSC kept migrating northward toward the hotspot, the decline in the amount of volcanic material emplaced on the Cocos Plate would have resulted in a reciprocal increase on the Nazca Plate (Figure 39). This expectation does not fit my results but also cannot explain the simultaneous formation of bathymetric saddles at both sides of the spreading center (Figure 12). Alternatively, my results suggest that the presence of synchronous bathymetric saddles on Cocos and Carnegie ridges represent a reduction in the amount of volcanic material emplaced on the Cocos and Nazca plates between ~12.5 Ma and ~10.5 Ma as a result of a decline in the intensity of the GHS.

Between ~10 Ma and ~5 Ma, my results indicate that as result of an increase in the intensity of the GHS, the calculated crustal volume flux at Cocos Ridge remained nearly constant whereas that at Carnegie Ridge increased ~4 times. A constant volume output of the hotspot along with the northward migration of the spreading center could explain the increase in crustal volume flux at Carnegie Ridge as the CNSC approached the GHS (Figure 39). However this increase would have required a reciprocal decrease at Cocos Ridge. Alternatively, my results indicate that as the CNSC approached the GHS and the amount of hotspot products being transferred to the Nazca Plate subsequently increased, the relative reduction in the amount of volcanic material emplaced on the Cocos Plate was compensated by an increase in the intensity of the GHS. The latter, in turn, might have kept the crustal volume flux at Cocos Ridge during this time nearly constant.

Since ~5 Ma, my results indicate that the crustal volume flux at the Galápagos Archipelago and Cocos Ridge is related to an increase in the intensity of the GHS

between ~5 Ma and ~2 Ma, followed by a decrease that has continued until the present time. Although the presence of a widespread volcanism on the Galápagos Platform since at least ~5 Ma [*Sinton et al*., 1996] could probably be explained by an increase in hotspot intensity, there is not evidence that this pattern had changed during the last 2 m.y when the calculated total volume output decreased. On the other hand, the occurrence of an increasing total volume output between ~5 Ma and ~2 Ma seems to explain the nearly uniform amount of volcanic material emplaced on the Cocos Plate during this time, despite the northward migration of the CNSC and its subsequent increase in distance relative to the GHS. The decline of the total volume output of the GHS during the last 2 m.y would in turn explain the reduction in the hotspot products deposited on the Cocos Plate since then until the present time.

A major problem with the crustal volume flux calculated at the Galápagos Archipelago is related with the assumption of an Airy-type compensation in this region despite the proximity of the GHS. It has been proposed [*Ribe and Christensen*, 1999; *Sleep*, 1990] that in the presence of a hotspot (e.g., Hawaii), the surrounding seafloor is uplifted (i.e., hotspot swell) by the dynamic pressure of plume material flowing in the asthenosphere away from the plume center. Accordingly, plume material in motion is thought to dynamically support the hotspot swell (e.g., Hawaii) as this material hits the lithosphere and is dragged off generally in the direction of plate motion [Li et al., 2004]. Despite of the presence of a bathymetric uplift of ~500 m in the central and western platforms of the Galápagos Archipelago (between ~89° W and 91.66° W) (Figure 40), and their probable dynamic compensation, I have assumed that these regions are

isostatically compensated as a result of variations in crustal root thickness. The latter would imply errors in the estimated isostatic crustal thickness and excess crustal thickness, and subsequently in the calculated crustal volume flux at the central and western Galápagos platforms. These regions correspond to hotspot traces emplaced on the Nazca Plate during the last ~4 m.y.

A recent seismic refraction experiment across the Galápagos platform [*Toomey et al.*, 2001] has resolved a maximum crustal thickness of ~15 km beneath its western segment, which is approximately 5 km lower than the estimated isostatic value. By assuming a similar differences in crustal thickness beneath the central platform where seismic refraction data is not available, the crustal volume flux values calculated at the western and central platforms of the Galápagos Archipelago are ~25 % lower than those previously determined in these regions.

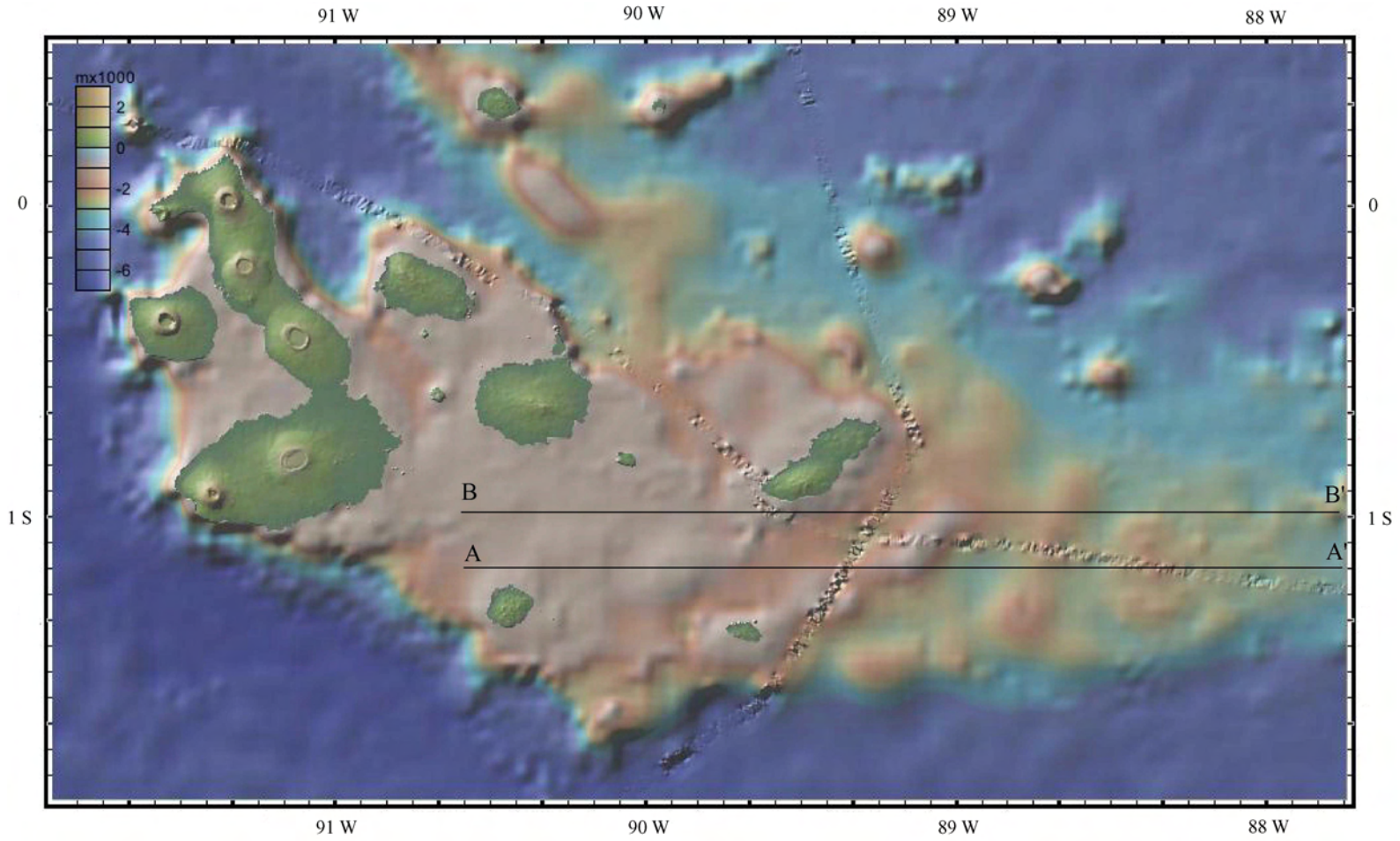

Figure 40. Bathymetric map of the Galápagos Archipelago. Notice the prominent bathymetric changes between the western and central platforms, and the eastern platform (western Carnegie Ridge), along transects A-A' and B-B'.

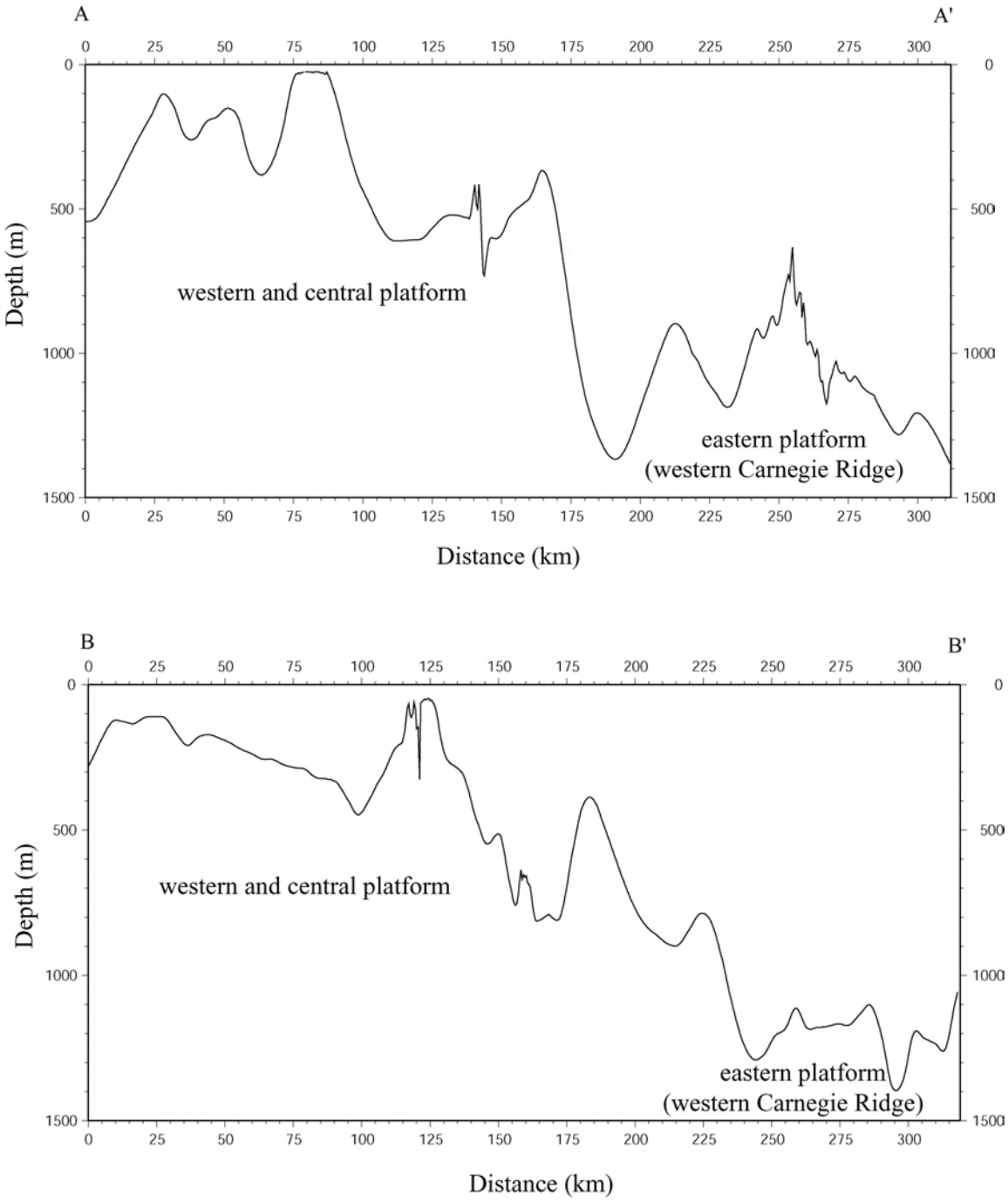

Figure 40. Continued

CHAPTER V

CONCLUSIONS

In this study, I estimated the long-wavelength crustal structure of Carnegie Ridge by employing 2-D forward gravity modeling as the primary analytical technique. The gravity modeling solution along the different transects examined in this study demonstrated that except for regions near the Ecuador Trench, simple 2-D crustal models built by assuming Airy isostasy accounts adequately for the observed gravity anomaly field.

The estimated long-wavelength crustal structure is characterized by crustal thickening mainly accommodated in oceanic layer 3 and the asymmetry of the crustal root geometry. On eastern Carnegie Ridge, this asymmetry is thought to be related to a ridge-related rifting whereas the origin and nature of that determined on western Carnegie Ridge remain uncertain. Variations in the estimated along-axis crustal thickness were found to be related not only to changes in the relative spreading center – hotspot distance but also to variations in the total volume output of the GHS. According to my results, soon after the CNSC shifted to the south of the GHS (i.e., ~15 Ma), the hotspot intensity started to decline. This decay continued for ~4.5 m.y, giving rise to a reduction in the amount of volcanic material emplaced on the Nazca Plate, and subsequently to the westward decrease of the along-axis crustal thickness of eastern Carnegie Ridge. The most obvious evidence of a decline in the intensity of the GHS is the simultaneous formation of bathymetric saddles both on Carnegie and Cocos Ridges

between ~12.5 Ma and ~10 Ma. Since ~10 Ma the volume output of the GHS started to increase again, giving rise to the formation of western Carnegie Ridge and the Galápagos Archipelago. This increase continued until ~2 Ma, when the hotspot intensity started a new decrease that continues until the present time.

REFERENCES

Barckhausen, U., C. R. Ranero, R. von Huene, S. C. Cande, and H. A. Roeser (2001), Revised tectonic boundaries in the Cocos Plate off Costa Rica: Implications for the segmentation of the convergent margin and for plate tectonic models, *J. Geophys. Res., 106*(B9*)*, 19,207–19,220.

Calmant, S. (1987), The elastic thickness of the lithosphere in the Pacific Ocean, *Earth Planet. Sci. Lett., 85*, 277–288.

Canales, J. P., J. J. Dañobeitia, R. S. Detrick, E. E. E. Hooft, R. Bartolomé, and D. F. Naar (1997), Variations in axial morphology along the Galápagos spreading center and the influence of the Galápagos hotspot, *J. Geophys. Res., 102*(B12), 27,341–27,354.

Canales, J. P., G. Ito, R. S. Detrick, and J. Sinton (2002), Crustal thickness along the western Galápagos spreading center and the compensation of the Galápagos hotspot swell, *Earth Planet. Sci. Lett., 203*, 311–327.

Carlson, R. L. and C. N. Herrick (1990), Densities and porosities in the oceanic crust and their variations with depth and age, *J. Geophys. Res., 95*(B6*)*, 9153–9170.

Detrick, R. S. and A. B. Watts (1979), An analysis of isostasy in the world's oceans, 3. Aseismic ridges, *J. Geophys. Res., 84*(B7), 3637–3653.

Detrick, R. S., J. M. Sinton, G. Ito, J. P. Canales, M. Behn, T. Blacic, B. Cushman, J. E. Dixon, D. W. Graham, and J. J. Mahoney (2002), Correlated geophysical, geochemical, and volcanological manifestations of plume-ridge interaction along the Galápagos spreading center, *Geochem. Geophys. Geosyst. 3*(10), 8501, doi:10.1029/2002GC000350.

Divins, D. (2001), Total sediment thickness of the world's oceans & marginal seas, http:/www.ngdc.gov/mgg/sedthick.html, Mar. Geol. and Geophys. World Data Cent., Boulder, CO.

Dubois., J., J. Launay, and J. Recy (1975), Some new evidence on lithospheric bulges close to island arcs, *Tectonophysics, 26*, 189–196.

Feighner, M. A. and M. A. Richards (1994), Lithospheric structure and compensation mechanisms of the Galápagos Archipelago, *J. Geophys. Res., 99*(B4), 6711–6729.

Graindorge, D., A. Calahorrano, P. Charvis, J.-Y. Collot, and N. Bethoux (2004), Deep structures of the Ecuador convergent margin and the Carnegie Ridge, possible

consequence on great earthquakes recurrence interval, *Geophys. Res. Lett., 31*, L04603, doi:10.1029/2003GL018803.

Gutscher, M.-A., J. Malavieille, S. Lallemand, and J.-Y. Collot (1999), Tectonic segmentation of the North Andean margin: Impact of the Carnegie Ridge collision, *Earth Planet. Sci. Lett., 168*, 255–270.

Hamilton, E. L. (1978), Sound velocity-density relations in sea-floor sediments and rocks, *J. Acoust. Soc. Am., 63*(2), 366–377.

Heath, G. R. and T. H. van Andel (1973), Tectonics and sedimentation in the Panama Basin: Geologic results of Leg 16, Deep Sea Drilling Project, in *Initial Reports of the Deep Sea Drilling Project*, vol. 16, T. H. van Andel, G. R. Heath, et al., pp. 899–913, U. S. Government Printing Office, Washington, D.C.

Hey, R. (1977), Tectonic evolution of the Cocos-Nazca spreading center, *Geol. Soc. Am. Bull., 88*, 1404–1420.

Hey, R., G. L. Johnson, and A. Lowrie (1977), Recent plate motions in the Galápagos area, *Geol. Soc. Am. Bull., 88*, 1385–1403.

Ito, G. T. and J. Lin (1995), Mantle temperature anomalies along the past and paleoaxes of the Galápagos spreading center as inferred from gravity analyses, *J. Geophys. Res., 100*(B3), 3733–3745.

Korenaga, J., P. B. Kelemen, and W. S. Holbrook (2002), Methods for resolving the origin of large igneous provinces from crustal seismology, *J. Geophys. Res., 107*(B9), 2178, doi:10.1029/2001JB001030.

Li, X., R. Kind, X. Yuan, I. Wölbern, and W. Hanka (2004), Rejuvenation of the lithosphere by the Hawaiian plume, *Nature*, *427*, 827–829.

Lonsdale, P. (1978), Ecuadorian subduction system, *Am. Assoc. Petrol. Geol. Bull., 62*, 2454–2477.

Lonsdale, P. and K. D. Klitgord (1978), Structure and tectonic history of the eastern Panama Basin, *Geol. Soc. Am. Bull., 89*, 981–999.

Meschede, M. and U. Barckhausen (2001), The relationship of the Cocos and Carnegie ridges: Age constraints from paleogeographic reconstructions, *Int. J. Earth Sci., 90*, 386–392.

Morgan, W. J. (1978), Rodriguez, Darwin, Amsterdam, …, A second type of hotspot island, *J. Geophys. Res., 83*(B11), 5355–5360.

Mutter, C. Z. and J. C. Mutter (1993), Variations in thickness of layer 3 dominate oceanic crustal structure, *Earth Planet. Sci. Lett., 117*, 295–317.

Nafe, J. E. and C. L. Drake (1957), Variations with depth in shallow and deep water marine sediments of porosity, density and the velocities of compressional and shear waves, *Geophysics*, *22*, 523-552.

Ribe, N. M. and U. R. Christensen (1999), The dynamical origin of Hawaiian volcanism, *Earth Planet. Sci. Lett., 171*, 517–531.

Sallarès, V. and P. Charvis (2003), Crustal thickness constraints on the geodynamic evolution of the Galápagos Volcanic Province, *Earth Planet. Sci. Lett., 214*, 545–559.

Sallarès, V., P. Charvis, E. R. Flueh, and J. Bialas (2003), Seismic structure of Cocos and Malpelo volcanic ridges and implications for hot spot-ridge interaction, *J. Geophys. Res., 108*(B12), 2564, doi:10.1029/2003JB002431.

Sallarès, V., P. Charvis, E. R. Flueh, J. Bialas, and the SALIERI Scientific Party (2004), Seismic structure of the Carnegie Ridge and the nature of the Galápagos melt anomaly, submitted to *Geophys. J. Int.*

Sandwell, D. T. and W. H. F. Smith (1997), Marine gravity anomaly from Geosat and ERS-1 satellite altimetry, *J. Geophys. Res., 102*(B5), 10,039–10,054.

Schilling, J.-G., R. H. Kingsley, and J. D. Devine (1982), Galápagos hot spot-spreading center system, 1. Spatial petrological and geochemical variations (83°W–101°W), *J. Geophys. Res., 87*(B7), 5593-5610.

Schilling, J.-G. (1991), Fluxes and excess temperatures of mantle plumes inferred from their interaction with migrating mid-ocean ridges, *Nature*, *352*, 397–403.

Shipboard Scientific Party (2003), Leg 202 summary, *Proc. Ocean Drill. Program Initial Rep.*, 202, 1-145.

Sinton, C. W., D. M. Christie, and R. A. Duncan (1996), Geochronology of Galápagos seamounts, *J. Geophys. Res., 101*(B6), 13,689-13,700.

Sleep, N. H. (1990), Hotspots and mantle plumes: Some phenomenology, *J. Geophys. Res., 95*, 6715-6736.

Talwani, M., J. L. Worzel, and M. Landisman (1959), Rapid gravity computations for two-dimensional bodies with application to the Mendocino submarine fracture zone, *J. Geophys. Res., 64*(1), 49-59.

Toomey, D. R., E. E. E. Hooft Toomey, and R. S. Detrick (2001), Crustal thickness variations and internal structure of the Galápagos Archipelago, *Eos Trans. AGU*, *82*(47), Fall Meet. Suppl., Abstract T42B-0939.

van Andel, T., G. R. Heath, B. T. Malfait, D. F. Heinrichs, and J. I. Ewing (1971), Tectonics of the Panama Basin, eastern equatorial Pacific, *Geol. Soc. Am. Bull., 82*, 1489–1508.

Walther, C. H. E. (2002), Crustal structure of the Cocos Ridge northeast of Cocos Island, Panamá Basin, *Geophys. Res. Lett., 29*(20), 1986, doi:10.1029/2001GL014267.

Walther, C. H. E. (2003), The crustal structure of the Cocos Ridge off Costa Rica, *J. Geophys. Res., 108*(B3), 2136, doi:10.1029/2001JB00888.

Watts, A. B. and M. Talwani (1974), Gravity anomalies seaward of deep-sea trenches and their tectonic implications, *Geophys. J. R. Astr. Soc., 36*, 57–90.

Watts, A. B. (1978), An analysis of isostasy in the world's oceans, 1. Hawaiian–Emperor Seamount Chain, *J. Geophys. Res., 83*(B12), 5989–6004.

Watts, A. B. and S. Zhong (2000), Observations of flexure and the rheology of oceanic lithosphere, *Geophys. J. Int., 142*, 855–875.

Wilson, D. S. and R. N. Hey (1995), History of rift propagation and magnetization intensity for the Cocos-Nazca spreading center, *J. Geophys. Res., 100*(B7), 10,041–10,056.

Woodroffe, C. D. (1988), Vertical movement of isolated oceanic islands at plate margins: Evidence from emergent reefs in Tonga (Pacific Ocean), Cayman Islands (Caribbean Sea) and Christmas Island (Indian Ocean), *Z. Geomorph. Suppl.-Bd., 69*, 17–37.

Woodroffe, C., R. McLean, H. Polach, and E. Wallensky (1990), Sea level and coral atolls: Late Holocene emergence in the Indian Ocean, *Geology, 18*, 62–66.

Wortel, R. and S. Cloetingh (1981), On the origin of the Cocos-Nazca spreading center, *Geology, 9*, 425-430.

VITA

Giorgio De La Torre

Personal Information

Address: Instituto Oceanográfico de la Armada, Base Naval Sur, Guayaquil-Ecuador

Phone: 593-42481300

e-mail: gdelatorre13@hotmail.com

Education

- B.S. with Honors, Marine Sciences, December, 1997, Escuela Superior Naval "Cmdte. Rafael Morán Valverde", Salinas-Ecuador.
- M.S. May, 2005, Oceanography, Texas A&M University, College Station, TX